DEVELOPMENT OF COATINGS ON Ti6Al4V ALLOY FOR NEW GENERATION BONE IMPLANTS WITH IMPROVED OSSEOINTEGRATION

Nataša Drnovšek

Doctoral Dissertation
Jožef Stefan International Postgraduate School
Ljubljana, Slovenia, November 2012

Evaluation Board:

Prof. Dr. Miran Čeh, Jožef Stefan Institute, Jamova cesta 39, 1000 Ljubljana, Slovenia

Prof. Dr. Miran Gaberšček, National Institute of Chemistry, Hajdrihova 19, 1000 Ljubljana, Slovenia

Prof. Dr. Jef Vleugels, KU Leuven, Kasteelpark Arenberg 44, B-3001 Heverlee Leuven, Belgium

MEDNARODNA PODIPLOMSKA ŠOLA JOŽEFA STEFANA
JOŽEF STEFAN INTERNATIONAL POSTGRADUATE SCHOOL

Nataša Drnovšek

DEVELOPMENT OF COATINGS ON Ti6Al4V ALLOY FOR NEW GENERATION IPLANTS BONE WITH IMPROVED OSSEOINTEGRATION

Doctoral Dissertation

RAZVOJ PREVLEK NA ZLITINI Ti6Al4V ZA NOVO GENERACIJO KOSTNIH VSADKOV Z IZBOLJŠANO OSTEOINTEGRACIJO

Doktorska disertacija

Supervisor: Asst. Prof. Saša Novak Krmpotič

Ljubljana, Slovenia, November 2012

Index

Abstract

The aging of bone tissue, bone defects that form during the removal of cysts, tumours, genetic defects and other bone-tissue-related diseases, together with demands for a better quality of life, mean a requirement for materials, artificial or autogenous, that will have a long functionality and survivability under the body's environmental conditions.

For hard-tissue replacement, the most widely used materials are titanium alloys. They are commonly used for bone substitutes, joints and dental implants, with the aim of permanently supporting or replacing injured or disease-damaged bone. Titanium itself is considered to be a biocompatible material that satisfies the need for mechanical support relatively well due to its high flexural strength and tolerable elastic modulus. However, when an implant is in direct contact with bone tissue in a complex dynamic system, it is typically not only exposed to mechanical loads, but it is also affected by extracellular liquid and proteins. This exposure results in a slow, but continuous, release of ions; for example, in the case of the Ti6Al4V alloy, titanium is released, as well as harmful alloying elements like aluminium and vanadium that are important constituents of the alloy.

Titanium, although it is biocompatible, is also bioinert, and as such it cannot form strong, interfacial, chemical bonding with bone, and in comparison with bioactive materials, its osseointegration rate is slow. Therefore, to avoid the dissolution of the alloying elements and their diffusion into the body, it is necessary to improve the quality of the native oxide layer and to increase its thickness. Furthermore, a surface modification is necessary to improve the osseointegration.

In this study, a naturally formed, amorphous TiO_2 layer was transformed into a crystalline one by a hydrothermal treatment in the presence of titanium ions. Morphology advantageous for bioactivity was achieved by using the appropriate dopants and surface-active agents during the processing. Different morphologies, sizes of crystals and thicknesses of the coatings were achieved by changing the hydrothermal conditions, such as temperature, time, pH and additives. Firmly attached anatase coatings were prepared. These coatings were tested both *in vitro* and *in vivo*, whereas the cell adhesion and proliferation tests revealed that the morphology of anatase crystals is important for cell attachment and growth. Similarly, the formation of hydroxyapatite when soaked in simulated body-fluid solution was influenced by the different anatase planes.

This investigation showed titania to be bioactive, but the rate of hydroxyapatite formation is still slow compared to other bioactive materials such as hydroxyapatite or other calcium phosphate ceramics and bioactive glasses. Bioactive glass is a bioresorbable material with an excellent bioactivity that is osteoconductive and osteoproductive and can form a strong bond with soft and hard tissues. However, due to its poor mechanical properties, bioactive glass is not suitable for use in load-bearing applications and its use is therefore mainly limited to coatings.

It was proposed that a combination of a porous titanium surface layer coated with BAG would significantly improve the osseointegration. However, to prepare BAG coating within the porous titanium structure, fine bioactive glass particles are needed. As melt-derived BAG does not meet the requirements, a particulate sol-gel method was developed in this study to prepare nanosized spherical particles that were then applied to the alloy substrate from the suspension by vacuum infiltration. Different bioactive glass compositions were prepared and characterized in terms of sintering, crystallization, antibacterial properties, and bioactivity, as well as *in vivo* tests on the BAG coatings.

Both coatings combined were applied and examined. Titania and bioactive glass were applied on the Ti-alloy to achieve good bioactivity provided by bioactive glass and to assure protection from the metal ions released by the titania coating even long after the bioactive glass is resorbed.

Povzetek

Zaradi staranja kostnega tkiva, kostnih defektov, ki nastanejo pri odstranitvi cist, tumorjev, genetskih defektov in ostalih kostnih bolezni, skupaj z vse večjo željo po boljši kvaliteti življenja, narašča tudi potreba po materialih, umetnih ali avtogenih, ki bi jih telo dobro sprejelo, ki bi imeli dolgo življenjsko dobo in ki bi dobro prenesli pogoje v človeškem telesu.

Med najbolj pogoste materiale za zamenjavo kostnega tkiva spadajo titanove zlitine. Te se uporabljajo za dentalne vsadke, kostne vijake, ploščice in za zamenjavo celotnih sklepov z namenom zamenjati oboleli oziroma poškodovani del kosti. Titan je namreč biokompatibilen material, ki ima relativno zadovoljive mehanske lastnosti. Vendar pa vsadek pri direktnem stiku s kostjo v kompleksnem dinamičnem sistemu telesa ni izpostavljen samo mehanskim obremenitvam, ampak je tudi pod velikim vplivom ekstracelularnih tekočin in proteinov. To pa privede do počasnega, vendar kontinuirnega sproščanja škodljivih kovinskih ionov. V primeru Ti6Al4V zlitine se sproščajo Ti in tudi toksična Al in V. Po letih sproščanja takšnih ionov lahko pride do negativnega odziva organizma. Druga slaba stran titanovih zlitin je njihova bioinertnost. Čeprav so titanove zlitine biokompatibilne, kar pomeni, da jih okoliško tkivo lahko sprejme, ne morejo tvoriti kemijske vezi s kostjo. V primerjavi z bioaktivnimi materiali je njihova hitrost osteointegracije počasna.

Da bi zmanjšali raztapljanje ionov zlitine in njihovo izluževanje v telo, je potrebno modificirati površino. To lahko dosežemo s povečanjem debeline in kakovosti oksidne prevleke, ki je vedno prisotna na površini. Poleg tega je potrebno površino modificirati tako, da bo povečana tudi hitrost vraščanja kosti, s katero bo vsadek tvoril tudi močnejšo vez.

V tem delu smo naravno amorfno oksidno prevleko na površini zlitine spremenili v debelejšo kristalinično s hidrotermalno obdelavo v prisotnosti Ti ionov. S spreminjanjem hidrotermalnih pogojev, kot so temperatura, čas in pH, smo spreminjali morfologijo, velikost kristalov in debelino prevleke. Z uporabo ustreznih dodatkov in površinsko aktivnih snovi smo dosegli želeno morfologijo. Tako pripravljene anatazne prevleke so bile bioaktivne in so imele dobro adhezijo s podlago. Prevleke smo testirali *in vitro* in *in vivo*, pri čemer so celični testi pokazali, da je adhezija in proliferacija celic odvisna od morfologije anataznih kristalov. Prav tako smo pokazali, da različne kristalne ravnine vplivajo tudi na nastanek hidroksiapatita pri testu v simulirani telesni tekočini.

Pokazali smo, da je prevleka iz titanovega dioksida lahko bioaktivna, vendar pa je nastanek hidroksiapatita zelo počasen v primerjavi z bioaktivnimi materiali, kot so na primer hidroksiapatit in drugi kalcijevi fosfati ali bioaktivno steklo. Bioaktivno steklo je biorazgradljiv material z visoko bioaktivnostjo. Je osteokonduktiven in

osteoproduktiven in lahko tvori vez s trdim in mehkim tkivom. Vendar pa ima slabe mehanske lastnosti in zato ni primeren za vsadke, ki morajo prenašati obremenitve. V takih primerih je njegova uporaba omejena na prevleke.

Kombinacija biostekla v poroznih titanovih vsadkih oziroma prevlekah naj bi močno izboljšala osteointegracijo. Vendar pa za takšne prevleke v porozni titanovi strukturi potrebujemo zelo fine delce bioaktivnega stekla. Ker z običajnim postopkom pridobivanja stekla s taljenjem ne dobimo dovolj majhnih delcev, smo razvili t. i. partikularni sol-gel postopek, kjer nastanejo sferični delci nano-velikosti. Te delce smo potem infiltrirali v porozno titanovo prevleko z vakuumsko infiltracijo. Testirali in primerjali smo različne sestave, spremljali njihovo kristalizacijo in sintranje, antibakterijske lastnosti in bioaktivnost ter na koncu potrdili izboljšano vraščanje v prisotnosti bioaktivnega stekla z *in vivo* testi.

Da bi združili lastnosti obeh prevlek, smo nanesli obe prevleki skupaj. Biosteklo bi tako služilo za pospeševanje nastanka nove kosti, anatazna prevleka pa bi preprečevala izluževanje toksičnih kovinskih ionov tudi po tem, ko bi se biosteklo razgradilo in bi ga zamenjala kost.

Abbreviations

a.u. = arbitrary units
AES = Auger electron spectroscopy
at.% = atomic percent
BAG = bioactive glass
CFU = colony-forming units
CNT = calcium nitrate tetrahydrate
DSC = differential scanning calorimetry
EDS = energy-dispersive X-ray spectroscopy
EPR = electron paramagnetic resonance
EtOH = ethanol
FEG = field-emission gun
HAp = hydroxyapatite
HT = hydrothermal treatment
mol.% = molar percent
OD600 = optical density at 600 nm wavelength
PBS = phosphate-buffered saline
SBF = simulated body fluid
SEM = scanning electron microscopy
TEM = transmission electron microscopy
TEOS = tetraethyl orthosilicate
TEP = triethyl phosphate
TG = thermogravimetry
TSB = tryptic soya broth
wt.% = weight percent
XPS = X-ray photoelectron spectroscopy
XRD = X-ray powder diffraction
ZP = zeta-potential
70S = bioactive glass with a composition (mol.%) $70SiO_2$-$30CaO$
58S4Zn = bioactive glass with a composition (wt.%) $58SiO_2$-$30CaO$-$8P_2O_5$-$4ZnO$
58S4Sr = bioactive glass with a composition (wt.%) $58SiO_2$-$30CaO$-$8P_2O_5$-$4SrO$
53S = bioactive glass with a composition (wt.%) $53SiO_2$-$20CaO$-$4P_2O_5$-$23Na_2O$
45S5 = bioactive glass with a composition (wt.%) $45SiO_2$-$24.5CaO$-$6P_2O_5$-$24.5Na_2O$
Vivoxid® = $53SiO_2$-$20CaO$-$4P_2O_5$-$24Na_2O$
NN = sodium nitrate
Sr-A = strontium acetate
Zn-A = zinc acetate
S. *aureus* = Staphylococcus *aureus*

S. *epidermidis* = Staphylococcus *epidermidis*
NBO = non-bridging oxygen
BO = bridging oxygen
NC = network connectivity

1 Introduction

Bone diseases are serious health conditions that have a major influence on the quality of life, particularly among the aged. For centuries, when tissue became diseased or damaged, the offending parts were usually amputated. The removal of bad tissue, such as joints, vertebrae, teeth, or organs elevated the pain and the quality of life was improved only marginally. But during the past century the situation changed dramatically. The goal of all early biomaterials was to achieve a suitable combination of physical properties to match those of the replaced tissue with a minimal toxic response in the host. Over the past few decades, the number of new biomaterials has expanded rapidly, as has our understanding of events that occur when a foreign material is placed in contact with living tissue. From dental repairs to controlled drug release or total organ/joint replacement, almost every human in the civilized world is these days exposed to a biomaterial during their lifetime.[1, 2]

With increasing life expectancy, which is now in the range 80+ years, people outlive the quality of their connective tissues, and therefore the need for replacement tissues is unavoidable. With ageing, the density and strength of the bone tissue decreases. Women are even more vulnerable to this. From 30 to 65 years the bone strength of women decreases by approximately 40 % (that of men by 20 %). Bone density decreases with age because the osteoblasts (cells which generate the bone tissue) become less productive in new-tissue formation and microcrack healing. The decreasing density substantially lowers the strength of the spongy tissue located at the ends of the long bones and vertebrae. A consequence of this is numerous breaks of the hip bone stem in old people, or deformation of the vertebrae and pain in the spinal column. The ageing of bone tissue, bone defects which are formed in the operational removal of cysts, tumours, genetic defects and other bone-tissue-related diseases, together with need for a better life quality claim for materials, artificial or autogenous, that will have long life functionality and survivability under body environmental conditions.[1, 2]

The survivability of implants requires the formation of a stable interface with the living host tissue. A strong bond between the implant and the surrounding tissue must be formed as soon as possible for faster postoperative healing and to avoid later implant loosening. Metal implants that are used in orthopaedics and dental care are required to have some surface modification to promote osseointegration, to protect the surrounding tissue from the release of metal ions from the implant, to possibly protect the surface from bacteria colonization and at least to obtain a hydrophilic surface for better cell attachment. Different coatings have been proposed, and among them are bioactive glass and titania. Bioactive glass is one of the most bioactive materials; it stimulates bone formation, and is also biodegradable, which means that the coating is temporary as it dissolves when in contact with body fluids. Another type is a titania coating that is already naturally formed on Ti metals, but is amorphous and a transformation into the crystalline phase is needed to obtain the above-mentioned properties.

1.1 History of biomaterials

Biomaterials are nowadays used widely throughout medicine, dentistry and biotechnology, whereas only 50 years ago the word biomaterial was even not used. The revolution in biomaterials began 30 years ago. However, people had used materials to replace damaged parts of the body a hundreds of years before. The oldest known non-biological material in the human body was dated to be 9000 years old. Archaeologists discovered a person with a spear embedded in his hip. Romans, Chinese and Aztecs used gold in dentistry more than 2000 years ago. Mayan people (600 A.D.) used nacre teeth from sea shells and apparently achieved what we now refer to as bone integration. Sutures were a relatively common fabricated material for thousands of years; and there is evidence that they may have been used 32000 years ago. Glass eyes, ivory and wooden teeth have also been in common use throughout history. In 1759 a wooden peg and a twisted thread were used to unite the edges of a brachial artery. In 1860 aseptic techniques that enabled some control over implant-related infections were improved. However, most implants prior to 1950 had a low probability of success because of a poor understanding of biocompatibility and sterilization.[1]

In the middle of the 20th century PTFE (Polytetrafluoroethylene; Teflon) began to be used for cardiac valves and vascular grafts and PE (polyethylene) was introduced into plastic surgery. During World War 2 synthetic plastics came into use. It was discovered accidentally that PMMA does not cause infections. Sir Harold Ridley, inventor of the plastic intraocular lenses, had the opportunity to examine warplane pilots who were injured by fragments of their aircraft canopy made from PMMA plastic. The fragments got lodged into their eyes and stayed there for years but the pilots did not suffer adverse chronic infections. Since then PMMA has been used for bone cement.[1]

In the past century, much research has been centred on creating better materials and design to make prostheses that serve patient better, last longer, and look more natural. One of the most notable advances came in the 1960s when Sir John Charnley invented the low-friction total hip arthroplasty, the first of which was implanted around 1962. In 1964 Dr. Branemark named a phenomenon called osseointegration and explored the application of titanium implants in surgical and dental procedures, when he discovered that the titanium screws after several months of implantation were tightly integrated in the bone.[1]

Only a few years later in 1969 bioglasses were discovered by L.L. Hench. By the mid-1980s bioglasses and other bioactive materials had reached clinical use. Synthetic hydroxyapatite ceramics began to be routinely used as porous implants, powders, and coatings on metallic prostheses to provide bioactive fixation. Bioactive glass is a designed biomaterial. It was designed specifically for biomedical applications.[1]

1.2 Types of biomaterials

No material implanted in an organism is absolutely inert. All materials elicit a certain response from a host tissue, i.e., they stimulate a reaction in living tissue. According to contemporary research, biomaterials are defined by four different types of implant-tissue attachment (Table 1). The classes are by no means precise, and there is often a debate about whether a material falls into the bioinert or bioactive categories, as biocompatibility is often dependent on the morphology of the sample, as well as the material. Toxic materials are, because of the death of the surrounding tissue, obviously to be avoided in any implant or tissue-engineering application.[1-3]

Table 1: Classes of biocompatibility[1-3]

Type of biomaterial	Reaction of organism	Material
Biotoxic	Atrophy[1], pathological change or rejection of living tissue near the material as a result of chemical, galvanic, or other process. The surrounding tissue dies.	Alloys containing Cd and other toxic elements, carbon steels, carbides
Bioinert	Coexistence with the material without noticeable change, separation from the material by layer of fibrous tissue of various thickness	Ta-, Ti-, Al- and Zr- oxides
Bioactive	Formation of direct biochemical bonds with the surface of the material and free growth	High density hydroxyapatite and tricalcium phosphate, bioactive glasses
Bioresorbable	Gradual dissolution of the material by the biosystem of the organism, implant replaced by growth of tissue	Tricalcuim phosphate, porous hydroxyapatite, calcium phosphate salts, bioactive glasses

Biomaterials can be divided into four major classes: polymers, metals, ceramics, and natural materials. Another class is combining the different classes of materials forming composite materials, such as ceramic coating on metals or hydroxyapatite particle-reinforced poly(lactid acid). [1-3]

Polymers represent the largest class of biomaterials, they are widely used in orthopaedics, dental, soft tissue and cardiovascular implants. A few examples of polymers used in medicine are collagen, polyethylene, poly(methyl methacrylate), poly(ethylene glycol). Natural materials such as silk, collagen, gelatine, etc. are natural polymers that are very similar or even identical to natural substances, which the biological environment can recognise and deal with metabolically. Therefore, they have the ability to be degraded by naturally occurring enzymes. Metallic implants (Ti and its alloys, stainless steel, Co-Cr alloys) are extensively used in orthopaedics as screws, plates, joints, etc. Ceramic materials include ceramics, glasses and glass ceramics, among which bioactive glasses, hydroxyapatite and other calcium phosphates are used for bone regeneration.[1, 4] Bioactive glasses and Ti alloys are more precisely presented in later chapters.

1.3 Ti-alloys

Titanium-based alloys are among the most common materials implanted into the human body, with the aim of permanently supporting or replacing injured or disease-damaged bone. They are commonly used for artificial bones, joints and for

---

[1] Atrophy: reduction of a cell, tissue, organ or a part of them

dental implants.

Titanium itself is considered a bio-inert material that satisfies the needs for mechanical support relatively well due to its high flexural strength and tolerable elastic modulus. Among other metallic implants it has the best corrosion resistance, chemical inertness and biocompatibility, which are ascribed to the native oxide layer formed on the surface. This oxide layer is formed when the alloy is exposed to air or water and is normally very thin (up to 10 nm), amorphous and nonstoichiometric and is thought to protect an implant exposed to the physiological environment from corrosion. However, recent studies have indicated that when an implant is in direct contact with bone tissue in a complex dynamic system, exposed to mechanical loads and affected by extracellular liquid and proteins, this naturally formed layer does not provide a sufficient long-term corrosion protection, and it is not an efficient barrier for preventing the release of metal ions into the body[5-7]. The release of ions is slow, but continuous. For example; in the case of the Ti6Al4V alloy, titanium is released, as well as harmful alloying elements like aluminium and vanadium[5, 6, 8, 9] that are important constituents of the alloy. After years of continuous release, these metal ions can cause adverse systemic responses, which have been seen as cytotoxicity and genotoxicity, or rarely, but not negligibly, delayed hypersensitivity reactions in some patients[7, 10-14].

1.3.1 Surface modification of Ti-alloys

Since the Ti implants are not bioactive, the osseointegration is limited and there is a risk of the release of toxic ions, different implant designs and surface modifications are used. Different surface modifications have been proposed such as structure modification, chemical treatments and bioactive coatings[15].

Using structure modifications the surface topography is changed in such a way that it improves adhesion and bonding of the bone and thus improves the stability of the implant. The surface can be modified by either surface roughening, machining, grinding, and blasting or by applying a porous metallic layer on the surface of the metallic implant. Such porous metallic coatings with their open and interconnected pores are designed to allow bone to grow into the pores, thus allowing better stability and fixation of the implant. Porous coatings also reduce the large difference in stiffness between the bone and implant[16-18]. The most common way of applying a porous titanium layer on a Ti-alloy implant is vacuum plasma spraying (VPS). Such implants were also used in this study as a substrate material.

For an improvement of the bioactivity of Ti-alloy implants ceramic, glass or glass-ceramic materials can be applied, such as different Ca-phosphates[19] or bioactive glasses. Hydroxyapatite coatings exhibit an osteoconductive capacity based on a similar chemical composition to natural bone and are being used in clinical practice. Bioactive glasses are a biodegradable material with excellent bioactivity and are bonded to both soft and hard tissue. The main function of such coatings is to enhance the osseointegration but was also reported to increase the corrosion resistance and ion diffusion barrier[20, 21]. The long-term protection is however questionable as the protective role of the coating decreases with time and is finally lost due to bio-resorption.

There are many reports on many different methods for applying BAG coatings; however, they are not used in clinical practise yet. Among them are plasma spraying [22], sputtering, electrophoretic deposition[23], pulsed laser deposition[24], sol-gel[20, 25], grit blasting[26], etc. All of the mentioned techniques are able to form a coating on flat surfaces and also some of them on more complex shapes, but none of them is able to coat porous samples. Therefore, we introduced the vacuum infiltration technique to infiltrate the BAG into the pores of the implant with VPS porous Ti-layers on the surface.

To avoid the dissolution of the alloying elements and their diffusion into the body, it is necessary to improve the quality of the native oxide layer and to increase its thickness[15]. This can be achieved by the modification of the surface with chemical treatments, including anodic oxidation, micro-arc oxidation, thermal oxidation, sol-gel, or deposition from TiO_2 suspensions followed by a thermal treatment[15, 27-29]. In most of these processes, the main problems are poor adhesion of the coating, delamination, and phase transformations during the thermal treatment. Methods also do not allow morphological control of TiO_2 particles, which is important for the bioactivity as well as for the cell adhesion.

In addition to the surface-protection effects, artificially made TiO_2-based coatings have been suggested to improve the biocompatibility and bioactivity of implants due to their more stable chemical composition[30, 31]. In contrast to bioactive glass, which dissolves in body fluid, the titania remains as a protective coating on the metallic implants. Titania is also well known for its photocatalytic activity and is potentially attractive for coatings on implants because it can provide a highly efficient, self-sterilizing effect under UV irradiation[32-34].

1.3.1.1 Hydrothermal (HT) treatment

Hydrothermal processing is defined as any heterogeneous reaction in a closed system in the presence of aqueous media above room temperature and at pressures greater than 1 atm. For the chemical reactions in the presence of a non-aqueous solvent, the term solvothermal is used. The material that is relatively insoluble under ordinary conditions, goes into solution under the action of mineralizers or solvents, to dissolve and recrystallize. Due to the specific physical properties, particularly the high solvation power, high compressibility, and mass transport of the solvents, different types of reactions occur: [35, 36]

- Synthesis of new phases or the stabilization of new complexes,
- Crystal growth of several inorganic compounds,
- Preparation of finely divided materials and microcrystallites with well-defined size and morphology for specific applications,
- Leaching of ores in metal extraction,
- Decomposition, alteration, corrosion, etching.

Pressure is controlled, either externally or by the degree of filling and temperature in a sealed vessel.

The reactions during the hydrothermal synthesis are controlled by thermodynamic variables such as temperature, pH, concentrations of reactants and additives. The phenomena that underlie the size and morphology control using the thermodynamic variables are the overall nucleation and growth rates, which control the crystal size, and the competitive growth rates along principal crystallographic directions that control the morphology. The size of the crystals can therefore be controlled by varying the temperature and the concentration. The crystal morphology and the size can be additionally affected by surfactants, which can adsorb on specific crystallographic faces and solvents, which adsorb similarly as well as regulate solubility.[35] The reactions between the components of a thermodynamic system can be characterized by thermodynamic state functions (thermodynamic potentials) depending on the state variables. The most important state function in thermodynamic modelling is the Gibbs free energy (G), given by:

$$\Delta G = \Delta H - T\Delta S \tag{1}$$

with enthalpy (H), temperature (T) and entropy (S).

The above expression shows the influence of enthalpy and entropy on the equilibrium constant, so that the enthalpy and entropy of the solubility (at constant P and T) are different for different solvents, also the solubility of the same solid substances changes with the solvent. Whether considering nucleation or growth, the reason for the transformation from solution to solid is the same, i.e., the free energy of the initial solution phase is greater than the sum of the free energies of the crystalline phase plus the final solution phase. [37, 38]

Relative to solid-state processes, liquids give the possibility of the acceleration of diffusion, adsorption, reaction rate and crystallization, especially under hydrothermal conditions. All forms of ceramics can be prepared under hydrothermal conditions, i.e., powders, fibres, single crystals and also coatings on metals, polymers or ceramics.[35]

When a hydrothermal treatment is used for the preparation of a coating, nucleation starts on a foreign surface. The presence of a foreign surface can be used to exert even greater control over the nucleation because, quite often, the interfacial energy between a crystal nucleus and a solid substrate is lower than that of the crystal in contact with the solution. This is because the atoms in the crystal can form bonds with those in the substrate that are stronger than the bonds of solvation. Because the enthalpy contribution to the free energy comes primarily from chemical bonding, stronger bonds lead to a smaller interfacial free energy. Clearly, the strength of bonding at the interface is strongly dependent on the structure and chemistry of the substrate surface. If the atomic structure of the substrate surface closely matches a particular plane of the nucleating phase so that lattice strain is minimized and, in addition, the substrate presents a set of chemical functionalities that promote strong bonding to the nucleus, then the enthalpic contribution to the interfacial free energy becomes small, and nucleation occurs preferentially on that crystal plane.[38]

Hydrothermal synthesis is usually conducted in a steel pressure vessel known as an autoclave, or a reactor or a high-pressure bomb. Usually, autoclaves are made from stainless steel and have a Teflon liner that is placed inside the steel autoclave in order to prevent corrosion, as autoclaves have to be inert with respect to the solvent. One of the most popular types of autoclave is presented in Figure 1.[37]

Figure 1: Example of an autoclave with a Teflon vessel.

1.3.1.2 TiO_2 coatings prepared by hydrothermal treatment

TiO_2 is one of the most studied materials prepared by hydrothermal synthesis. Knowledge from the synthesis of powder can be transformed to the synthesis of coatings as the major difference is only in the nucleation site. Summarized by Bayrappa[37], the synthesis of TiO_2 is usually carried out in autoclaves with Teflon vessels at relatively low temperatures, up to 200 °C and pressure up to 100 bars. Different solvents are used, such as NaOH, KOH, HCl, HNO_3, HCOOH and different starting charges such as reagent-grade anatase, sintered anatase, $TiCl_4$, titanium alkoxide or titania gel formed from alkoxide can be used. According to the solvents and starting charges, different polymorphic forms of anatase can be produced, rutile, anatase or brookite, or a mixture of them. In biomaterials some reports suggests that anatase has a better bioactivity than rutile and brookite[39]. For the formation of a single phase, the temperature and pH of the media are of great importance too. When the pH of the medium is low, the product is usually rutile. As the pH increases, essentially anatase phase is formed and is even more favoured when NaOH is added. Beyond pH 12 amorphous materials can be obtained. To alter the particle shape and size and to enhance crystallization different additives have been used, such as F-, K+, HNO_3, tetrametyl ammonium hydroxide or tetrabutyl ammonium hydroxide, etc[37].

Several attempts have also been made to form a TiO_2 layer on the surface of Ti and different Ti-alloys by a hydrothermal (HT) treatment. Often TiO_2 is applied by some other method and is then crystallized by an additional hydrothermal treatment.

Beusen et al. hydrothermally synthesised anatase particles which were deposited on a Ti-alloy by tape casting[40]. Ueda et al. [41, 42] synthesised TiO_2 layers on Ti and Ti-Nb by the HT crystallization of amorphous TiO_2, which was prepared on the metal surface using a chemical pre-treatment with a H_2O_2/HCl solution. The TiO_2 formed on the metal substrates was identified as anatase; however, Nb was detected as an impurity in the surface TiO_2 layer[41, 42]. Cheng[43] hydrothermally treated amorphous sol-gel-prepared TiO_2 layers on NiTi substrates. Liu et al.[44] hydrothermally treated micro-arc oxidized titania films. Without any pre-treatment of the metal surface Obata et al.[45] HT synthesised the TiO_2 polymorphs anatase and brookite on Ti metal in a diluted NaOH solution. Similarly, Wong et al.[46] HT synthesized an anatase film on a NiTi alloy by HT just in water which improved the corrosion resistance but did not induce HAp formation. Divya Rani et al.[47] grew nanoleaves, nanoscaffolds and nanoneedles by hydrothermal treatment in a diluted NaOH solution, of which only the nanoneedles resemble anatase crystals, but it resulted in the formation of fibrous tissue when implanted into a rat.

1.4 Bioactive glasses (BAG)

Bioactive glasses were discovered by L.L. Hench and colleagues in 1969. They found out that a certain group of calcium-rich glasses could form a chemical bond with bone. Since this discovery, bioglasses have been used in many clinical applications, such as drug-delivery systems, bone cements, filling defects left from the removal of teeth, devices for implant into the middle ear, and also in facial reconstruction. Due to their poor mechanical properties bioactive glasses cannot be used in load-bearing applications, where metallic alloys are still the material of choice. But can be used as a coating for metal implants in order to improve implant bioactivity.[3, 48, 49]

Bioactive glasses have an ability to repair and to rebuild damaged tissues, particularly hard tissues. They possess their bioactivity because the components of the glass are similar to those which contain hydroxyapatite; so once the glass dissolves, the dissolution products nucleate hydroxyapatite formation at silanol Si-OH groups on the glass surface. Their osteoconductive behaviour enables them to bond to hard as well as to soft tissue.[49, 50]

The similarity of bioactive glasses to other bioactive ceramics is a time-dependent, kinetic modification of the surface that occurs after implantation. The surface forms a biologically active hydroxycarbonate apatite layer, which provides the bonding interface with the tissue. The hydroxycarbonate apatite phase that forms on bioactive implants is equivalent, chemically and structurally, to the mineral phase in bone. It is that equivalence that is responsible for the interfacial bonding. On the other hand, they differentiate from bioactive ceramics or glass ceramics in the possibility to tailor their chemical composition and linking speed to the tissues. Therefore, it is possible to design glasses with tailored properties for a specific clinical application.[49, 50]

The bioactive glass ability of bonding to bone was first demonstrated for only a certain compositional range of bioactive glasses, which contained SiO_2, Na_2O, CaO and P_2O_5 in specific proportions. There were three key compositional features to these bioactive glasses that distinguished them from traditional soda-lime-silica glasses[49]: higher mol.% SiO_2, high Na_2O and CaO content, and high CaO/P_2O_5 ratio. Those bioactive glasses were prepared by melting at high temperatures.

By introducing the sol-gel method for bioactive glass production, the bioactivity broadens to a larger range of its composition. The higher surface area and nanoporosity of sol-gel derived bioactive glass makes it bioactive even for amounts of silica as high as 90 mol.%.[50, 51]

Bioactive glasses are bioresorbable materials, and besides bone bond formation their ionic dissolution products were shown to stimulate angiogenesis. Certain compositions of bioactive glasses increase the secretion of angiogenic growth factors from fibroblasts and can induce infiltration of an increased number of blood vessels into the tissue[52-54]. The released ions also showed antibacterial and inflammatory effect[55-57]. A schematic overview of the biological responses to bioactive glass ionic dissolution products is presented in Figure 2.

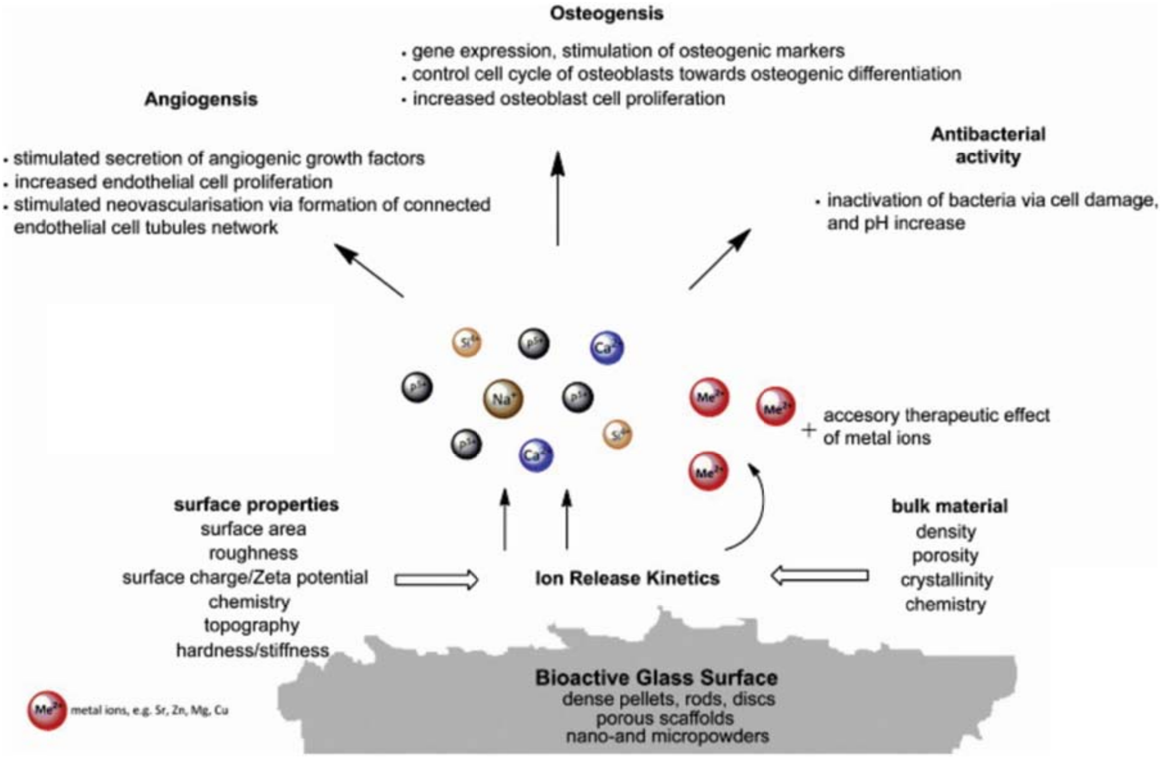

Figure 2: Biological responses to ionic dissolution products of bioactive glasses.[58]

1.4.1 Bioactive glass structure

The main feature of bioactive glass is its bioactivity, which is strongly connected to the glass structure. Therefore, a brief introduction to the glass structure is presented below in order to understand the connection with bioactivity.

Silicate glasses are defined as amorphous solids that are characterized by a network of covalent SiO_4 tetrahedrons, linked together by bridging oxygens (BO) where each oxygen atom is shared by two Si atoms which occupy the centres of linked tetrahedra. The short-range order is similar to the crystalline counterparts, while there is no long-range order present. Amorphous SiO_2 is characterized by a continuous network interconnected in three dimensions, with every tetrahedron linked by four BOs to four adjacent tetrahedra. The addition of network modifiers (alkali and alkali earth metal cations) replaces BO with non-bridging oxygen (NBO). Ionic bonds between NBOs and network modifiers ensure the local charge balance and the overall charge neutrality. The concentration of NBOs increases, and the concentration of BOs decreases directly in proportion to the alkali oxide content.[59] A two-dimensional drawing of a bioactive glass structure is shown in Figure 3.

The bioactivity of BAG is connected with its network connectivity (NC) that is defined as the average number of BO atoms per silicon in the glass network. It is a general rule that glasses with NC values over 2.4 have negligible bioactivity and it is increased towards the value of 2.0, which corresponds to silicate structure where each silicon atom has on average two NBO and two BO (Q^2 structure; two silicon atoms are bonded to another silicons).[60, 61] The dissolution and bioactivity are controlled by NC, so the addition of modifiers decreases the NC by increasing the number of NBO and thus the solubility of the glass.

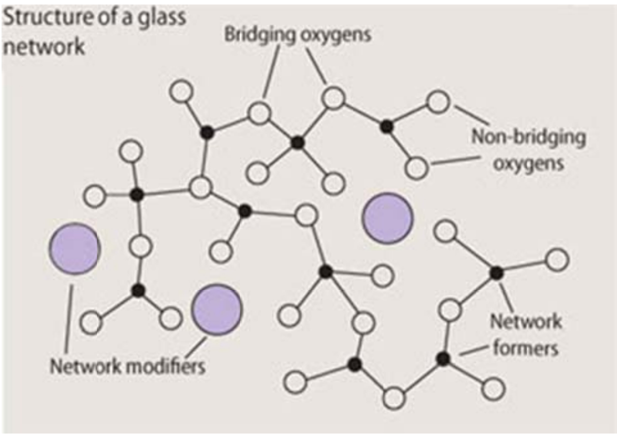

Figure 3: Structure of bioactive glass network[62]. Network modifiers are disrupting connectivity of glass structure by forming NBOs.

1.4.2 Bonding of bone to bioactive glasses

Bioactive glasses as well as other bioactive materials (glass ceramics, sintered hydroxyapatite, tricalcium phosphate) bond to living bone trough the apatite layer, which is formed on their surfaces in the living body under body environmental conditions. This apatite is a carbonate containing hydroxyapatite with small crystallites and a defective structure, which is very similar to the apatite in the bone in its composition and structure. Therefore, the bone-producing cell, the osteoblast, can preferentially proliferate, differentiate and mineralize to produce apatite and collagen on this apatite layer. As a result the surrounding bone can come into direct contact with the surface apatite without the intervention of the fibrous tissue. When this occurs a tight chemical bond is formed between the bone apatite and the surface apatite in order to reduce the interface energy between them[63].

In vitro the bone-bonding ability of a biomaterial, the so-called bioactivity, can be predicted from the apatite formation on its surface in simulated body fluid (SBF) with the ion concentration nearly equal to that of human blood plasma. The composition similarity of SBF and human blood plasma is shown in Table 2. It is clear that bioactivity is not only a material property but also depends on the solution used for *in vitro* tests[64]. Therefore, *in vitro* tests must create similar conditions as *in vivo*.

Table 2: Ion concentration of SBF and human blood plasma

	Ion concentration (mM)							
	Na^+	K^+	Mg_2^+	Ca^{2+}	Cl^-	HCO_3^-	HPO_4^{2-}	SO_4^{2-}
Human blood plasma	142.0	5.0	1.5	2.5	103.0	27.0	1.0	0.5
SBF	142.0	5.0	1.5	2.5	148.8	4.2	1.0	0.5

It is thought that there are 5 stages to the formation of hydroxyapatite on bioactive glasses in solution[2, 49]:

- FORMATION OF Si-OH BONDS: Exchange of Na^+ (or K^+ or Ca^{2+}) ions from the surface of the glass with H^+ or H_3O^+ ions from solution, leading to the formation of silanol (Si-OH) groups on the surface:

  $$\text{Si-O-Na} + H^+ + OH^- \rightarrow \text{Si-OH} + Na^+ \text{ (solution)} + OH^+ \qquad (2)$$

  This stage is usually controlled by diffusion

- FORMATION OF SiOH BONDS AND RELEASE OF SOLUBLE SILICA: Loss of soluble silica in the form of $Si(OH)_4$ to solution, resulting from breaking of Si-O-Si bonds and the formation of further silanols (Si-OH) at the glass solution interface:

  $$\text{Si-O-Si} + H_2O \rightarrow \text{Si-OH} + \text{OH-Si} \qquad (3)$$

  This stage is usually controlled by interfacial reaction

- POLYCONDENSATION: Condensation and repolymerization of a SiO_2-rich layer on the surface depleted in alkalis and alkaline-earth cations, to form hydrated silica gel:

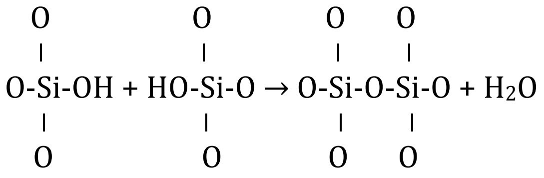

$$\text{O-}\overset{\displaystyle O}{\underset{\displaystyle O}{\text{Si}}}\text{-OH} + \text{HO-}\overset{\displaystyle O}{\underset{\displaystyle O}{\text{Si}}}\text{-O} \rightarrow \text{O-}\overset{\displaystyle O}{\underset{\displaystyle O}{\text{Si}}}\text{-O-}\overset{\displaystyle O}{\underset{\displaystyle O}{\text{Si}}}\text{-O} + H_2O \qquad (4)$$

- ADSORPTION: Migration of Ca^{2+} and PO_4^{3-} groups on the surface through the SiO_2-rich layer forming a calcium phosphate (CaO-P_2O_5) rich film on top of the SiO_2-rich layer, followed by the growth of the amorphous calcium phosphate-rich film by the incorporation of soluble calcium and phosphate from the solution

- CRYSTALLIZATION OF HCA: Crystallization of the amorphous CaO-P_2O_5 film by incorporation of OH^-, CO_3^-, or F^- anions from solution to form a mixed hydroxyl, carbonate, fluoro-apatite layer.

A schematic presentation of those five stages is presented in Figure 4 on two component glasses SiO_2-CaO and SiO_2-Na_2O[65].

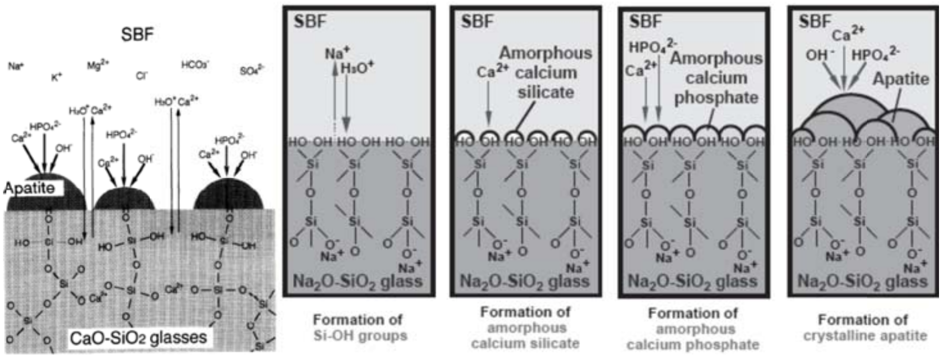

Figure 4: Mechanism of apatite formation on a) a CaO-SiO_2 glass[63], b) a Na_2O–SiO_2 glass in SBF.[65]

The first five stages occur on the glass side and do not depend on the presence of tissue. They are then followed by six biological stages, summarized in Figure 5.

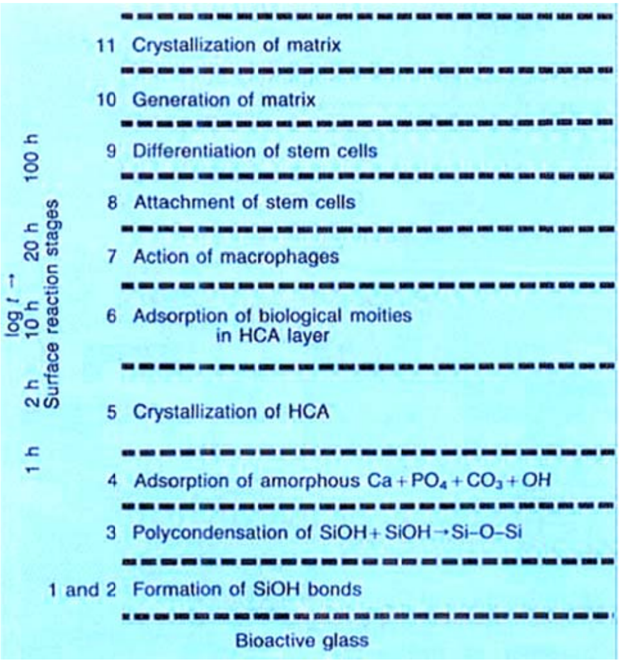

Figure 5: Sequence of interfacial reactions involved in forming a bond between a bone and a bioactive glass.[2, 3, 49]

The *in vitro* bioactivity of bioactive glasses is affected by many factors including composition, texture, porosity, density and crystallinity. All of these factors influence the dissolution rate of BAG.

The influence of composition was already evident in the first bioactive glasses, where only a certain range of compositions were bioactive. Later, by introducing the sol-gel synthesis of BAG the range of compositions that are still bioactive was greatly extended. The composition of BAG has a major influence on the network connectivity that is the most important feature influencing the solubility and thus the bioactivity of the glasses[66, 67].

The crystallization of BAG is undesirable because it reduces the bioactivity since the crystal phases are in a lower energy state, the structure is more tightly packed, the bonding is stronger and thus the crystal phase is less soluble[68, 69]. In general, bioactivity increases with decreasing network connectivity. Thus the dissolution rate of BAG increases with the addition of network modifiers that are responsible for forming non-bridging oxygens.[60, 66] Therefore, the composition of glass is not important just for the released ions but also for the glass network that is responsible for the rate of glass dissolution. Silica, as a network former, forms OH groups during the dissolution of glass, which are the nucleus sites for hydroxyapatite (HAp) precipitation. Other oxides in a composition are important for disrupting the silica network and making it less connective.

More recently, it was observed that the formation of a HAp layer is not a critical stage of the reaction for bone regeneration. The bioactivity is important, but more critical is the dissolution of ionic products from the bioactive glass, especially the critical concentration of soluble calcium and silica ions. The released ions stimulate the expression of several families of genes, including genes encoding the nuclear transcription factor, and activates growth factors, especially IGF-II along with IGF binding proteins and proteases that cleave IGF-II from their binding proteins. The response of those genes and the activation of growth factors modulate the cell cycle response of osteoblasts to bioactive glass. The osteogenesis (new bone formation) is controlled by the genes.[50, 70-73]

1.4.3 Sol-gel bioactive glasses

1.4.3.1 Sol-gel

Sol-gel is a process which enables the preparation of a glass without melting. Glass, ceramics and composites can be prepared by the sol-gel technique at much lower temperatures than conventional techniques. In the sol-gel process the starting compounds also called precursors consist of metal or metalloid elements surrounded by various ligands. The common precursors for oxides are inorganic salts, such as nitrates, and organic compounds, such as alkoxides.[74]

Sol is a different name for a colloid suspension of submicrometer- and nanometer-sized particles in a liquid. If those particles have surface-active groups, like hydroxyl groups, under specific conditions the condensation reaction can start and the particles can bond together. Water or solvent, which are condensation products, are trapped between the sol particles, i.e., sol matrix, thus forming an intermediate product called a gel. The gel is a semisolid with a liquid trapped in the pores. During gelation M-O-M (M is a metal atom) bonds are formed (or Si-O-Si) with a controlled hydrolysis of the metal alkoxides. The most common and most widely studied precursors are tetraethoxy silane (TEOS) with the formula $Si(OC_2H_5)_4$ and tetramethoxysilane (TMOS) with a formula $Si(OCH_3)_4$. These precursors are also the main starting compound for sol-gel bioactive glass synthesis.[74]

Metal alkoxides react with water; hydroxyl ion becomes attached to the metal atom. The reaction is called hydrolysis[74]:

$$\text{Si-(OR)}_4 + \text{H}_2\text{O} \rightarrow \text{HO-Si(OR)}_3 + \text{R-OH} \qquad (5)$$

Depending on the amount of water and catalyst, hydrolysis can stop when the metal is only partly hydrolysed, as written above, or it can go to completion[74]:

$$\text{Si-(OR)}_4 + 4\text{H}_2\text{O} \rightarrow \text{Si(OH)}_4 + 4\text{R-OH} \quad (6)$$

Partially hydrolysed molecules then link together by condensation. The reaction where larger and larger molecules are formed by condensation is called polymerization. The polymerization, to form siloxane bonds, occurs by either an alcohol or water condensation reaction[74]:

$$\text{(OR)}_3\text{Si-OR} + \text{HO-Si(OR)}_3 \rightarrow \text{(OR)}_3\text{Si-O-Si(OR)}_3 + \text{R-OH} \quad (7)$$

$$\text{(OR)}_3\text{Si-OH} + \text{HO-Si(OR)}_3 \rightarrow \text{(OR)}_3\text{Si-O-Si(OR)}_3 + \text{H}_2\text{O} \quad (8)$$

During the polymerization of the monomers three-dimensional particles are formed with OH groups on their surface, which serves as nuclei for further growth. This further growth occurs by Ostwald ripening. Particles grow in size as highly soluble small particles dissolve and re-precipitate on larger, less soluble ones. The growth stops when the solubility between the smallest and largest particles becomes only a few ppm. However, further growth can be achieved at higher temperatures and higher pH (above 7).[74]

The above-described mechanism where a solution of monomers is condensed to the cross-linked polymer corresponds to the formation of a sol. However, two types of sol can be formed, as described by Brinker[74], polymeric and particulate. The factor broadly distinguishing the systems is that particulate sols consist of dense particles rather than polymeric clusters. A polymeric sol is defined as a colloid in which the solid phase contains no dense (non-fractal) particles larger than 1nm, whereas the particulate system has particles larger than 1 nm.[74]

Below pH 7 condensed species aggregate to form chains and a network that extends through the liquid medium and is thickened into a silica gel, where pores are filled with water or ethanol. The process of gel formation is slow but can be accelerated with a catalyst, acid or base. If the reaction is catalysed by acid the product is a chain and if it is catalysed by a base the product is more branched. The residual liquid phase left in the gel is eliminated by drying. A dried gel, also called xerogel, still contains some water in form of OH groups. If no catalyst is added the gelation can go up to 1000 h.[74]

At pH above 7, due to the greater solubility, the growth of primary particles continues by Ostwald ripening. If no salts are added, no chaining or aggregation occurs, and the particles are repulsive. When salts are added, as it is necessary for BAG containing oxides other than silica, the aggregation of particles occurs due to the reduced thickness of double layer. Such a particulate sol or colloids can remain stably suspended or can be further aggregated into a particulate gel and aged, or grow so large that they settle out of suspension. Colloids can then be dried to obtain a powder used for further sintering or melting.[74]

1.4.3.2 Bioactive glasses prepared by sol-gel

The sol-gel bioactive glasses are prepared at much lower temperatures than conventional melt-derived glasses. The presence of network modifiers, which open the Si-O-Si bonds, reduces the melting temperature of the melt-derived glasses, but temperatures above 1300 °C are still needed to prepare the glass. On the other hand, sol-gel synthesis allows the preparation of glasses at much lower temperatures (usually around 600 °C). The use of sol-gel expands the bioactive compositional range up to 90 % of SiO_2 and also allows a wider compositional range[75]. To obtain bioactive properties in melt-derived BAG the composition has to be within a certain range (5-17 P_2O_5, 20-50 CaO, 20-55 SiO_2 and 10-50 Na_2O). Glasses with a higher SiO_2 content are inert[50]. However, in sol-gel derived BAG a larger amount of silica means a higher concentration of silanols, more nucleation sites for HAp and therefore better bioactivity. No source of Na is needed for reducing the melting temperature in sol-gel. The BAG composition prepared by sol-gel can be as simple as SiO_2-CaO. This two-component BAG was proven to be as bioactive as melt derived 45S and 58S[76-80]. The higher bioactivity and the higher rate of dissolution was ascribed to the larger surface area and the textural features, such as the pore size[51, 81, 82]. A higher surface area of sol-gel glasses is also beneficial for the adhesion of cells on the glass surface[83].

Besides better bioactivity, sol-gel prepared BAG also has a higher degree of purity as the starting reagents are liquids and not powders, and therefore also a higher homogeneity. Any contamination with impurities during milling that is necessary to form smaller particles of melt-derived glass is therefore avoided. Simplified compositions allow us to avoid he addition of Na_2O that is added to reduce the melting temperature in melt-derived glasses. Due to this the low-temperature process coatings and thin films are easier to make. On the other hand, large pores, large shrinkage and crack formation during gel drying negatively affect the mechanical properties.

Using the sol–gel process, bioactive glass and other ceramic and glass materials can be fabricated in various forms: fibres, powders, films, monolithic materials, highly porous aerogels, microporous membranes, etc. [76]

Starting precursors for sol-gel bioactive glass are, due to their availability, alkoxides TEOS for SiO_2 and triethyl phosphate for P_2O_5 and usually inorganic salts for CaO, Na_2O, MgO etc. For Ca, calcium nitrate is most often used, as calcium alkoxide is very easily hydrolysed and the procedure is therefore much more complicated[84]. Na, Zn, Sr and other oxides can be added to the glass in the form of nitrates acetates or also alkoxides. The introduction of nitrates, also called the inorganic sol–gel route, demands a thermal treatment at temperatures of 500 °C to 800 °C in order to remove the residual salt, but the decomposition temperature of the salts into oxides is often higher than the crystallization temperature of the bioactive glass.

The method in used literature for BAG preparation using the sol-gel process is the polymeric sol-gel route. The process involves the hydrolysis of TEOS and TEP under acidic conditions. Usually, nitric acid is used and is followed by slow gelation at slightly increased temperatures[85-87], although other acids such as lactid acid[88] or acetic acid[89] can be used. Several attempts have been made in order to decrease the particle size by accelerating the gelation reaction using a basic catalyst such as NH_4OH[90-92], where the base is added after the hydrolysis is completed.

Only a couple of reports were found where the sol-gel BAG synthesis was held under basic conditions [93, 94]. Meiszterics et al. used NH_4OH as a catalyst for both the hydrolysis and condensation reactions, but the synthesis was unsuccessful as they report about unwanted calcium salts precipitation[93]. In another study, Labbaf et al. prepared two-component BAG SiO_2-CaO by the formation of spherical SiO_2 particles using a Stöber process[95] with ammonia as the catalyst. Calcium nitrate was introduced into the system when SiO_2 particles were already precipitated and was deposited on the silica particles. As Ca had to diffuse into the particles from their surface, after they were already formed, they had problems to incorporate Ca into the network and were able to obtain the composition only with a maximum of 15 mol.% of calcium.

1.4.4 Antibacterial properties of bioactive glasses

The presence of an implant in the human body is known to increase susceptibility to infection, activating the host defence and host immune systems. The sources of contamination with bacteria during the surgery are the patient's or medical personnel's skin and the air in the surroundings. After the implantation there is an immediate beginning of the so-called race for the surface, involving extracellular matrix (ECM) proteins, fibroblasts, osteoblasts, endothelial cells and also bacteria. At first a conditioning film of ECM proteins is acquired. This film is a biologically active layer composed of a complex mixture of macromolecules (fibrinogen, fibronectin, collagen, albumin, vitronectin). Host cells' adhesion, migration, proliferation and differentiation are all influenced by the composition and structural organization of the surrounding ECM, which not only serves as a substrate for host cells but also for colonizing the bacteria[96]. Therefore, for good implant ingrowth good antimicrobial conditions have to be achieved. Bacterial infections thus prevent the adhesion and growth of the bone tissue, which can lead to longer healing, possible implant failure, revision surgery or, in the worst case, amputation.

Implant-related infections are commonly caused by S. *aureus* and S. *epidermidis*. S. *aureus* is a common cause of metal-biomaterial, bone joint and soft-tissue infections, while S. *epidermidis* is more common with polymer-associated implant infections. Both of these staphylococci strains are capable of producing a biofilm, which means that bacteria attach to the surface of an implant followed by other bacteria, thus forming multiple layers of bacteria where the bacteria on the interior of such a biofilm are protected from antibiotics and phagocytosis[96]. To avoid bacteria colonization the implant surface has to be modified in a way to prevent bacteria from attachment. Antibiotics are used to prevent infection and can also be included in a coating as well as in inorganic components. In the case of the BAG coating different metal ions, but most often Ag^+ ions, are applied[56, 97-99]. Those ions have a broad spectrum of bactericidal activity even at low concentrations [56]. Different mechanisms for the killing of bacteria are documented, but the most important is surface binding and damage of the membrane function. The use of silver in medicine has to be precisely controlled as it can be toxic, not just for bacteria but also for human cells, and also widespread and uncontrollable use may result in bacteria developing resistance, which however is less likely than a resistance to antibiotics[100].

Instead of Ag_2O some other oxides such as ZnO, SrO or CeO and CuO can be added. Zn is considered as an antiseptic material[101], however there are not many reports in the literature about Zn being added to BAG to inhibit bacteria growth or attachment[102-104]. It was proven that the released Zn^{2+} ions cleave the phosphate diester bond and the cleavage of DNA which leads to bacterial distraction when Zn is added to HAp[105] and that Zn^{2+} ion released from biomaterials have antibacterial efficacy, killing many bacterial strains commonly associated with infection after orthopaedic surgery[104]. ZnO-containing glasses were shown to have a stimulating effect on osteoblast cells, and they increase alkaline phosphatase activity and osteoblast proliferation[106]. However, there are many controversial studies contradicting this positive effect, some also indicating the toxic effect of Zn^{2+} ions, especially at higher concentrations (2–8 ppm)[107-109].

A. Guida et al. studied the effect of Sr added in glass ionomer cements dental materials as strontium has been suggested to have a caries-inhibitory role[110]. The antibacterial activity was related to the ability of material to interfere with the bacterial metabolism and growth and was not caused by a pH increase, as in glass cements the pH is minimally reduced and not increased. The addition of SrO in BAG is beneficial for bone formation[111-113]. Similar to strontium-renalate, used as an osteoporosis cure, Sr-substituted BAG promotes an anabolic effect on osteoblasts and an anti-catabolic effect on osteoclasts[111]. According to Lin et al.[114] Sr also has some antibacterial properties when added to hydroxyapatite. The antibacterial properties of Sr-substituted hydroxyapatite, were improved compared to the non-substituted[114].

Copper-containing phosphate-based glasses were also shown to have antibacterial properties[115] as well as cerium, known by its lower cytotoxicity compared to Ag^{+} doped glasses[116].

Bioactive glass has been shown to have antibacterial properties, also without the above-mentioned additions. The antibacterial properties of BAG are ascribed to a pH change and the concentration of the released ions[117]. When ions are released and exchanged with ions from surrounding fluids, the pH increases. Alkaline pH is important for HAp nucleation and crystallization, and at the same time it is believed to have a great effect on bacteria, which has already been reported by several authors[55, 118-121]. Bioactive glass powders that reached the highest pH values during dissolving also had the greatest effect on the bacteria (S. *epidermidis*, S. *aureus*, E. *faecalis*, S. *mutans*)[57]. The influence of pH was confirmed by Allan et al., who got the same results when the pH was raised with NaOH instead of with particulate bioactive glass powder [119]. Zhang also showed that besides pH there is a strong possibility that a high concentration of released calcium and other metallic ions aids the antimicrobial effect. Similar conclusions were made by Vaahtio et al. who observed the effect of Ca^{2+} ions released from CaPSiO ceramics[122]. A high concentration of released calcium and other ions cause the perturbation of the membrane potential of the bacteria. The negative potential of the cell membrane is depolarized by the release of the alkali ions. The effect of metallic oxides, ZnO, MgO and CaO, was also evaluated quantitatively by J. Sawai et al. [123]. Again, the CaO was the most effective.

Using oxides as antimicrobial agents has recently attracted much interest due to the better stability relative to organic (antibiotics).

2 Aims and Hypothesis

The Ti6Al4V alloy is one of the most common materials being implanted into the human body with the aim to permanently support or replace injured or disease-damaged natural bone. The alloy satisfies the need for mechanical support, but unfortunately contains harmful elements, like aluminium and vanadium, both known as cytotoxic and genotoxic. When attached in a direct contact with bone tissue in a complex dynamic system, exposed to mechanical loads and surrounding body fluids, those elements are gradually released into the body. Moreover, the material as such cannot form strong interfacial chemical bonding with the bone and in comparison with bioactive materials, its osseointegration rate is slow. Therefore, our aim was to prevent any direct contact of the metal with the surrounding tissue and thus reduce the release of metal ions from the alloy and to increase the alloy's bioactivity.

Both a reduced ion release and improved bioactivity can achieved by applying a coating such as titania, where the chosen technique is hydrothermal treatment of Ti-alloy implant. In comparison with other techniques, a hydrothermal treatment enables the formation of a coating on complex and porous surfaces. By changing the procedure conditions and additives, a different titania morphology can be achieved and the one suitable for cell attachment, proliferation and bioactivity can therefore be chosen.

Even better bioactivity can be achieved with a bioactive glass coating on a Ti-alloy. According to the literature data a bioactive glass can strongly improve the growth of bone tissue as well as the surrounding soft tissue. Usually, bioactive glass is prepared by a melting method that is inappropriate for applying coatings into porous implants due to bigger particles than the pores themself. The milling of such glass, in order to obtain smaller particles, leads to contamination of the powder, which subsequently prevents its use for biomedical applications. Therefore, our aim was to prepare nano-sized bioactive glass particles and to develop a coating technique that would successfully coat the inner side of the pores in the porous implant with bioactive glass powder, and not just the top surface of the pores, as achieved with other known techniques, such as different spraying techniques, dip-coating, etc.
The chosen technique for that was vacuum infiltration.

The more specific aims and goals were as follows:

- To study the influence of hydrothermal conditions on coating morphology
- To verify the bioactivity of TiO_2 coating in simulated body fluid
- To study the correlation between coating morphology and bioactivity and cell adhesion and proliferation

- To prepare a more hydrophilic surface by applying a TiO_2 coating
- To develop sol-gel synthesis for the preparation of nano-sized bioactive glass particles
- To compare different bioactive glass compositions by means of bioactivity, antibacterial properties and crystallization
- To verify the influence of pH and the silica network on bioactivity and antibacterial properties
- To apply both coatings together and to verify the interaction of BAG with the substrate material and the possible effect of the TiO_2 interlayer
- To test coatings *in vivo*, specifically to compare bone ingrowth of non-coated and BAG coated implants.

3 Materials and Methods

3.1 Substrate materials

The experiments were performed with disc-shaped samples of Ti6Al4V (grade 5, UNS R56400) with a diameter of 15.5 mm, thickness of 2 mm, and mean surface roughness R_a of 0.21 µm (Helipro d.o.o., Slovenia) and composition of 6 wt.% Al, 90 wt.% Ti 4 % V, max 0.25 wt.% Fe and max 0.2 wt.% O, as well as titanium dental screws (grade 2, LIMA spa, Italy) and porous titanium-coated Ti6Al4V cylinders (Alhenia AG, Switzerland). The substrates are presented in Figure 6.

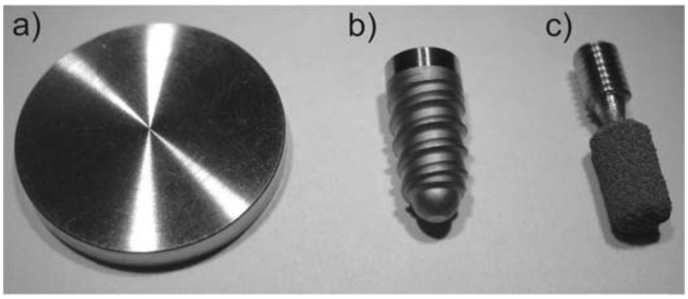

Figure 6: Substrate materials: (a) Ti6Al4V discs, (b) Ti dental screw, (c) porous Ti-coated Ti6A4V cylinder.

3.2 Sample preparation

3.2.1 Hydrothermal synthesis of TiO_2 coating

Prior to any HT treatment the substrates were ultrasonically cleaned with acetone, rinsed in distilled water and dried in air. The treatment was performed at different pH values with (HT B, C, D, E, F) or without the addition of titania (HT A) in the form of either TiO_2 anatase powder (samples HT B, C, D, E) (0.5 µm, Fluka AG, CH) or Ti(IV)-hydroxide (HT F) precipitated by the hydrolysis of Ti-isopropoxide ($Ti(iOPr)_4$, Alfa Aesar GmbH & Co., Germany) in distilled water. The Ti6Al4V substrates were placed into a Teflon container, half filled with a 2.5, 5 or 30 wt.% water suspension of TiO_2 or $Ti(OH)_4$ containing 0.4 mol/l Ti(IV) or with a NaOH or NH_4NO_3 solution. The additives used for the hydrothermal treatment were NaOH, TMAH, ammonium citrate, citric acid, CaF_2 (Kemika, Croatia). The Teflon container was placed in a stainless steel autoclave treated at 150 °C or 200 °C for 24 h. After the HT treatment the autoclave was left to cool to room temperature with a cooling rate 0.5 °C/min and the samples were then ultrasonically cleaned in distilled water before any further characterization.

3.2.2 Preparation of bioactive glass coating

3.2.2.1 Sol-gel bioactive glass synthesis

Bioactive glass (BAG) was prepared by polymeric or particulate sol-gel synthesis. Four different compositions were tested, named 70S, 53S, 58S4Zn and 58S4Sr. Their compositions together with the compositions of two commercial BAGs used in this study for comparison are described in Table 3. The targeted compositions prepared in this study were chosen according to reports, which described them as having a good biological response[58, 71, 80].

Table 3: Targeted BAG compositions

BAG	wt.% (*mol.%)					
	SiO_2	CaO	P_2O_5	Na_2O	ZnO	SrO
70S	70*	30*				
53S	53	20	4	23		
58S4Zn	58	30	8		4	
58S4Sr	58	30	8			4
Bioglass® 45S5	45	24.5	6	24.5		
Vivoxid (Perioglass)	53	20	4	23		

* BAG 70S is written in mol.% in accordance with other literature. Corresponding wt.% is 71.4 for SiO_2 and 28.6 for CaO.

The polymeric and particulate sol-gel routes are schematically presented in Figure 39. The preparation of the BAG involved the reaction of stoichiometric amounts of tetraethyl orthosilicate (TEOS, $Si(OC_2H_5)_4$, Alfa Aesar), triethyl phosphate (TEP, $OP(OC_2H_5)_3$, Alfa Aesar), calcium nitrate tetrahydrate (CN, $Ca(NO_3)_2 \times 4H_2O$), Alfa Aesar), sodium nitrate (NN, $NaNO_3$, Alfa Aesar), sodium ethoxide (Na-ethoxide, C_2H_5ONa, Alfa Aesar), zinc acetate (Zn-A, $Zn(OOCH_3)_2 \times 2H_2O$, Alfa Aesar) and strontium acetate (Sr-A, $Sr(CH_3COO_2)_2$, Alfa Aesar) according to the desired composition presented Table 3.

In the polymeric sol-gel route the hydrolysis was catalysed by HNO_3. TEOS was dissolved in EtOH and mixed with H_2O and 2M HNO_3 with a molar ratio (H_2O+HNO_3) / TEOS = 8. Other reagents were added in the order presented in Figure 39. On the completion of the hydrolysis the condensation reaction was continued with aging for 24h or it was accelerated by the addition of 2M NH_4OH. The obtained gels were dried at 60 °C for 24h.

Particulate sols were prepared in basic conditions. Alkoxides were mixed together with 50 vol.% ethanol in a ratio previously calculated to obtain the desired glass composition. A mixture of those reagents (M1) was then added dropwise to another mixture of ethanol, water, NH_3OH (M2) where nitrates and acetates were also added. Calcium nitrate was dissolved in an excess of water to avoid $Ca(OH)_2$ precipitation. The H_2O/TEOS molar ratio was 10. The mixture was stirred vigorously during the addition of drops. The pH value of the mixture M2 was carefully kept constant at pH 10.3 with the dropwise addition of NH_4OH to ensure the same conditions for the hydrolysis and condensation for M1 till the end of the process and to avoid possible insoluble calcium hydroxide formation due to the too high pH of the M2. The process was performed with Titrando 835 (Metrohm, Switzerland). After being stirred for 1 h, the obtained white suspension was dried in a dryer at 70 °C overnight or in a microwave oven for 5 min at 120 W, 5 min at 380 W and 5 min at 700 W.

BAG prepared with sodium ethoxide as a precursor for Na_2O was prepared in the same manner, except Na-ethoxide was added dropwise into the M2 mixture and less NH_4OH was used to keep the pH value at 10.3 as the basic conditions were established by ethoxide that is a strong base.

3.2.2.2 Sintering studies

The shrinkages of the BAG pellets during sintering were analysed by a research grade Thermo Mechanical Analyzer TMA Model Q400 V7.4 Build 93 (TA Instruments, USA), that measures the vertical displacement as a function of temperature. Experiments were carried out in the temperature range between 100 to 1000 °C with a heating and cooling rate 10 °C/min under argon flow with a flow rate of 100 ml/min.

Thermogravimetry (TG) and differential scanning calorimetry (DSC) were performed on a DSC Netzsch STA 449 C (Netzsch, Germany) coupled with a mass spectrometer (MS) under a flowing argon atmosphere up to 800 °C with a heating and cooling rate of 10 °C/min.

3.2.2.3 Application of bioactive glass coating on Ti6Al4V

Vacuum infiltration

Ti-alloy samples with porous Ti-layers applied by VPS (samples used for further *in vivo* tests) were coated with bioactive glass by vacuum infiltration. The suspension used for infiltration was 4 wt.% BAG dispersed in ethanol with 0.6 wt.% of deflocculant PEI 1800. The suspension was dispersed with an ultrasonic finger. Ti-alloy samples were placed in a vessel equipped with two valves. One served for evacuation and the other for adding the suspension. The vessel was tightly sealed and the suspension was pumped into the pores of the coatings. After bioactive glass addition a negative pressure was held for another 2 minutes. Coatings were then dried at room temperature and sintered at elevated temperature under vacuum.

Electrophoretic deposition

Samples that were used for the TEM characterization of BAG-coating-Ti-alloy interface were prepared by electrophoretic deposition on flat surfaces due to the easier handling. A Ti6Al4V alloy served as the counter positive electrode and as a negative electrode on which the BAG particles were deposited. Electrodes were placed on 2 cm distance in the BAG suspension prepared in the same manner as for the vacuum infiltration. The deposition was maintained at 15 V for 1 min.

3.3 Characterization

3.3.1 Wettability

The wetting angles of the water on the discs were measured before the hydrothermal treatment, after the hydrothermal treatment, and after the UV irradiation, using a tensiometer (Attension, KSV Instruments).

3.3.2 X-ray diffraction analyses

The crystal structure of the TiO_2 coatings was analysed by X-ray diffractometry (Siemens D5000, Germany) using $Cu_{K\alpha 1}$ radiation (1.5406 Å), with the angle 2θ scanned from 20 to 60° using a step of 0.04° and acquisition time of 1 s (or step 0.034° and holding time 5000 s). BAG crystallization was monitored during sintering by high-temperature X-ray diffractometry PANalytical X'Pert PRO (PANalytical B.V., Netherlands) using $Cu_{K\alpha 1}$ radiation (1.5406 Å, with the angle 2θ scanned from 20–70 °C using a step of 0.04°). Samples were heated 10 °C/min in argon flow and XRD spectra were collected at 25, 500, 600, 700, 800 and 900 °C.

3.3.3 X-ray photoelectron spectroscopy

X-ray photoelectron spectroscopy (XPS, PHI-TFA XPS, Physical Electronics Inc., or ESCA) and Auger electron spectroscopy (AES, PHI 545A scanning Auger microprobe) were used to analyse the surfaces and the at-depth composition of the coatings and to estimate their thicknesses. The at-depth composition of the elements was obtained with XPS/AES depth profiling, i.e., alternating cycles of sputtering with Ar ions and subsequent XPS/AES spectra acquisition. For the AES analysis a static, primary electron beam of 3 keV, with a diameter of ~ 40 μm, was used. The AES depth profiles were obtained by ion sputtering with two symmetrically inclined 1-keV argon-ion beams over area of 5 x 5 mm^2. The sputtering velocity during the AES depth profiling was calibrated on a flat, reference, multilayer structure of Ni/Cr to be 2 nm/min. The XPS-analysed area was 0.4 mm in diameter. The sample surfaces were excited by X-ray radiation from an Al K_α line at an energy of 1486.6 eV. The ion sputtering was performed with 3-keV Ar ions over an area of 3 x 3 mm^2. The sputtering velocity during the XPS depth profiling was calibrated on the flat, reference, multilayer structure of Ni/Cr to be 5 nm/min. The concentrations were calculated from the intensities of the peaks in the XPS/AES spectra using the relative sensitivity factors provided by the instrument manufacturer. The sensitivities of these methods are about 1 at.% and the relative error of the concentrations obtained using the XPS and AES methods are estimated to 20 %.

3.3.4 Photocatalytic activity

The photocatalytic activity of the TiO_2 surface coating was estimated using spin-trapping electron paramagnetic resonance (EPR) spectroscopy (Bruker Elexsys E500; 9.6 GHz). A droplet of a solution containing 0.05 M spin-trap 5-(diethoxyphosphoryl)-5-methyl-1-pyrroline-N-oxide (DEPMPO; $C_9H_{18}NO_4P$; Vinci Biochemicals) in 30 % ethanol (adding KOH to maintain a pH of 11) was placed on the coated discs. The disc was then put under the diode with a wavelength of 365 nm for 5 min. The solution was taken up into a capillary tube and the trapped radical signal monitored for 5 min in the EPR spectrometer. The short-lived reactive oxygen species that will be trapped with the DEPMPO are initially trapped with the primary ethanol trap, which is then converted into the ethyl radical and trapped on the DEPMPO. The absence of hydroxyl or superoxide radicals in the spectra proves that ethanol trapped the primary radical production. The background was measured with respect to the spin-trap solution placed on a non-coated disc and irradiated with UV light under the same conditions.

3.3.5 Leaching of metal ions

The leaching of metal ions was analysed after aging the non-treated and hydrothermally treated discs in a physiological solution (ultrapure 0.9 % NaCl in Milli-Q water) at 36.5 °C for 1 or 6 months. Ultrapure 0.9 % NaCl was used as a blank sample. Prior to the experiments, the aluminium-free polyethylene containers were carefully cleaned with HNO_3 to eliminate any metallic ions that were potentially present. The whole procedure, including cleaning and measurements, was performed in a clean room. The concentrations of titanium, aluminium, and vanadium that leached out of the samples during the 1 month in physiological solution were measured by inductively coupled plasma mass spectroscopy (ICP-MS).

3.3.6 FTIR

Fourier transform infrared (FTIR) measurements were monitored with a FT-IR spectrophotometer (PerkinElmer Spectrum 100 FT-IR) equipped with an ATR (Attenuated Total Reflection) in the mid-IR range 400–1400 or 2000 cm^{-1}.

3.3.7 Particle size distribution

The size of the BAG particles was measured with a laser scattering particle size distribution analyser Horiba LA-920 (Horiba Ltd., Kyoto, Japan). Powders were dispersed in ethanol (without any deflocculant addition) by ultrasound that is a part of the equipment for 5 minutes before measurement.

3.3.8 Electron microscopy

The microstructures of the oxide layer on the hydrothermally treated samples and of the untreated control sample, the BAG powders, sintered BAG pellets and BAG coatings were examined by scanning electron microscopy (SEM JEOL 5800, Tokyo, Japan) and field-emission scanning electron microscopy (FEG-SEM; Zeiss SUPRA 35VP, Carl Zeiss SMT, Oberkochen, Germany and JEOL JSM 7600F, Tokyo, Japan).

For the transmission electron microscopy (TEM) studies the specimens were prepared as cross-sections, where the specimen discs with the oxide surface or BAG coating were placed at the centre of the specimen. After cutting, the specimen was ground and polished into 100-μm-thick discs, which were further prepared according to standard procedures for TEM specimen preparation by dimpling and ion milling (BAL-TEC, RES 010) using 4-kV Ar^+ ions at an incidence angle of 10° to obtain large electron-transparent areas. The morphology and crystallinity of the titania film were studied using a 200-keV transmission electrone microscopes (JEOL 2100 FX and JEOL JEM 2010F, Jeol Inc., Tokyo Japan), and analysed with an energy-dispersive X-ray spectroscopy (EDS).

3.3.9 Mechanical characterization

The adhesion of the coatings to the substrates was evaluated by measuring the shear strengths of the coatings using an Universal Instron Mechanical Testing System (Instron 5569, Instron Co.), according to the ASTM F1044-05 standard. The coated samples and a non-coated Ti6Al4V cylinder were glued together with FM1000 adhesive film (Cytec Ind. Inc., USA), by applying a load during heating. The load was applied in the in-plane direction, with a crosshead speed of 1 mm/min, and the failure loads were determined. Scratch tests and Rockwell indentation tests were also performed to verify the delamination of the coating during the applied load. The scratch test was performed using an automatic scratch tester (Revetest®, SCEM). Load with a normal force 0-100 N was applied with a Rockwell-shaped indenter. The loading rate was 10 N/mm, the transverse velocity of the sample to the diamond was 10 mm/min and the length of the scratches was 10 mm. For Rockwell indentation test the applied load was 60 kg.

3.3.10 Bioactivity testing

The bone-like apatite that formed on the surface TiO_2-coated alloy and BAG samples was observed using an acellular and protein-free simulated body fluid (SBF) as proposed by Kokubo et al.[124]. The pH and ion concentrations were nearly equal to those of human plasma. The cleaned samples were immersed in 30 ml SBF under sterile conditions in sealed flasks and soaked without stirring for up to 3 weeks. The entire specimen was submerged in the SBF. The samples were then rinsed with distilled water and dried in a desiccator. The lower surfaces of the samples (flat pellet surfaces that were facing the bottom of the flask during the immersion) were characterised before and after the soaking using FTIR, SEM and energy-dispersive X-ray spectroscopy.

3.3.11 Bacterial testing

Four different compositions of bioactive glasses prepared by particulate sol-gel technique were tested for their antibacterial properties. Tests were performed with bioactive glass pellets sintered at temperatures evaluated with dilatometric measurements.

Each BAG composition was tested with two different bacteria; S. *aureus* ATCC 25923 and S. *epidermidis* 1457. Three different methods of bacteriological tests were used. Biofilm formation was quantitatively evaluated by viable colony forming unit (CFU) counts after incubation with S. *aureus* ATCC25923 or S. *epidermidis* 1457 and qualitatively by SEM observation of the BAG surface after incubation. Optical density measurements were used to see the effect of leaching ions from BAG on the bacteria.

BAG pellets (Φ = 6 mm, h = 3 mm) were placed in a 24–well plate and covered with 1 ml tryptic soy broth (TSB) inoculated with *S. aureus* or *S. epidermidis* at a starting density 10^4 cells/ml. Plates were statically incubated at 27 °C and then placed on a 3D rotary platform for 24, 48 or 120 hours. After incubation supernatants were removed from the samples and placed in another well-plate. All well plates containing BAG were rinsed with 2 ml of phosphate-buffered saline (PBS). Pellets were then removed from the wells and carefully washed with 3 ml of PBS for 3 times. Rinsed pellets were placed in a plastic tube with 10 ml PBS and sonicated twice for 5 min in a sonication bath (Branson 2510-MT, 42 kHz) followed by 10 s of mixing in a vortex to detach the bacteria from the pellet surface. Next, tenfold serial dilutions in PBS were made from the supernatants and 100 µl were plated on tryptic soy agar (TSA). After overnight incubation at 37 °C, the number of colonies per plate were counted (Figure 7).

Figure 7: Procedure for biofilm formation test. From left to right; Incubation of bacteria with BAG pellets, detaching of bacteria from pellets surfaces, serial dilutions and bacteria colonies on agar plates after overnight incubation.

For the SEM observation the BAG pellets were treated in the same way as described above, but instead detaching from the pellet surface they were fixated by the protocol catheter fixation for SEM. The pellets were immersed in 1 ml glutardehyde (2.5 %) in cacodylate buffer (0.1 M, pH 7.4) for 12 hours at 4 °C, rinsed in 0.1 M cacodylate buffer (pH 7.4) for 1 hour with 3 changes, rinsed with 1 ml distilled water for 1 min, dehydrated in ascending ethanol baths, placed in 1 ml of 100 % hexamethyldisizilane for 5 min and at the end air dried.

The optical density of the supernatants was measured at a wavelength of 600 nm (OD600) with a spectrophotometer Bio-Rad Smartspec 3000 after 24, 48 and 144 hours of incubation of bacteria with BAG samples.

3.3.12 *In vitro* tests

The *in vitro* tests were performed on disc-shaped samples of the Ti6Al4V alloy and on the Ti6Al4V alloy with a porous Ti coating and different surface morphologies. All of the samples were γ-ray sterilised (25 kGy) prior to the tests.

3.3.12.1 Cytotoxicity testing

The first step in the biocompatibility evaluation was to investigate the cytotoxicity of the materials according to ISO 10993-5 in order to exclude any toxic materials. Necrotic cell death due to acute toxicity was assessed according to cell viability over 24 h. The cytotoxicity test was performed using mycoplasma-free Balb/c3T3 cells[2] (ATCC CCL 163) in direct contact. The cells were seeded in 6-well plates (35 mm in diameter, Nunc) at a starting density of 35×10^3 cells/cm^2. Culture medium used was DMEM supplemented with 5 % (v/v) fetal calf serum (Gibco). The cultures were incubated at 37 °C in a humidified atmosphere containing 5 % (v/v) CO_2 for 24 hours. These cultures were examined with an optical microscope in order to verify that the cells consisted of a sub-confluent monolayer and that their morphology was not altered. The culture medium was discarded and fresh medium added to each well. Non-coated and TiO_2-coated titanium samples were carefully placed in the centre of each of the replicate wells, covering one-tenth of the cell layer surface. Negative and positive control materials were treated in the same manner. The wells were then incubated at 37 °C in a humidified atmosphere containing 5 % (v/v) CO_2

---

[2] Balb/c: laboratory-bred strain of the albino mouse

for 24 hours. Positive (BSI disc from Portex Ltd or phenol at 0.64 mg/ml) and negative (Termanox disc or culture medium) controls were run in parallel, and three replicates of each sample and control were used for the analysis.

Cytotoxicity was evaluated by counting the viable cells. At the end of the incubation period (24 h), the culture medium was removed and discarded. The cells were detached using 0.2 % (w/v) trypsin in Hank's balanced solution (Ca^{2+} and Mg^{2+} free) and incubated (2 min) with Trypan blue (Sigma) 0.2 % (w/v) in 0.15 M NaCl. Dead cells (blue) and live cells (uncoloured) were counted using a haemocytometer.

3.3.12.2 Cell coating interaction

Cell adhesion and proliferation were investigated at 1, 3, 9, and 15 days by counting the viable cells. The test system consisted of human osteogenic cells (HOC) from bone marrow, to analyse the cells that are responsible for bone formation and repair, and human endothelial cells (HEC) from microvessels, to analyse the cells that are responsible for angiogenesis, which is required for bone repair.

First, the samples were covered with a complete culture medium and incubated at 37 °C for 30 min. This pre-coating with serum proteins mimics the *in vivo* situation following implantation (for the adsorbed protein layer). The culture medium was then removed and 10×10^3 cells/cm^2 seeded onto the samples. Finally, the complete culture medium was carefully added onto the samples and the plates were incubated at 37 °C in a humidified atmosphere containing 5 % (v/v) CO_2.

3.3.12.3 Cell counting

At the end of the incubation period (1, 3, 9, 15, or 27 days), the culture medium was removed and discarded. The cells were counted as already described for the cytotoxicity evaluation. The negative control was the plastic of the culture wells.

3.3.13 *In vivo* tests

The *in vivo* test was performed on Ti6Al4V alloy cylinders with a porous titanium layer that was non-coated, coated with TiO_2 or coated with BAG. TiO_2 coatings were applied by hydrothermal treatment and BAG was applied by vacuum infiltration. Samples were γ-ray sterilised (25 kGy).

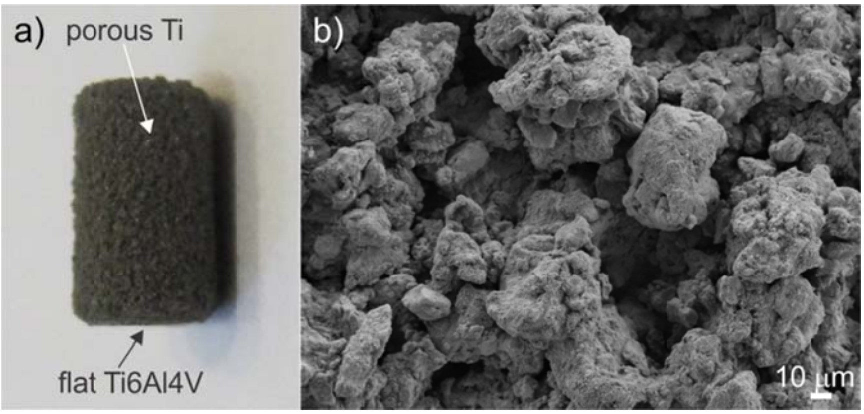

Figure 8: Substrate used for *in vivo* test. (a) Porous titanium-coated cylinder. (b) SEM image of the substrate surface.

3.3.13.1 Surgical procedure

The animal experiments were approved by the Veterinary Administration of the Republic of Slovenia. Fifteen mature male New Zealand rabbits (mean weight 4.5 ± 1.0 kg) underwent the operative procedure. Anaesthesia was induced by intravenous administration of 0.08 mg/kg acetylpromazine (Vanastress; Vana GmbH, Germany), 30 mg/kg ketamine (Narketan, Vetoquinol) and 3 mg/kg xylazine (Chanazine, Chanelle Pharmaceuticals Manufacturing Ltd). Anaesthesia was maintained by intravenous injection of 3 mg/kg propofol (Propofol, Fresenius). After preparation of the surgical field, a skin incision was made over the medial border of the tibia tuberosity, approximately 1 cm distal to the knee joint, followed by dissection of the periosteum and retraction of the tibialis anterior muscle laterally. A tunnel was drilled into the proximal tibial metaphysis at a 90° angle relative to the long axis of the tibia, using a 3.2-mm drill bit. A press-graft was pushed into the tunnel, and the wound was closed in routine fashion. The implant position is shown in Figure 9a. After 10 weeks, the animals were sacrificed by the administration of the above-mentioned sedation, followed by intravenous administration of T61 euthanasia solution (Intervet/Schering-Plough). The samples were harvested by *en-bloc*[3] resection of the proximal tibia, and put into 10 % formaldehyde solution.

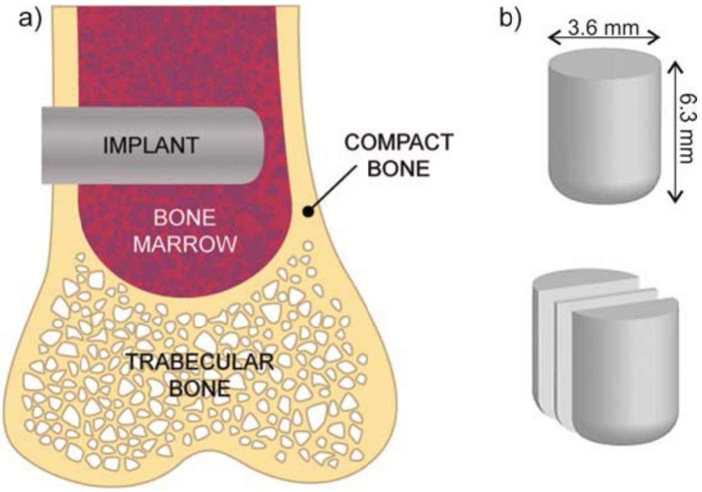

Figure 9: *In vivo* tests. (a) Position of implant in rabbit tibia (b) and implant cutting for histological and morphological examinations.

3.3.13.2 Specimen preparation for *in vivo* tests

The bone implant specimens were removed from the formaldehyde, rinsed with 0.2 M cacodylate buffer, dehydrated through a graded series of ethanol, and embedded in Epon (Epoxy Embedding kit, Sigma-Aldrich, Switzerland). The embedded samples were sectioned vertically along the long axis of the implant (see Figure 9b) using a circular water-cooled diamond saw. One half was ground with SiC papers and polished with diamond paste for scanning electron microscopy (SEM) examination, energy-dispersive X-ray (EDS) analyses, and for quantitative

---

[3] *En bloc* resection: Surgical removal by cutting, as of a tumor or a portion of a structure or organ.

analyses of the bone ingrowth. The second cross-section was used for the further parallel cutting of a thin slice for histological examination (see Figure 9b). The cut slices were then additionally thinned to 50–70 μm by grinding, and then finally stained with Van Gieson picrofuchsin red and Stevenel's blue. Van Gieson red stains the mineralised bone red, and Stevenel's blue stains the osteoid and connective tissue bluish-green. The histological examination was performed on a stereo microscope (Zeiss Discovery.V8, Karl Zeiss AG, Germany).

3.3.13.3 Quantitative analyses of bone ingrowth

The quantitative analysis of the bone ingrowth was performed on polished cross-sections of the explanted samples mounted in Epon resin. Bone ingrowth and bone-to-implant contact were measured on (FEG)-SEM images (JEOL JSM 7600F). EDS mapping was used to distinguish between the mineralised bone, the implant and the polymer resin. For quantification of the volume percentage of bone in the pores, manual stereological analysis was used, with a standard point-count technique[125]. Student *t*-tests were used to analyse the differences between uncoated and coated samples. The relevant area was carefully selected so that only the porous titanium layer was evaluated. The lineal fraction of the bone-to-implant contact was measured using Image Tool software (A Division of Evans Technology, Inc., USA).

4 Results

4.1 Hydrothermal synthesis of TiO_2 coatings

TiO_2 coatings were prepared by hydrothermal (HT) treatment at different conditions, with and without the addition of Ti^{4+} ions and with a different source of Ti^{4+} ions. The surface of the Ti alloy before the HT treatment is presented in Figure 10, which shows the surface morphology before the treatment. The grooves remaining from the machining of the substrates can be clearly seen on the sample surface. The mean surface roughness (Ra) measured with profilometer is 0.21±0.02 µm.

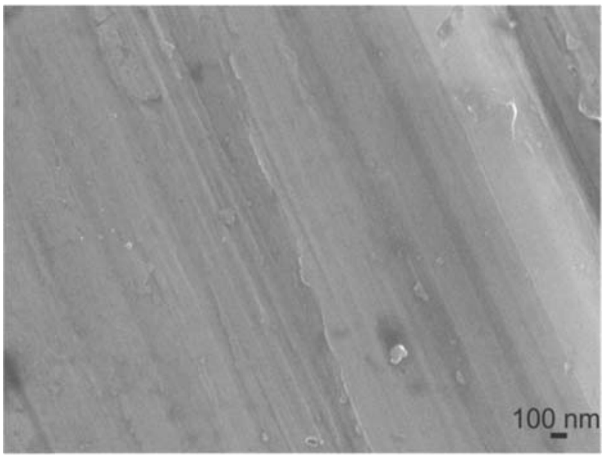

Figure 10: SEM image of the surfaces of the Ti6Al4V alloy samples before HT treatment.

After the HT treatment the formation of a thin layer was reflected macroscopically by a colour change. The samples showed characteristic interference colours, depending on the thickness of the titania layer[126]. The light-grey colour of the untreated substrate changed with increasing thickness through blue, gold or purple and finally to dark grey, for the samples with the thickest oxide layers. The HT treatment strongly affected the surface morphology of the samples: the grooves became less visible because of the oxide coating that formed on the surface.

4.1.1 Hydrothermal treatment without addition of Ti^{4+} ions

In the first set of hydrothermal (HT) experiments (HT A1, A2 and A3) treatments were performed just in water solutions at different pH values, where the pH was adjusted by NH_4NO_3, NaOH or TMAH (Table 4). No additional Ti^{4+} ions were added.

Table 4: Hydrothermal treatments without addition of Ti^{4+} ions.

Hydrothermal treatment	Additives					
	NH_4NO_3 (pH)	NaOH (pH)	TMAH (pH)	t (h)	T (°C)	substrate
HT A1	5			24	200	Ti6Al4V
HT A2		11		24	200	Ti6Al4V
HT A3			11	24	200	Ti6Al4V

Under all conditions we observed the formation of a thin layer of idiomorphic anatase crystals on the surfaces of the HT-treated Ti6Al4V samples. Under acidic conditions (pH=5, adjusted by the addition of NH_4NO_3, HT A1) the crystals had a very distinct anatase morphology (Figure 11a). In addition to bipyramidal {101} faces the crystals had extremely well developed pinacoidal {001} faces (the morphology of the anatase crystals is shown in Figure 11d); however, crystals of an unknown phase were observed as well. The average size of the anatase crystals grown under these conditions was 50−200 nm, whereas the layer thickness rarely exceeded the crystal size (Figure 11a). At an increased pH value (pH=11), adjusted by the addition of NaOH, we observed scattered and randomly oriented anatase crystals with sizes in the range 50−200 nm (Figure 11b, HT A2). The HT-treated samples at an increased pH value (pH=11) with TMAH had a similar morphology and crystal size to the sample treated in NaOH (Figure 11c, HT A3); however, a large fraction of crystals had poorly developed faces. Under all conditions, the coatings were not continuous and their thickness rarely exceeded the crystal size.

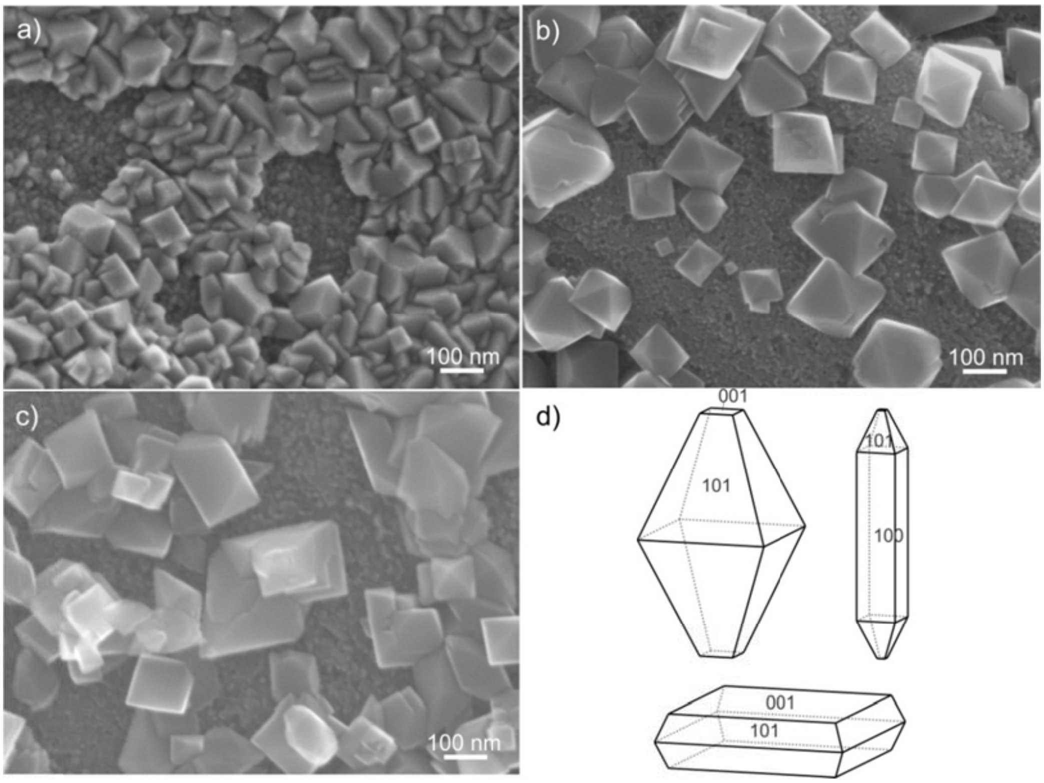

Figure 11: TiO_2 coating prepared with hydrothermal treatments without addition of Ti^{4+} ions. SEM image of the surfaces of the Ti6Al4V alloy samples after hydrothermal treatment with (a) NH_4NO_3 (HT A1); (b) NaOH (HT A2); (c) TMAH (HT A3); (d) Anatase crystal morphology.

4.1.2 Hydrothermal treatment with addition of Ti^{4+} ions

4.1.2.1 Hydrothermal treatment in TiO_2 powder suspension

The great majority of experiments were performed in a suspension of TiO_2 submicron-sized powder (0.5 µm, Fluka AG, CH). Treatment conditions are presented in Table 5.

Table 5: Hydrothermal treatments in suspensions of TiO_2 micro-sized powder.

Hydrothermal treatment	W_{TiO2} (wt.%)	Additives				t (h)	T (°C)
		CA* (wt.%)	AC** (wt.%)	NaOH (pH)	TMAH (pH)		
HT B1	5	/	/	8	/	24	150
HT B2	5	/	/	11	/	48	150
HT B3	5	/	/	8	/	24	200
HT B4	5	/	/	11	/	24	200
HT C1	2.5	/	/	/	11	24	150
HT C2	5	/	/	/	11	24	150
HT C3	30	/	/	/	11	24	150
HT C4	5	/	/	/	11	24	200
HT D1	5	/	/	10	12	24	150
HT D2	5	/	/	8	10	24	200
HT D3	5	/	/	10	12	24	200
HT D4	5	/	/	10	12	72+24***	200
HT E1	5	1	/	10	12	24	200
HT E2****	5	/	0.5	8	10	24	200

*CA: citric acid, **AC: ammonium citrate

*** HT was performed with a longer treatment time (72 h) and also a longer cooling time (24 h)

**** in HT E2 experiments used for bioactivity test Ca^{2+} ions in form of CaF_2 (0.5 wt.% according to TiO_2 powder) were additionally added

The first additions of NaOH alone and TMAH alone were tested at 150 °C and 200 °C. The samples treated in NaOH at 150 °C were coated with crystals resembling anatase morphology (Figure 12a and b; HT B1 and B2) but the coating was not dense. The particles were randomly scattered all over the alloy surface. At 200 °C (Figure 12c, d; HT B3 and B4) the coatings were denser compared to the treatment at lower temperature. They were composed of tightly packed, rounded particles with a few larger and again randomly scattered anatase-shaped particles. At higher pH (pH = 11) the amount of both rounded and bigger particles was greater compared to the treatment at lower pH values (pH = 8).

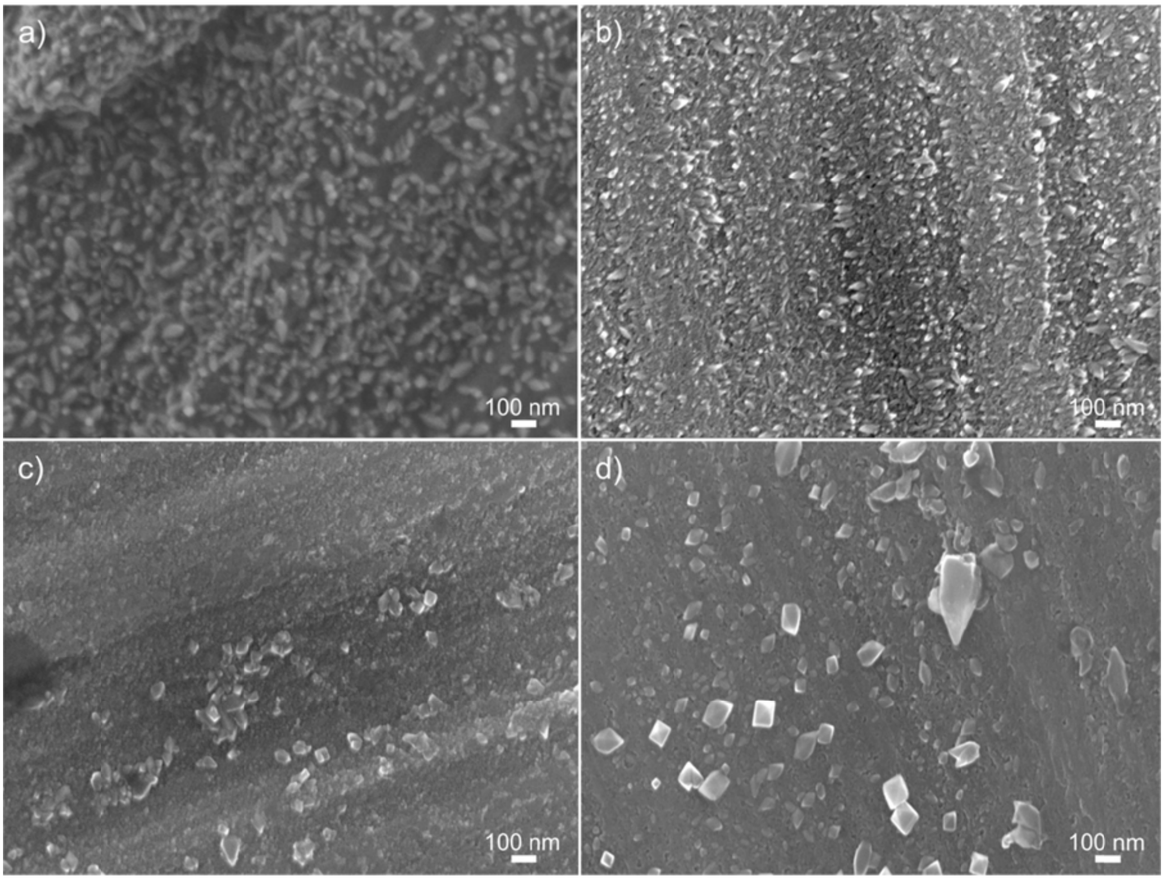

Figure 12: TiO_2 coating prepared with hydrothermal treatments in TiO_2 suspensions with the addition of NaOH. SEM image of the surfaces of the Ti6Al4V alloy samples after hydrothermal treatment with NaOH (a) pH8, 150 °C (HT B1); (b) pH11, 150 °C (HT B2); (c) pH8, 200 °C (HT B3); (d) pH11, 200 °C (HT B4). The concentration of the TiO_2 suspension was 5 wt.%.

For samples treated in TMAH alone at 150 °C three different TiO_2 concentrations were tested: 2.5, 5 and 30 wt.%. The biggest particles were formed with the smallest concentration (Figure 13a, HT C1) and the densest coating with the higher concentration (Figure 13c, HT C3). Crystallites were observed only at the lower concentrations: 2.5 and 5 wt.% (Figure 13a, b; HT C1 and C2). Samples treated in TMAH alone at 200 °C had a surface coated with spherical particles and a few larger particles resembling an anatase morphology, the same as observed for the treatment with NaOH alone at 200 °C. Particles were also bigger than at 150 °C, and the coating was denser (Figure 13d, HT C4).

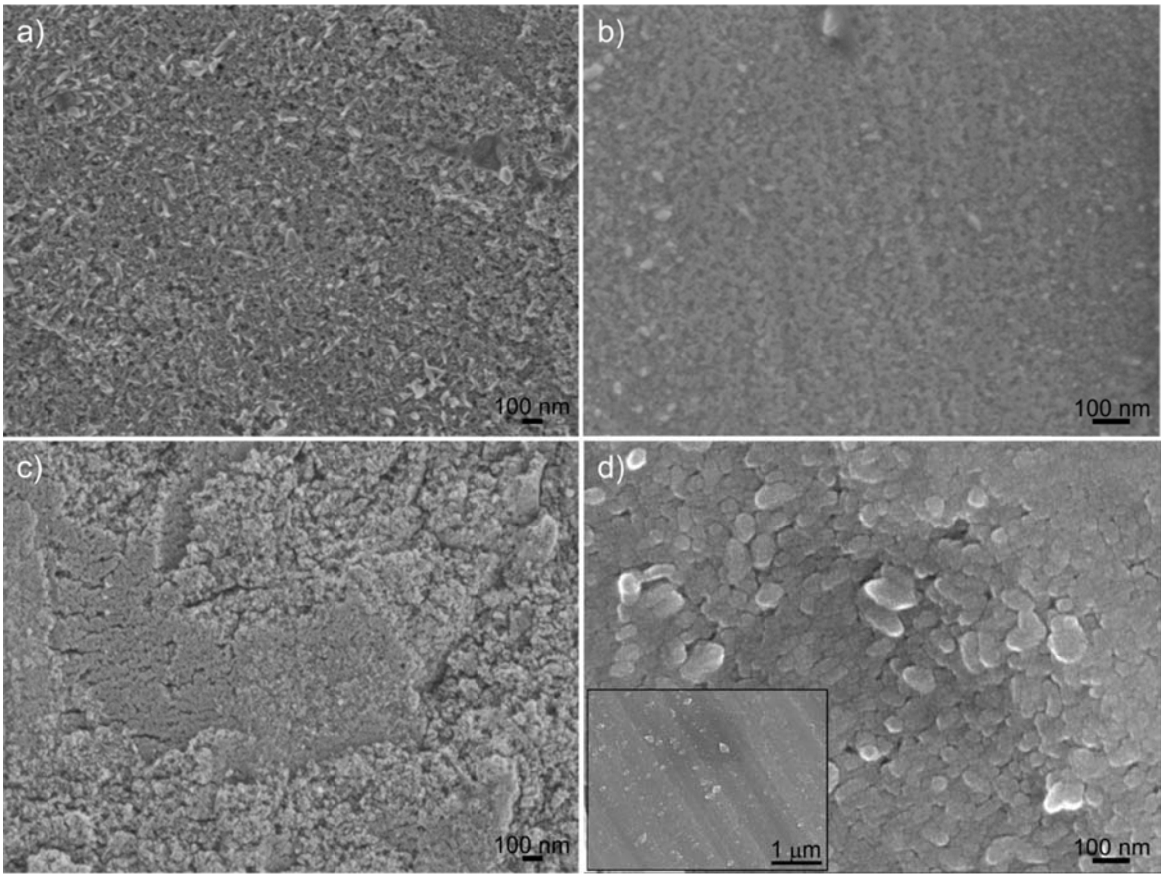

Figure 13: TiO_2 coating prepared with hydrothermal treatments in TiO_2 suspensions with the addition of TMAH. SEM image of the surfaces of the Ti6Al4V alloy samples after hydrothermal treatment with TMAH (a) pH11, 150 °C, w = 2.5 wt.% (HT C1); (b) pH11, 150 °C, w = 5 wt.% (HT C2); (c) pH 11, 150 °C, w = 30 wt.% (HT C3); (d) pH11, 200 °C, w = wt. 5 % (HT C4).

In the third set of experiments with TiO_2 suspensions both NaOH and TMAH were used for hydrothermal treatments (Figure 14). At both temperatures the coatings were dense and composed of TiO_2 crystals, but the particles were sharper at lower temperatures (Figure 14a and b; HT D1 and D2). The particles had an anatase morphology. When the pH was increased the particles became smaller but the coating was dense at both pH values (Figure 14c, HT D3). A longer treatment time was also checked in this set of experiments. The HT D4 samples, presented in Figure 14d, were treated for 72 h and had a slower cooling rate than all the other treatments performed; they were cooled to room temperature in 24 h. The longer time resulted in larger anatase crystals as well as the development of new crystal facets. The crystals are elongated, similar to HT D1, but with developed prismatic {100} faces; they resemble a pencil-like morphology.

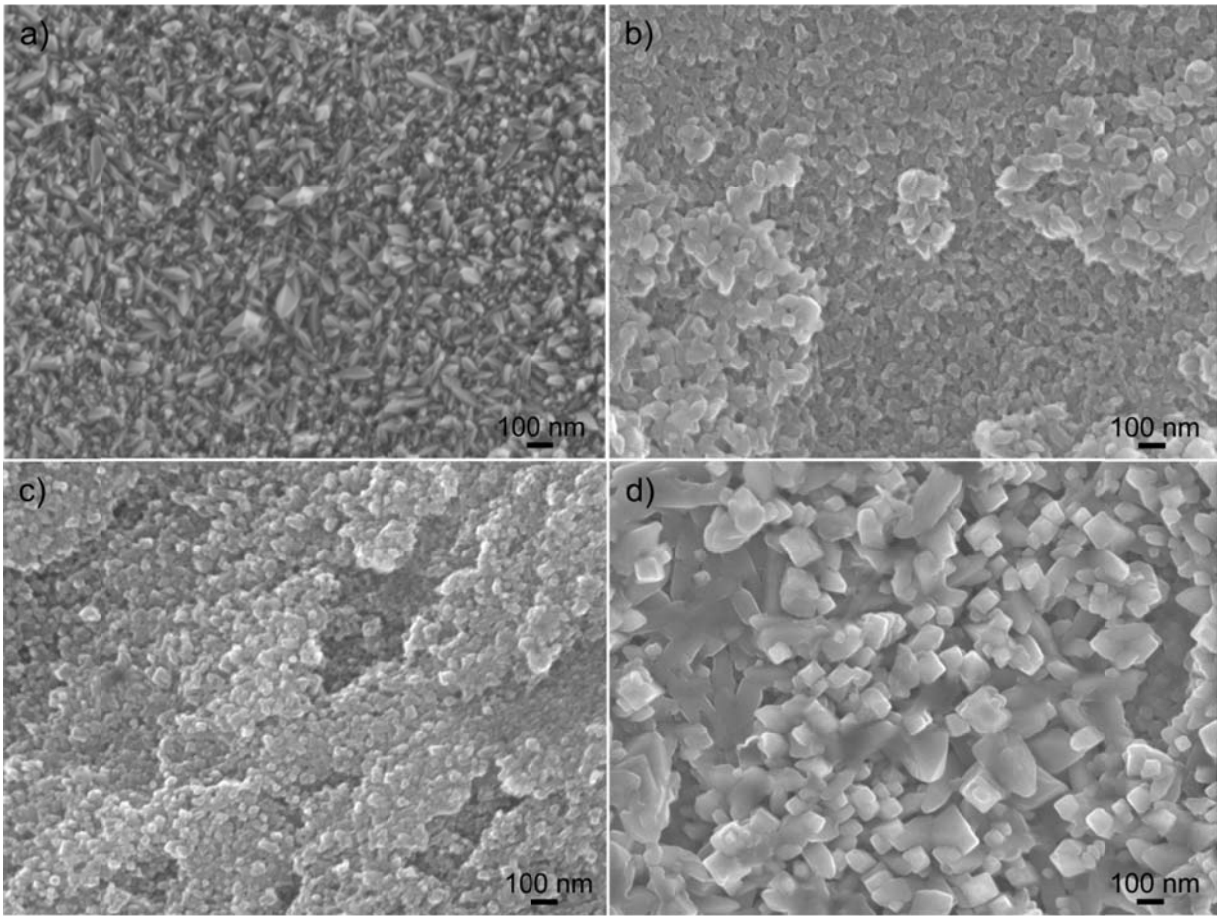

Figure 14: TiO_2 coating prepared with hydrothermal treatments in TiO_2 suspensions with the addition of NaOH and TMAH. SEM image of the surfaces of the Ti6Al4V alloy samples after hydrothermal treatment with NaOH/TMAH (a) pH12, 150 °C (HT D1); (b) pH10, 200 °C (HT D2); (c) pH 12, 200 °C (HT D3) and (d) HT with longer treatment time (72 h) and slower cooling (24 h) pH12, 200 °C (HT D4).

In the final set of experiments citric ions were added to the suspension to obtain the desired pinacoidal morphology of anatase particles with the exposed (001) faces. The citric ions were added in form of citric acid (CA) or ammonium citrate (AC). When the citric acid was added the pH was lowered and therefore the amount of NaOH or TMAH had to be much higher in order to reach the same pH as in the previous experiments. Figure 15a (HT E1) shows the surface of the alloy after the treatment with the addition of citric acid. TiO_2 particles with a characteristic bipyramidal anatase morphology are no more elongated in the <001> direction. Instead, they have well-developed {001} facets. However this dense coating is not homogeneous; large (100–300 nm) anatase particles are mostly found only in the grooves left from the sample cutting. The rest of the surface is still coated with smaller spherical particles with undeveloped anatase facets. When as a source of citric ions ammonium citrate was used, the pH was not lowered and therefore the concentration of NaOH and TMAH remained the same as in previous experiments without citric ions. The surface was again densely coated with TiO_2 particles having an anatase shape and with large {001} facets (Figure 15b, c; HT E2).

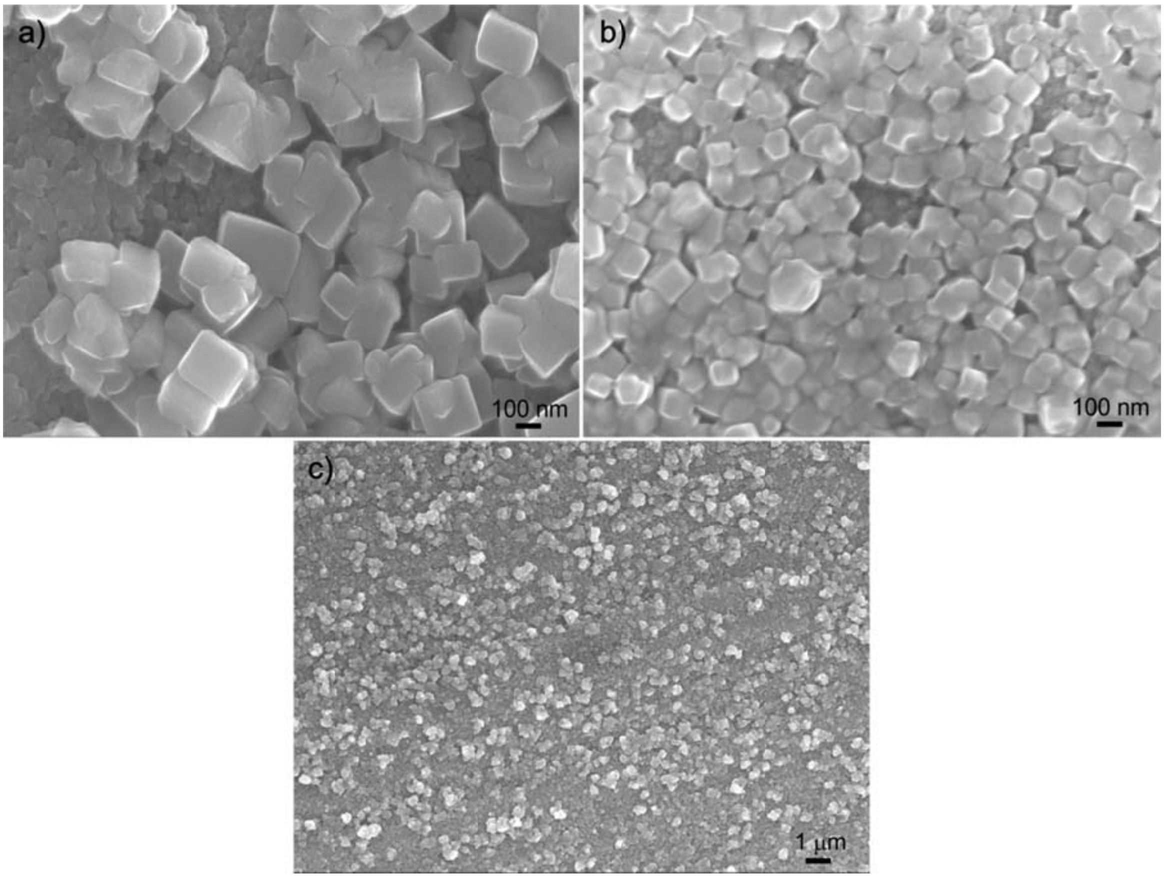

Figure 15: TiO_2 coating prepared with hydrothermal treatments in TiO_2 suspensions with addition of NaOH, TMAH and citrate ion. SEM image of the surfaces of the Ti6Al4V alloy samples after hydrothermal treatment with addition of (a) CA, pH10, 200 °C (HT E1); (b) AC, pH10, 200 °C (HT E2); (c) AC, pH10, 200 °C at lower magnification (HT E2).

4.1.2.2 Hydrothermal treatment in $Ti(OH)_4$ suspension

Instead of using TiO_2 powder a different source of Ti^{4+} ions was used, i.e., $Ti(OH)_4$. The $Ti(OH)_4$ was precipitated from Ti-isopropoxide by hydrolysis. Samples were treated in conditions that were favourable for the pinacoidal anatase shape when using submicron-sized powder. As seen in Figure 16, the surface is completely and densely coated with spherical particles for a treatment with NaOH/TMAH/CA (Figure 16a, HT F1). When AC is used instead of CA, the particles start to resemble the anatase morphology (Figure 16b, HT F2), with developed {101} faces, but with poor {001}. To reduce the size of the {101} and increase the size of the {001} surfaces, more AC was added to the suspension, while the pH was kept the same. Under these conditions the fraction of crystals with the typical anatase shape was reduced. According to morphology, a large fraction of crystals (up to 200 nm long) of an unknown secondary phase (Figure 16c, HT F3) was present in the coating.

Table 6: Hydrothermal treatments with $Ti(OH)_4$ as source of Ti^{4+} ions.

Hydrothermal treatment	Additives				t (h)	T (°C)
	CA (pH)	w(AC) (%)	NaOH (pH)	TMAH (pH)		
HT F1	3	/	4	10	24	200
HT F2	/	0.5	8	10	24	200
HT F3	/	1	8	10	24	200

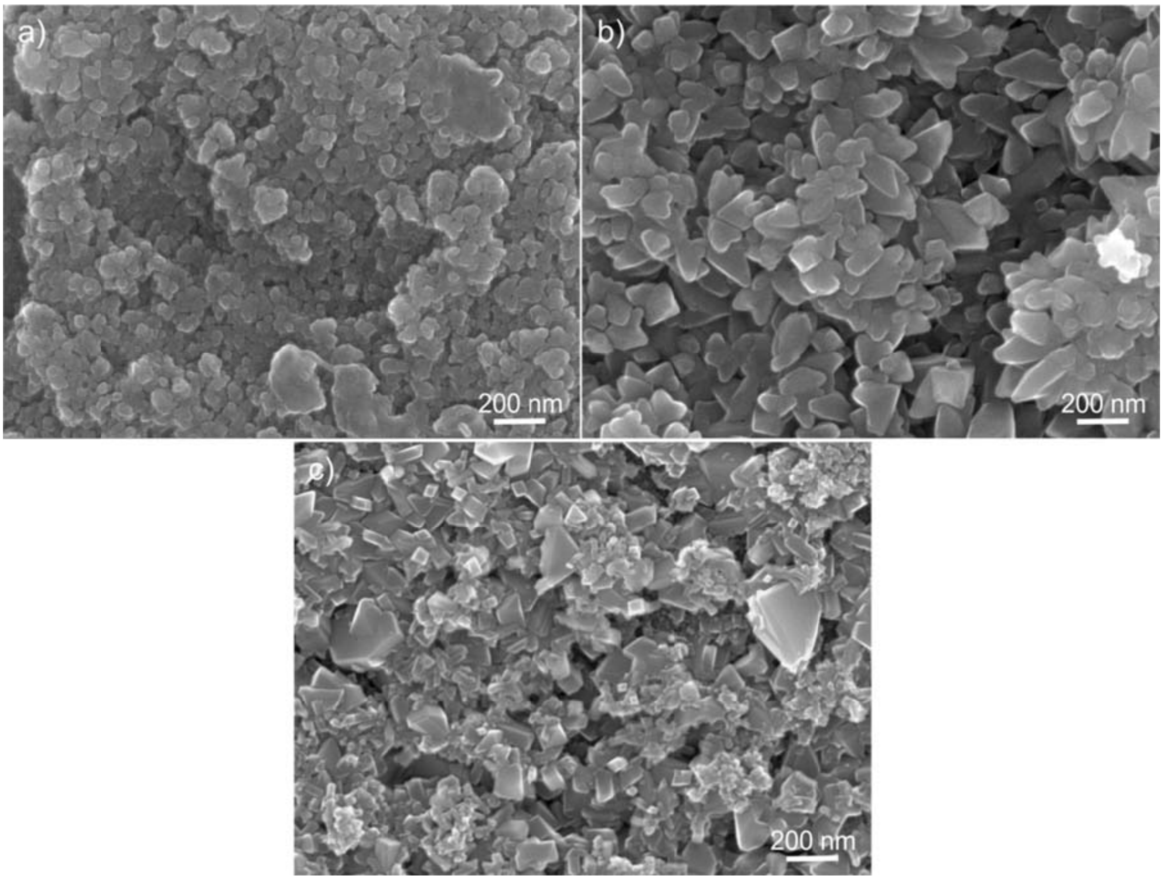

Figure 16: TiO_2 coating prepared from $Ti(OH)_4$. SEM image of the surfaces of the Ti6Al4V alloy samples after hydrothermal treatment with (a) NaOH, TMAH (HT F1); (b) NaOH, TMAH, CA (HT F2); (c) NaOH, TMAH, AC (HT F3).

In subsequent experiments, instead of the flat, disc-shaped Ti6Al4V alloy samples, substrates with more complex surfaces were hydrothermally treated according to the above procedures to obtain a TiO_2 coating with pinacoidally shaped crystals (HT E2). The dental implant (Figure 17a, c) and porous Ti-layer on the Ti6Al4V alloy (Figure 17 b, d) were fully covered with a dense layer of anatase crystals. This result confirmed that a hydrothermal treatment is a convenient method for obtaining a uniform TiO_2 coating of various complex shapes: smooth, rough, or even porous surfaces.

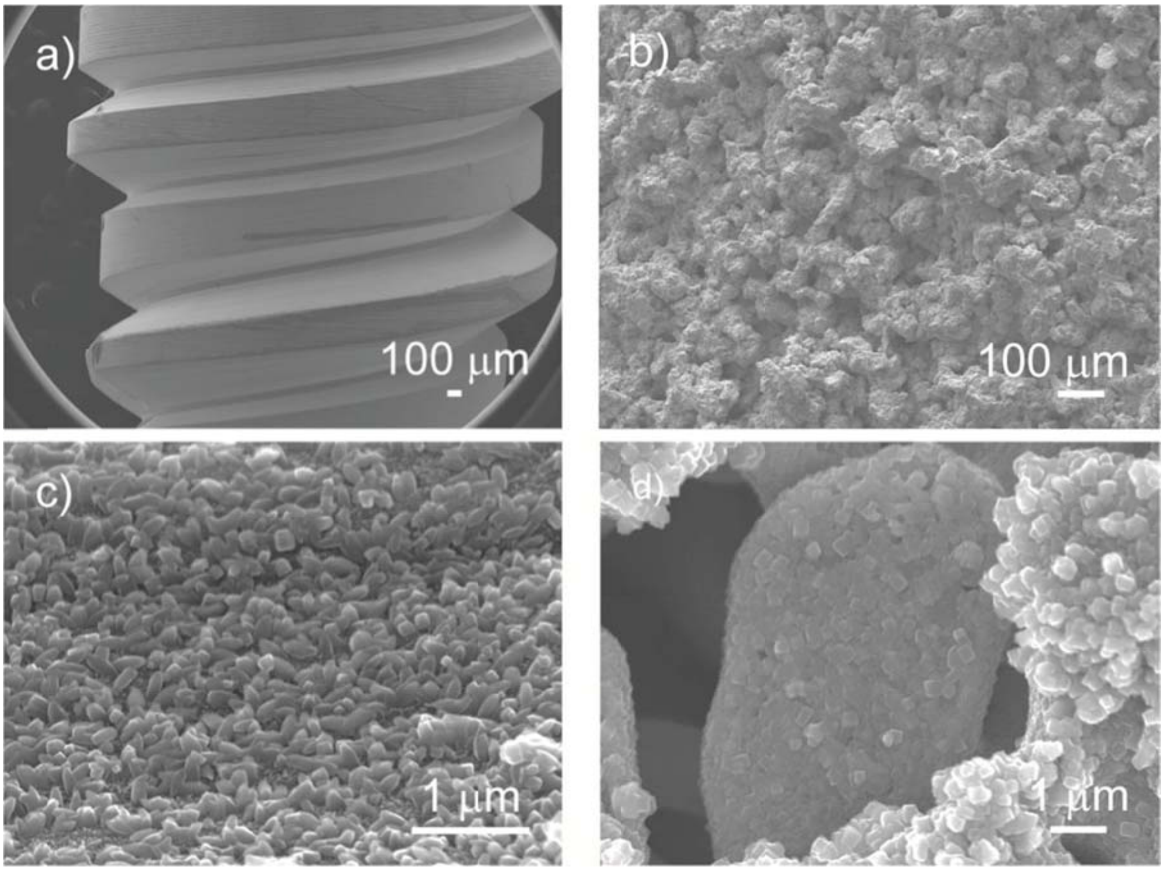

Figure 17: TiO_2 coatings on complex samples following the hydrothermal treatment of (a, c) a dental screw (HT D2) and (b, d) a porous titanium-coated Ti6Al4V cylinder (HT E2).

4.1.3 Characteristics of TiO_2 coating

4.1.3.1 XPS study of HT-treated samples

The compositions of the surface and oxide layers were analysed by X-ray photoelectron spectroscopy (XPS) and Auger electron spectroscopy (AES).

Figure 18 shows the AES and XPS depth profiles obtained from the untreated sample (Figure 18a), from the HT-treated sample without the addition of Ti^{4+} ions (Figure 18b), from the HT-treated sample in the $Ti(OH)_4$ suspension (Figure 18c) and from the HT-treated sample in the TiO_2 suspension (Figure 18d). The treated samples differ from the untreated ones in terms of the thickness and the composition of the oxide layers. As is evident from Figure 18a, for the untreated sample the oxygen concentration drops from 31 to 6 at.% after just 5 min of sputtering, whereas it decreases much more slowly when the sample has a HT-formed oxide layer on its surface. The oxide-layer thickness was calculated from the sputtering time and the sputtering velocity. Assuming that the thickness is given by the depth when the oxygen concentration drops to half of its initial value, the estimated thickness of the native oxide layer on the untreated sample is less than 10 nm. It should be pointed out that the alloying elements Al and V, which have possible toxic effects, were detected on the surface of the untreated sample (Figure 18a). When samples were HT treated without Ti^{4+} (HT treated in a NH_4NO_3 solution) ions the oxide layer became thicker (approximately 180 nm), which is also the size of the anatase crystal (seen in Figure 11). The concentrations of undesired Al and V ions on the surface were also lower (Figure 18b).

A depth profile of the sample treated in the $Ti(OH)_4$ suspension revealed an oxide with a continuous transition of the Ti and O concentrations (Figure 18c). This can be ascribed either to the presence of non-stoichiometric Ti sub-oxides at the layer/substrate interface or to the effect of the non-uniform sputtering of the rough surface (the nano roughness of the sample's surface is 35 nm). The first explanation is supported by the presence of Ti^{3+} and Ti^{2+} peaks in the XPS spectra as well as by the strong adhesion of the oxide layer to the Ti6Al4V substrate. The thickness of this layer was approximately 200 nm.

The depth profile of the sample treated in the TiO_2 suspension (Figure 18d) confirmed that it had a much thicker oxide layer, as was also observed with the SEM and TEM analyses (estimated to be 600 nm, Figure 22). It was confirmed that for those samples the Ti/O ratio is still constant, even after 90 min of sputtering (~ 180 nm), meaning that the at-depth analyses were stopped in the oxide layer. In addition, the Ca^{2+} is evidently incorporated into the coating's structure. Ca^{2+} was added to improve the bioactivity.

Table 7: Atomic concentration of elements on the surface and 30 nm below the surface for Ti6l4V substrate and HT treated samples.

	at.% conc. of elements on the surface				
sample	Ti	Al	V	O	C
Ti6Al4V	8.5±1.7	4.7±0.9	1±0.2	31.4±6.2	54.4±10.9
HT in NaOH solution	23.6±4.7	0	0	60.3±12.1	16.1±3.2
HT in $Ti(OH)_4$ suspension	23.8±4.8	0	$0.2\pm0.4*10^{-1}$	56.8±11.4	19.3±3.9
HT in TiO_2 suspension	5.8±1.2	0	0.8±0.2	22.6±4.5	70.8±14.2
	at.% conc. 30 nm below the surface				
sample	Ti	Al	V	O	C
Ti6Al4V	74.5±14.9	7.5±1.5	3.3±0.7	6.5±1.3	8.2±0.3
HT in NaOH solution	38.0±7.6	0	$0.1\pm0.2*10^{-1}$	61.5±12.3	0.4±0.1
HT in $Ti(OH)_4$ suspension	43.7±8.7	0	$1.0\pm0.2*10^{-1}$	54.7±10.9	0.6±0.1
HT in TiO_2 suspension	30.6±6.1	0	0.9±0.2	51.8±10.4	16.7±3.3

It is important to note that for the samples HT treated in TiO_2 or $Ti(OH)_4$ suspensions no Al was found in the Ti-oxide layers. The elemental compositions of all the samples obtained with the XPS and AES analyses on the surface and at a depth of about 30 nm below the surface (obtained after the corresponding sputtering time) are given in Table 7. The main difference in the surface compositions between the samples is the presence of metal ions. It should be mentioned that a part of the oxygen and carbon detected at the surface is a consequence of molecules being adsorbed from the air. Vanadium was not detected in the surface layer of the other samples treated without an additional source of Ti^{4+} ions. As already observed with the EDS analysis of the sample treated in a TiO_2 suspension, a small amount of V was still present on the surface of the samples treated with an additional source of Ti^{4+} (Table 7), which is the influence of the solid solubility of V in TiO_2. However, the concentration of undesired Al and V ions is strongly reduced.

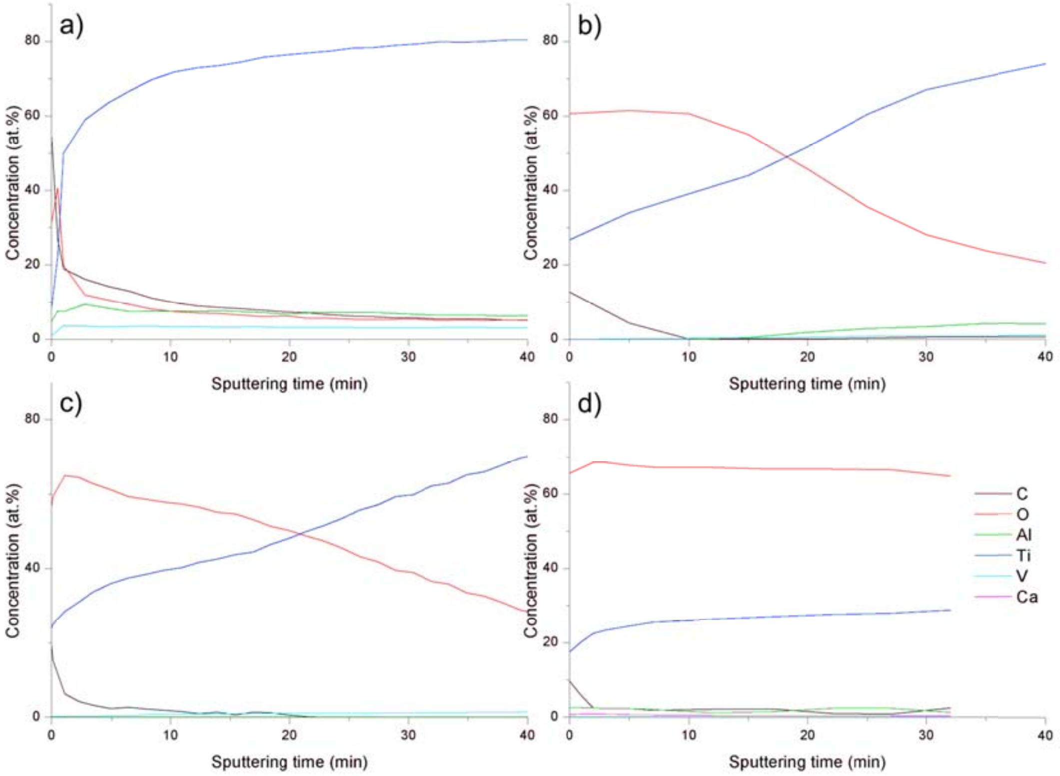

Figure 18: AES and XPS depth profiles obtained on the surface of: (a) untreated Ti6Al4V, (b) HT treated without addition of Ti^{4+} ions, (c) HT treated with addition of Ti^{4+} in the form of $Ti(OH)_4$ and (d) HT treated with addition of Ti^{4+} ions in the form of TiO_2 powder. Sputtering velocity for AES was 2 nm/min (a) and for XPS was 5 nm/min (b, c, d).

The Ti 2p spectrum from the surfaces of all the samples showed that characteristic binding Ti 2p peaks appeared at binding energies of 458.8 and 464.3 (shown in Figure 19a). These binding energies are characteristic for TiO_2 and confirm that the surface is mainly composed of TiO_2. The O 1s spectrum from the surface also has two characteristic binding peaks (Figure 19b). The peak at the binding energy 530.1 eV corresponds to oxygen atoms bonded in TiO_2. The peak at 532.3 eV is characteristic for Ti-OH or for adsorbed water molecules on the surface.

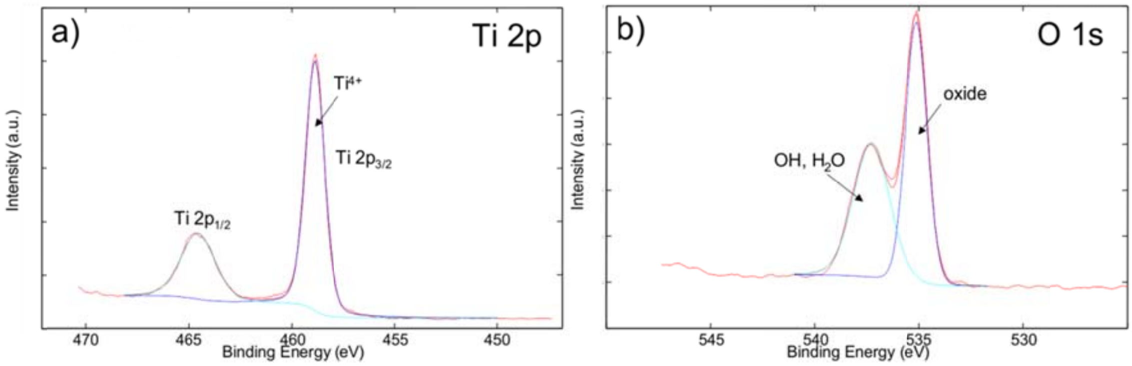

Figure 19: XPS spectrum obtained on the surface of the sample with TiO_2 coating (HT D2); (a) of Ti 2p (b) of O 1s

4.1.3.2 TiO_2 phase detection of HT-treated samples

The structure of the oxide surface layer on the hydrothermally treated samples was analysed using XRD. The spectra of untreated and treated samples are shown in Figure 20. The peaks at 38.6°, 39.6°, 53.4°, 35.4°, 40.5° 2θ belong to the substrate (Figure 20a). The XRD study confirmed the anatase structure of an oxide layer on all treated samples that had enough thick coating to be detected by conventional XRD. The small anatase peak at 2Θ of 25.3° which corresponds to the (101) plane of anatase was already observed in spectra of the sample treated without the addition of Ti^{4+} ions, but only in TMAH solution (HT A3). Due to the thin and inhomogeneous coating the intensity of the peak is small (Figure 20b).

The coating formed in acidic conditions seems to be even thinner, as no anatase peaks were detected; therefore, the anatase phase had to be confirmed by Raman spectroscopy.

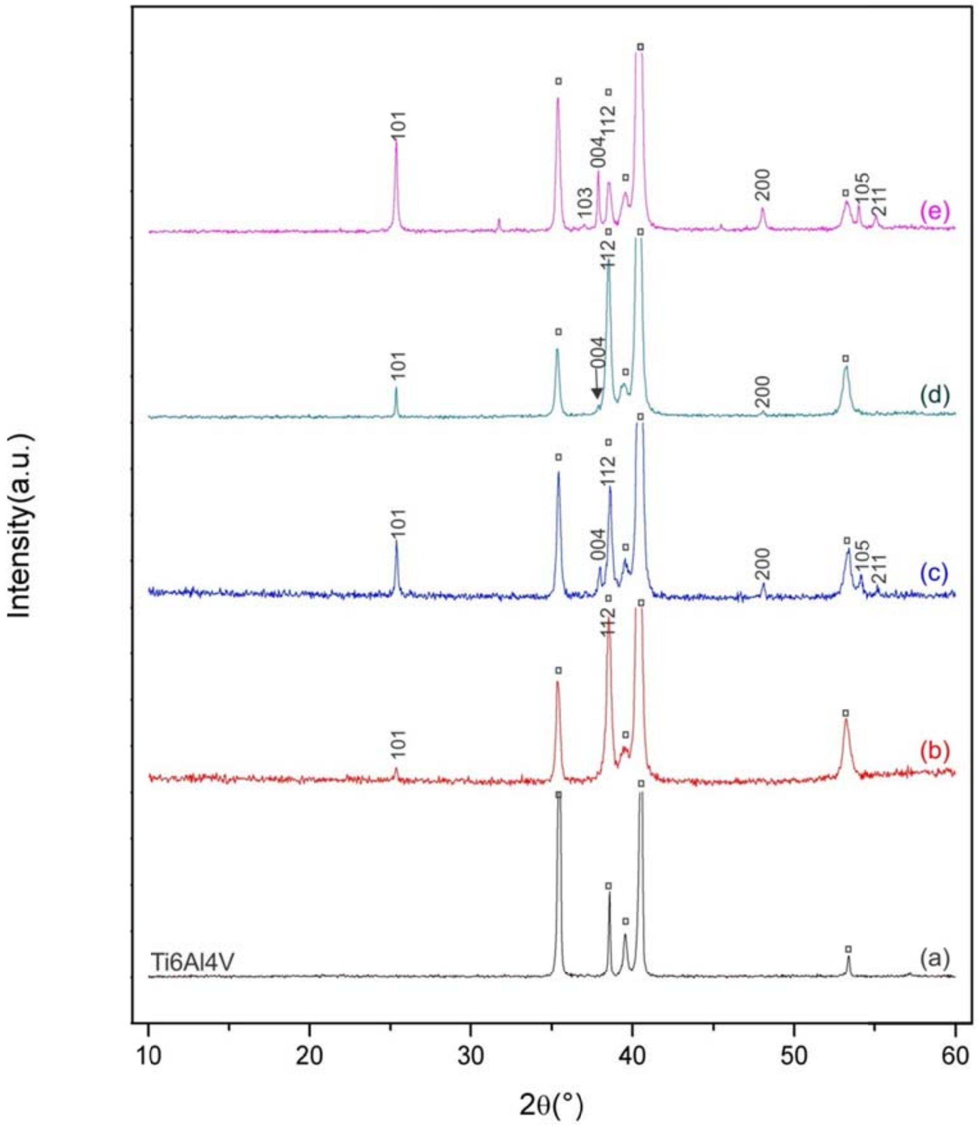

Figure 20: XRD spectra of non-coated and TiO_2 coated Ti6Al4V; (a) non-coated Ti6Al4V; (b) HT treatment without addition of Ti^{4+} (HT A3); (c) HT treatment in TiO_2 suspension with addition NaOH/TMAH (HT D2); (d) HT treatment in TiO_2 suspension with addition of NaOH/TMAH/AC (HT E2); (e) HT treatment in $Ti(OH)_4$ suspension (HT F2).

When treatments were performed in hydrothermal conditions containing an external source of Ti^{4+} ions (HT D2, E2 and F2), the peaks became higher and more peaks were visible; the peaks corresponding to (101), (004), (200) as well as, (103), (105) and (211) anatase planes were visible. Coatings formed in the TiO_2 suspension with TMAH or NaOH alone could not be determined by XRD even at prolonged holding times. No peaks were observed on either of the coatings, showing their amorphous state (HT B3). A few crystals that were scattered on the sample surface after treatment in the TiO_2 suspension with the addition of NaOH were not enough thick to be determined by XRD, but were confirmed to be anatase by Raman spectroscopy (see Figure 21b).

The samples treated in the TiO_2 suspension with the TMAH/NaOH/AC addition (Figure 20c, d) were much denser and the coating was much thicker, therefore anatase peaks were much more visible compared to HT A3. Both spectra had a peak at 2Θ of 25.3° that belongs to the (101) plane and 2Θ of 39.6° that belongs to the (004) plane.

XRD spectra also confirmed the anatase structure for the coating prepared with HT in the $Ti(OH)_4$ suspension (Figure 20e). Due to the thick oxide layer this spectra had the highest anatase peaks and besides the peak corresponding to the (101) planes, a high peak corresponding to (001) is visible, as well as (100), (103), (105) and (211). An additional peak is observed at around 32°, which could belong to a brookite phase[127] or possibly to some Ti sub-oxide.

For anatase TiO_2 six characteristic Raman modes could be detected at 144, 197, 399, 513, 519, and 639 cm^{-1} [128]. Raman spectra, provided for samples with too thin TiO_2 coatings to be detected with XRD, are shown in Figure 21. Both spectra indicate the presence of anatase.

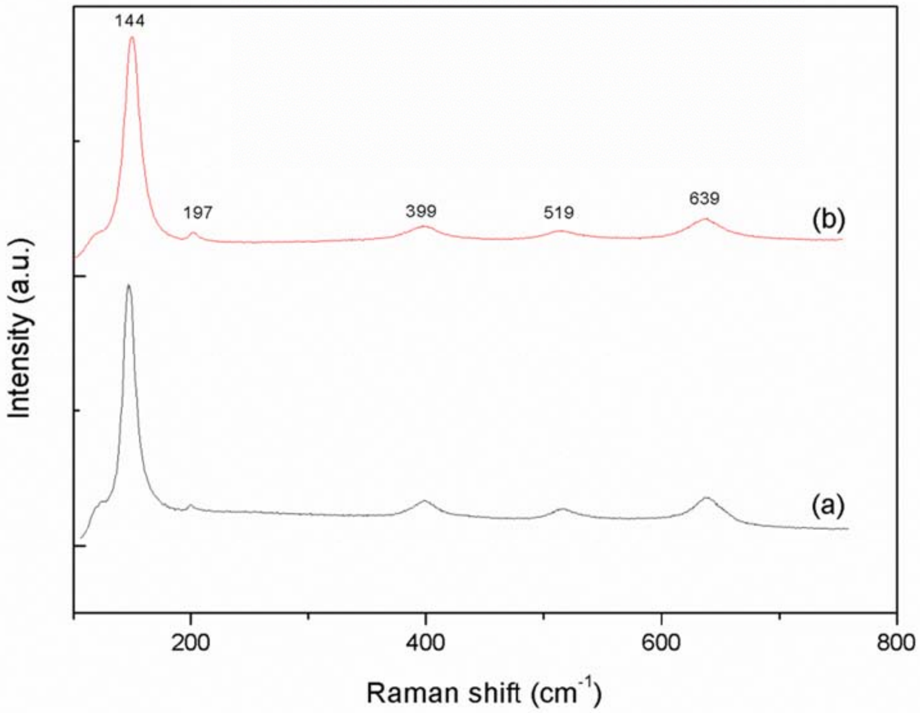

Figure 21: Raman spectra of TiO_2 coated samples; (a) treatment in NH_4NO_3 solution (HT A1); (b) treatment in TiO_2 suspension with addition of NaOH (HT B3).

4.1.3.3 TEM/SEM study of HT-treated Ti6Al4V samples

The TEM was used to examine the contact between the Ti6Al4V substrate and the titania layer, the crystallinity and crystallography of the titania particles, and finally their chemical composition. We analysed the sample HT treated in a TiO_2 suspension according to the procedure HT E2 with the thickest oxide layer. The thickness of the TiO_2 coating, which was estimated by XPS to be more than 180 nm, was measured from the SEM cross-section image to be around 600 nm (Figure 22). Figure 23a presents a TEM cross-section of the TiO_2 layer (upper part) on the Ti6Al4V substrate (lower part).

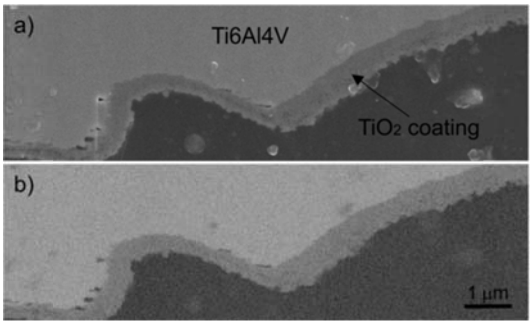

Figure 22: Cross section images of TiO_2 coated Ti6Al4V. (a) secondary electron SEM image, (b) backscattered electron image.

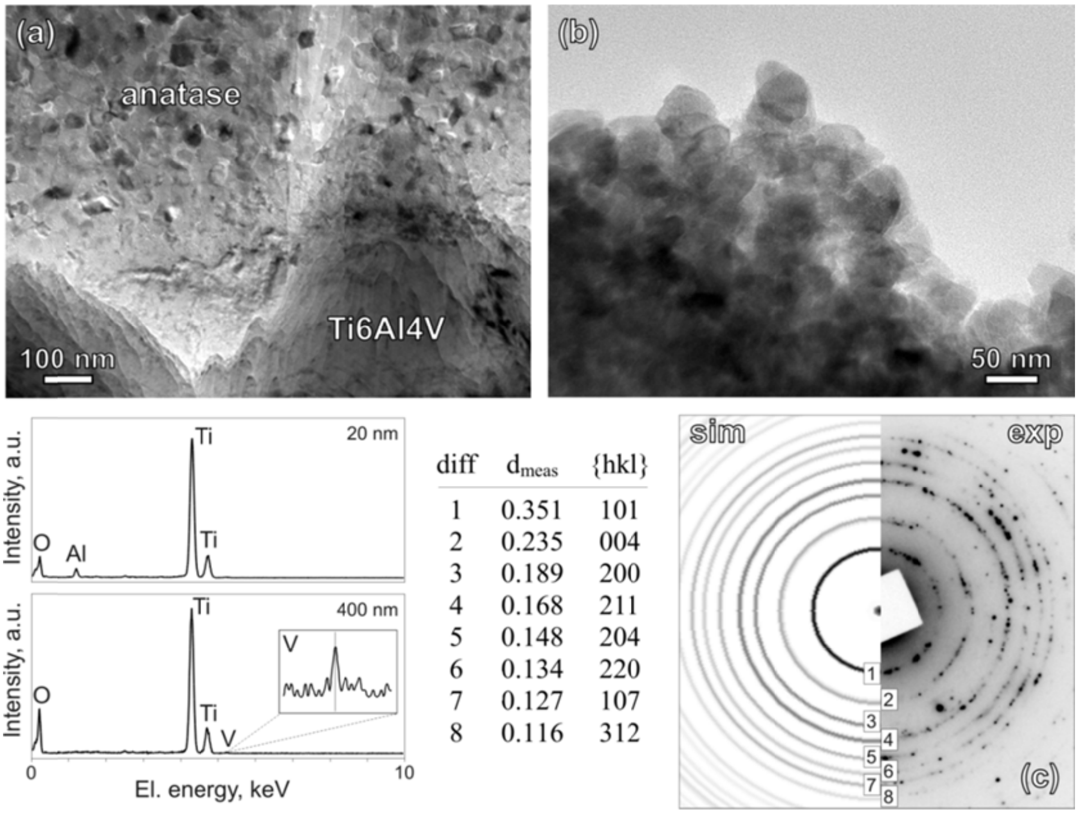

diff	d_{meas}	{hkl}
1	0.351	101
2	0.235	004
3	0.189	200
4	0.168	211
5	0.148	204
6	0.134	220
7	0.127	107
8	0.116	312

Figure 23: TEM images of HT treated Ti6Al4V specimen with TiO_2 addition (HT E2) in cross-section: (a) The interface between the substrate and titania layer. (b) The surface of the oxide layer. (c) Experimental and calculated SAED patterns with measured d-values for anatase. EDS spectra of the oxide layer (bottom left) at 20 and 400 nm distance from the interface.

No visible cracks or pores were present along the substrate/oxide interface, suggesting a strong bonding between the alloy and the titania layer. The oxide layer was composed of nanocrystalline titania particles. Close to the interface the titania crystals are smaller and denser, whereas towards the surface their size increases. The developed crystals that grew in the cavities displayed a distinct morphology that is common for anatase (Figure 23b). The EDS analysis of the anatase crystals close to the interface showed a considerable amount of Al (up to 1.7 at.% at 20 nm), dropping rapidly with the distance from the alloy (below the detection limit at 400 nm). Quantitative EDS analyses showed a small amount of V throughout this layer. In the inset of Figure 23, showing the EDS spectrum of the titania layer at 400 nm, the low intensity V-K_{β} (5.426 keV) line is enlarged, while the V-K_{α} keV line partly overlaps with the Ti-K_{β} line (4.931 keV). The presence of vanadium can be attributed to the equilibrium solid solubility of V in the anatase structure[129]. The selected-area electron diffraction (SAED) patterns recorded from the nanocrystalline oxide layer showed diffraction rings with d-values that correspond to anatase (Figure 23c). All the diffraction rings in the SAED patterns could be matched to the lattice planes of anatase.

4.1.3.4 Adhesion

Next, we verified the strength of the adhesion. Using a scratch test we estimated the titania layer to be well attached to the alloy's surface (Figure 24a, b), as the layer next to the scratch did not peel off the substrate and no cracks were observed. The scratch critical load (L_c) could not be evaluated as the detachment of the coating was not observed, even at the highest applied load of 60 N.

Strong adhesion of the TiO_2 layer to the substrate is of utmost importance for coatings on implant surfaces. With the aim to verify the strength of the adhesion, we employed various techniques: scratch test, Rockwell indentation and a shear-strength test. The scratch test should provide the critical load at which the coating starts to delaminate; however, in our case, delamination did not appear and therefore the failure of the titania coating could not be determined. As is evident from Figure 24a and b, the scratch initially formed in the anatase coating extended with increased load into the substrate without visible signs of delamination. Also, the Rockwell indentation did not reveal cracks that typically appear by delamination (Figure 24c).

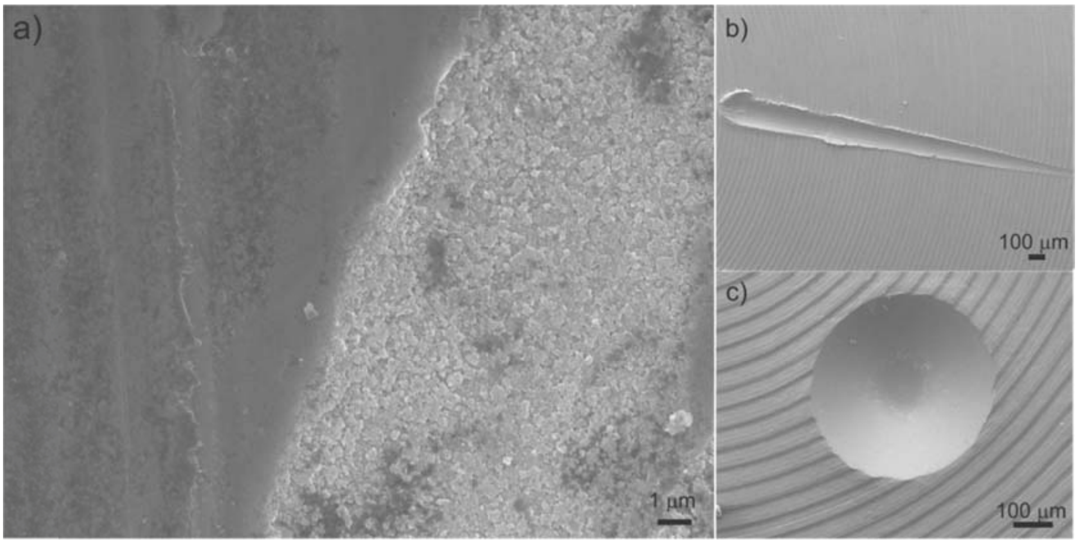

Figure 24: Scratch test on the TiO_2 coated sample; (a) scratch-coating interface, (b) scratch at lower magnification. (c) Rockwell indentation test.

Using a shear-strength test we confirmed that the TiO_2 coatings were firmly attached to the Ti6Al4V substrate (the mean value for Ti6Al4V discs was >45 MPa). Any failures occurred within the glue, confirming that adhesion of the coating is greater than actually detected. The failure in the glue can be seen in Figure 25. Both the coating on Ti6Al4V and on the porous Ti reached higher values (Table 8) than required for biomedical coatings, which is more than 22 MPa.

Table 8: Adhesion strength of TiO_2 coating on Ti6Al4V and TiO_2 coating on porous Ti sample

Sample	Average adhesion (MPa)
TiO_2 coated Ti6Al4V	43.7±4.8
TiO_2 coated porous Ti	32.7±6.7

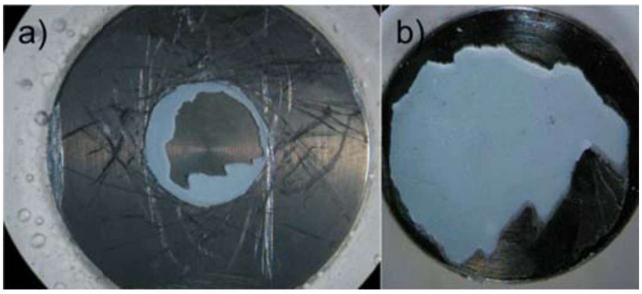

Figure 25: Failure of the glue after adhesion test of TiO_2 coated sample (HT D2); (a) sample side and (b) and the non-coated counterpart.

4.1.3.5 Leaching of metal ions

The leaching of metal ions during soaking at 36.5° in physiological solution (0.9 % NaCl) was measured after one month and, for the non-treated sample, also after 6 months of soaking. The amount of metal ions was reduced for all the TiO_2 coated samples. The amount of Ti and Al was under the limit of detection. Only a small amount of V was detected in all the coated samples. Much higher concentrations were measured for non-coated samples. The results are presented in Table 9.

Table 9: Titanium (Ti), aluminium (Al) and vanadium (V) ions released from non-coated and coated discs after one or six month of immersion in physiological solution.

Sample	Time (month)	ng/cm^2		
		Ti	Al	V
Ti6Al4V, non-treated	1	1.64±0.02	42.00±0.42	2.57±0.03
Ti6Al4V, non-treated	6	1.98±0.02	27.97±0.28	4.12±0.04
TiO_2 coated (HT E1)	1	0*	0*	0.03±0.03*10^{-2}
TiO_2 coated (HT D2)	1	0*	0*	0.11±0.01*10^{-1}
TiO_2 coated (HT C4)	1	0*	0*	0.004±0.004*10^{-2}

*under the limit value that is calculated according to the control sample

4.1.3.6 Photocatalytic activity

The non-coated and TiO_2-coated Ti6Al4V alloy samples were irradiated for 4 h under UV light (wavelength >290 nm) and then immersed into resazurin dye solution to qualitatively estimate the photocatalytic activity. After UV-irradiation, the violet resazurin dye solution was discoloured by the TiO_2-coated samples, appearing pink within 24 h, but this colour change was not seen with the non-coated sample. As suggested in previous studies, this colour change indicates the formation of radicals that induce the decomposition of organic substances [130]. The effect was quantitatively analysed using the EPR signal in an ethanol droplet (30 % EtOH/KOH) that remained on the discs during 5-min of UV irradiation (365 nm) for the ethanol-spin trap mixture. The data confirmed significant radical production, which is the consequence of the excited TiO_2-coated sample (Figure 26). For a comparison, Degussa P25 TiO_2 powder, which is known to have good photocatalytic properties, was evaluated in a similar way; the powder and spin trap were admixed in ethanol and UV-irradiated for 5 min. The EPR signal of the TiO_2 coating was increased 10-fold and the signal for the TiO_2 P25 22-fold compared to the blank.

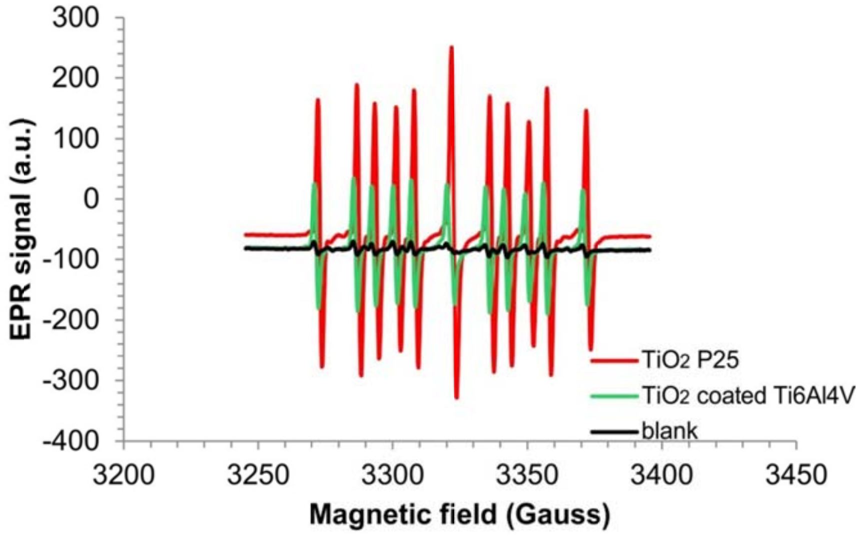

Figure 26: EPR signal for a TiO_2-coated sample and Degussa P25 TiO_2 powder compared to KOH (blank).

4.1.3.7 Wetting

After the hydrothermal treatment the wetting angle of the titanium alloys decreased. As presented in Table 10 the wetting angle decreased from 91° for non-treated Ti6Al4V down to 30° for a sample that was fully coated with pinacoidally shaped anatase. Almost no change was observed for coatings with nanosized and amorphous particles (89 and 87°), while amorphous coatings with at least a few anatase crystals were less hydrophobic, i.e., the wetting angle was 78°. The most hydrophilic were crystalline anatase TiO_2 coatings.

Table 10: Wetting angles for non-treated and TiO_2 coated samples with different morphologies

Sample	Coating description	Average wetting angle (°)
Ti6Al4V, non-treated	/	91
TiO_2 coated (HT in $Ti(OH)_4$ + NaOH/TMAH/CA)	amorphous	87
TiO_2 coated (HT in TiO_2 + NaOH)	few crystals	78
TiO_2 coated (HT in TiO_2 + NaOH/TMAH/CA)	crystalline	48
TiO_2 coated (HT in $Ti(OH)_4$ + NaOH/TMAH/AC)	crystalline	43
TiO_2 coated (HT in TiO_2 + NaOH/TMAH/AC)	crystalline	37

An additional decrease in wetting angle was measured after UV irradiation of the discs for 4h. It can be seen in Figure 27a-c how the wetting angle on the Ti6Al4V alloy decreases after hydrothermal treatment to 55° and after the UV irradiation it drops to 9°. The change from the hydrophobic to a hydrophilic surface can be ascribed to the photocatalytic decomposition of the organic impurities on the disc surface. The effect is particularly pronounced in the case of the porous Ti-coating on the Ti6Al4V alloy, with which the original high wetting angle on the titanium of nearly 120° dropped drastically after the hydrothermal treatment, as reflected in a sudden penetration of the water droplet into the pores (Figure 27d, e).

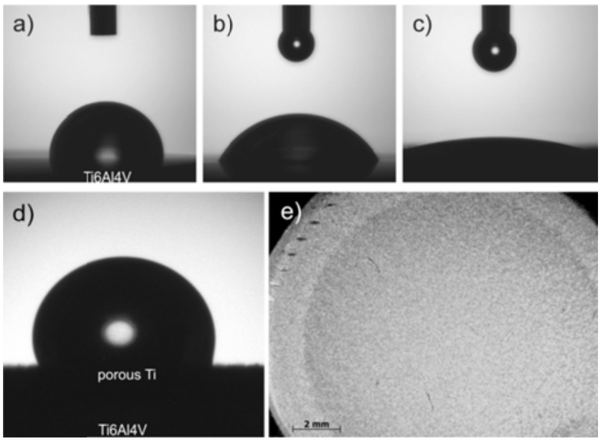

Figure 27: Wetting angles on Ti6Al4V disk; (a) before and (b) after the hydrothermal treatment and (c) after HT treatment and UV irradiation. Wetting angles on porous Ti coated Ti6Al4V; (d) before and (e) after hydrothermal treatment-top view; the dark grey circle represents the liquid penetrated into the pores.

4.1.4 Bioactivity testing of TiO_2 coatings in acellular SBF

The bioactivity was tested on TiO_2-coated as well as on non-coated discs. Non-coated discs did not exhibit any ability to form hydroxyapatite (HA) in simulated body fluid (SBF), even after a prolonged soaking time (5 weeks). Though the non-treated Ti6Al4V sample retained its surface morphology while soaking for 3 weeks in SBF, apatite formation was observed on some hydrothermally treated samples (Figure 29). The Ca/P ratio was confirmed by EDS to be 1.67±0.01, which is the stoichiometric ratio of hydroxyapatite. Moreover, bioactivity was observed only for the TiO_2 coatings with specific morphologies. In our experiments, amorphous TiO_2 coatings or coatings with round-shaped crystals (anatase crystals with no sharp edges) never induced apatite formation (Figure 28). Differences in the bioactivities were also seen across the different crystalline coatings. No hydroxyapatite nucleation was observed on the surfaces with bipyramidal anatase morphology, elongated in the <001> directions, i.e., for crystals with no or very small {001} facets and, consequently, very large {101} facets; however, slight bioactivity (Figure 29a) was observed for elongated crystals with large {100} facets and, consequently, smaller {101} facets. On the other hand, very good bioactivities (Figure 29b, c) were seen for coatings with anatase crystals expressing {001} facets (pinacoidal anatase, Figure 29e, f). In addition, smaller crystals resulted in better bioactivity; although the samples were soaked in SBF for the same duration, the surface of the sample with larger pinacoidal crystals (Figure 29e) was only partly covered with apatite (Figure 29b), whereas the sample with smaller crystals (Figure 29f) was fully covered with apatite (Figure 29c).

The thickest and the most dense hydroxyapatite layer apparently formed on the TiO_2 coating with pinacoidal anatase crystals and the addition of Ca^{2+} ions (Figure 29d). The bioactivity expressed by apatite formation on this surface can be ascribed to the presence of the Ca^{2+}, as seen in the XPS spectra of the coating (see Figure 19d).

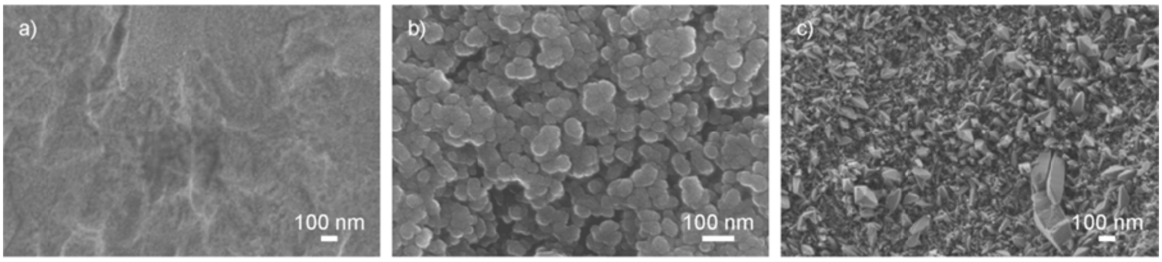

Figure 28: Bioactivity test. SEM images of TiO_2 coatings that were soaked in SBF but induced no HAp formation. (a) amorphous TiO_2 coating prepared by the HT C3 procedure but using nano-sized TiO_2 powder, (b) HT F1, (c) HT D1.

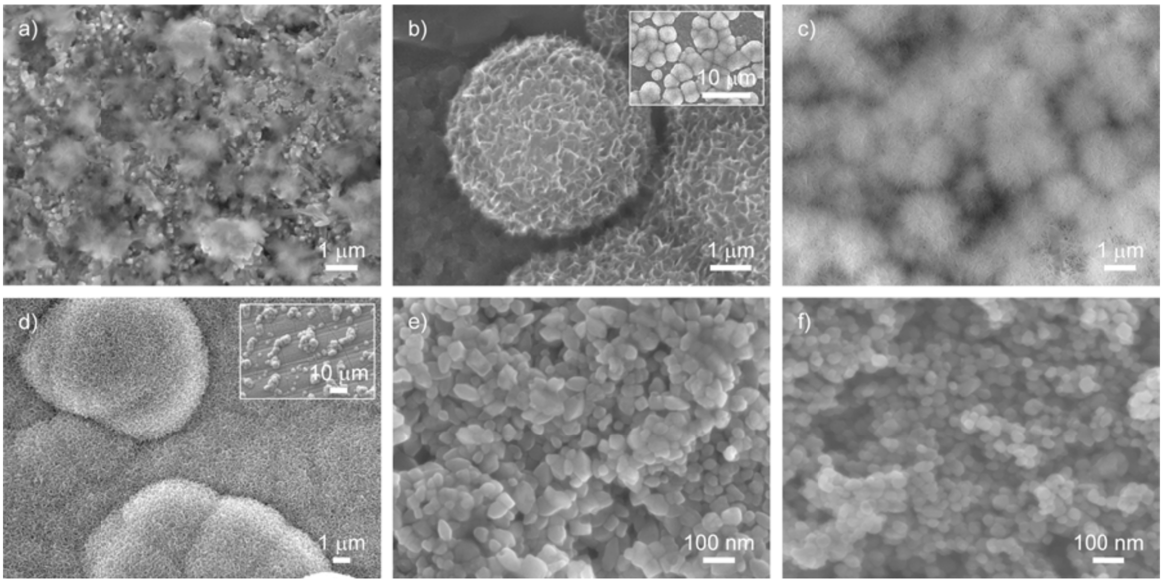

Figure 29: Bioactivity test. SEM of anatase-coated Ti-alloy surfaces before and after soaking in SBF for 3 weeks. (a) Sample with bipyramidal anatase crystals with large (100) facets (surface before soaking is shown in Figure 14d); (b) sample with larger pinacoidal crystals after soaking; (c) sample with smaller pinacoidal crystals after soaking; (d) sample with larger pinacoidal anatase crystals and addition of Ca^{2+} ions; (e) surface from b before soaking; and (f) surface from c before soaking.

4.1.5 *In vitro* characterisation of the cell–coating interaction

To determine the effects of the surface characteristics of the material for implants, *in vitro* tests were performed on two types of TiO_2 coatings with different grain morphologies of the anatase TiO_2 crystals: (a) bipyramidal, elongated in the <001> directions (sample 2, HT D1)); and (b) with small pinacoidal crystals (sample 3, sample 5, HT E2), and on two different substrates: (a) Ti6Al4V and (b) Ti6Al4V with a porous titanium coating. The morphologies of these samples are illustrated in Figure 14a and Figure 14c, respectively.

The as-received Ti6Al4V alloy with (sample 4) and without the porous titanium layer (sample 1) were also tested for comparison.

Table 11: Composition of the analysed samples.

Sample	Substrate	TiO_2 coating
1	Ti6Al4V	-
2	Ti6Al4V	bipyramidal anatase crystals (HT D1)
3	Ti6Al4V	pinacoidal anatase crystals (HT E2)
4	Ti6Al4V with porous titanium coating	-
5	Ti6Al4V with porous titanium coating	pinacoidal anatase crystals (HT E2)

4.1.5.1 Cytotoxicity tests on Balb/c cells

No cytotoxic effects were observed for the hydrothermally treated Ti6Al4V alloy (samples 2 and 3). With the Balb/c 3T3 cell the viabilities were expressed as percentages of the negative control, i.e., 102 % for sample 2, and 115 % for sample 3 (Figure 12). The results obtained for the pure Ti6Al4V alloy (without the TiO_2 coating; sample 1) were similar, at 103 %. For the Ti6Al4V alloy with the porous titanium layer, the percentage of viable cells was 88 % (sample 4), while it was 91 % for the TiO_2-coated Ti6Al4V with the porous titanium (sample 5). Indeed, no significant inhibition of the cell growth was observed for any of the test materials considered and the cell morphology was not altered.

Table 12: Balb/c 3T3 cell viabilities following direct contact with the samples.

Sample Number*	Cell viability (% negative control)
1	103
2	102
3	115
4	88
5	91

* see Table 11 for details

4.1.5.2 Cell–coating interaction

To compare the TiO_2-coated samples and the non-coated samples, the results were normalized to the negative controls, i.e. the plastic material of the wells. As illustrated in Figure 30, the adhesion and proliferation of human osteogenic cells (HOC) after day 1 was better for the samples coated with TiO_2, either with bipyramidal (sample 3) or pinacoidal anatase (sample 4) particles, compared to non-coated samples (sample 1). Over time, the cell spreading and proliferation decreased for both coated and non-coated samples. For TiO_2-coated sample 2 (bipyrmidal TiO_2 crystals), after 24 h (D1) adhesion was high for both cell types. Although the morphology observed in terms of the adherence of HOC was very good (data not shown), after 3 days (D3) 90 % of the cells were detached. This negative effect was even greater for the human endothelial cells (HEC), none of which were attached to the sample by day 3. Due to detachment and negative proliferation, the test was stopped at day 3.

On the other hand, for TiO_2-coated sample 3 (pinacoidal TiO_2 crystals), good HOC adhesion and spreading were observed. The cell density after day 1 was higher than that of the non-coated sample. Up to day 3 the HOC continued to proliferate well, with the density remaining greater than that of the non-coated sample. However, the HOC started to detach after day 3, which was particularly obvious by day 9, when the cell density decreased by more than 50 % to values lower than that of the non-coated sample. At this stage, HEC adhesion and spreading appeared to be better than that of the HOC. Thus, the HEC slowly proliferated, resulting in a cell density greater than that of the non-coated sample by day 9, which is an interesting result when taking into account the sensitivity of the HEC.

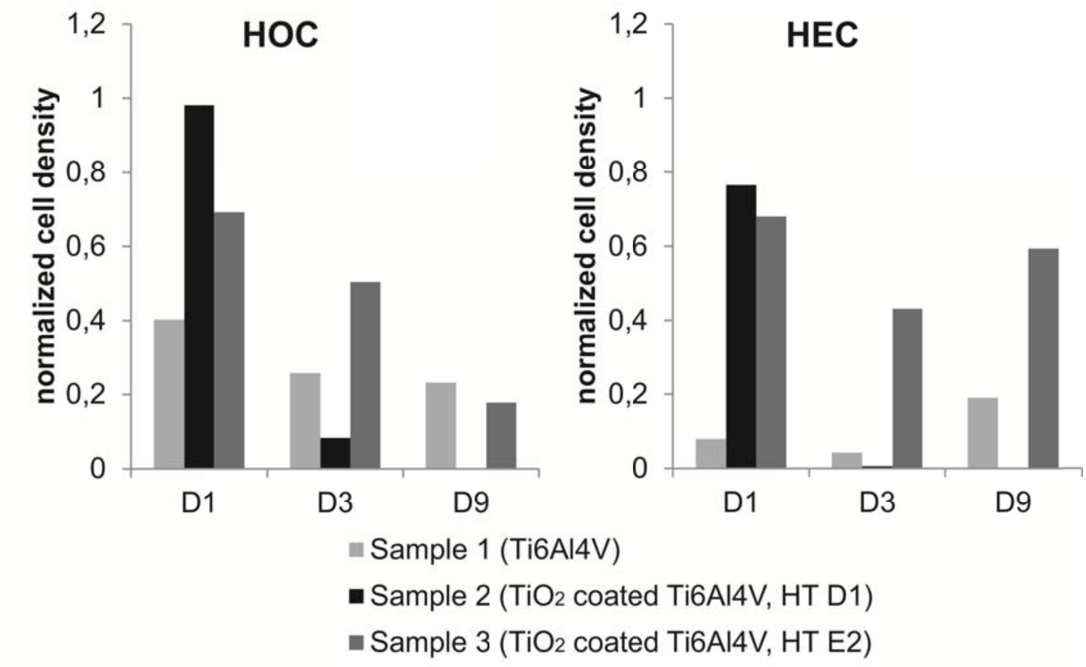

Figure 30: Adhesion and proliferation of human osteoblast cells and human osteogenic cells on the Ti6Al4V alloy. HOC and HEC adhesion and proliferation on the (a) non-coated (sample 1) and (b) TiO_2-coated Ti6Al4V alloy samples with different anatase morphologies (samples 2 and 3, respectively).

Figure 31 shows the proliferation of the samples on non-coated and TiO_2-coated Ti6Al4V alloy with a porous Ti layer. Both samples 4 and 5 (non-coated Ti layer and TiO_2-coated Ti layer) exhibited very poor adhesion after day 1 for both HOC and HEC, and no significant cell proliferation thereafter. However, the HOC continued to proliferate on the substrate very slowly until day 15 (Figure 31b). No significant HEC adhesion and growth was observed (Figure 31b).

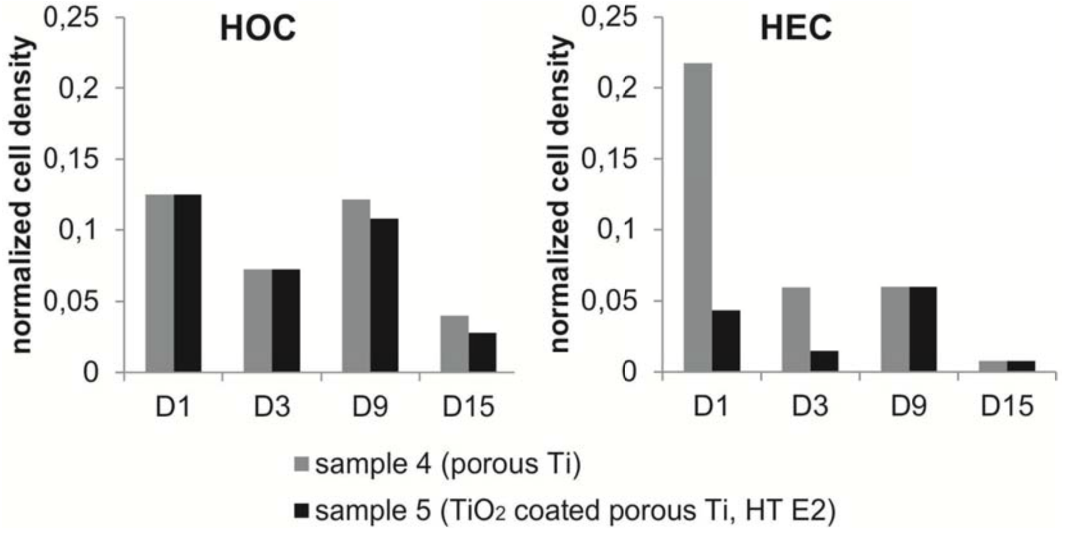

Figure 31: Proliferation of human osteoblast cells and human osteogenic cells on the porous titanium-coated Ti6Al4V alloy. (a) Sample 4, untreated porous titanium, showing adhesion of the HOC and HEC. (b) Sample 5, TiO_2-coated porous titanium, showing adhesion of the HOC and HEC.

4.1.6 *In vivo* test

The *in vivo* tests were performed using Ti6Al4V alloy cylinders (Figure 8) with a porous titanium layer that was either non-coated (6 implants) or hydrothermally (HT E2) coated with TiO_2 (8 implants). The samples were extracted from the rabbit tibia after 10 weeks of implantation and examined in two ways: a) stained histological preparations of the perpendicular cross-sections of the implants and adjacent newly formed bone (~300-µm-thick slices) were examined with optical microscopy, and b) polished bulk cross-sections were analysed by SEM and EDS.

These *in vivo* tests showed the beneficial effects of the hydrothermal treatment. In both kinds of samples (non-coated and TiO_2 coated), no fibrous tissue encapsulated the implant 10 weeks after implantation (Figure 32). Newly formed mineralised bone (NB) was in direct contact with the implant surface and had grown into the porous coating. This new bone had an organised structure, with Haversian canals and several lacunae and osteocytes. The spaces between the trabeculae were filled with adipose tissue, which contained many fat and blood cells (Figure 32b, d). The new bone growth was directed towards and along the implant surface (Figure 32a). No differences in bone morphology were seen between the non-coated (Figure 32a, b) and coated (Figure 32c, d) implants, except for the greater amount of mineralised bone within the pores in the TiO_2-coated sample. However, the evaluation of the occupation of the pores by bone using transmitted light is not reliable because a large fraction of the pores are not visible due to the particular thickness of the opaque metallic slices (the pore opening depends on the thickness of the slice).

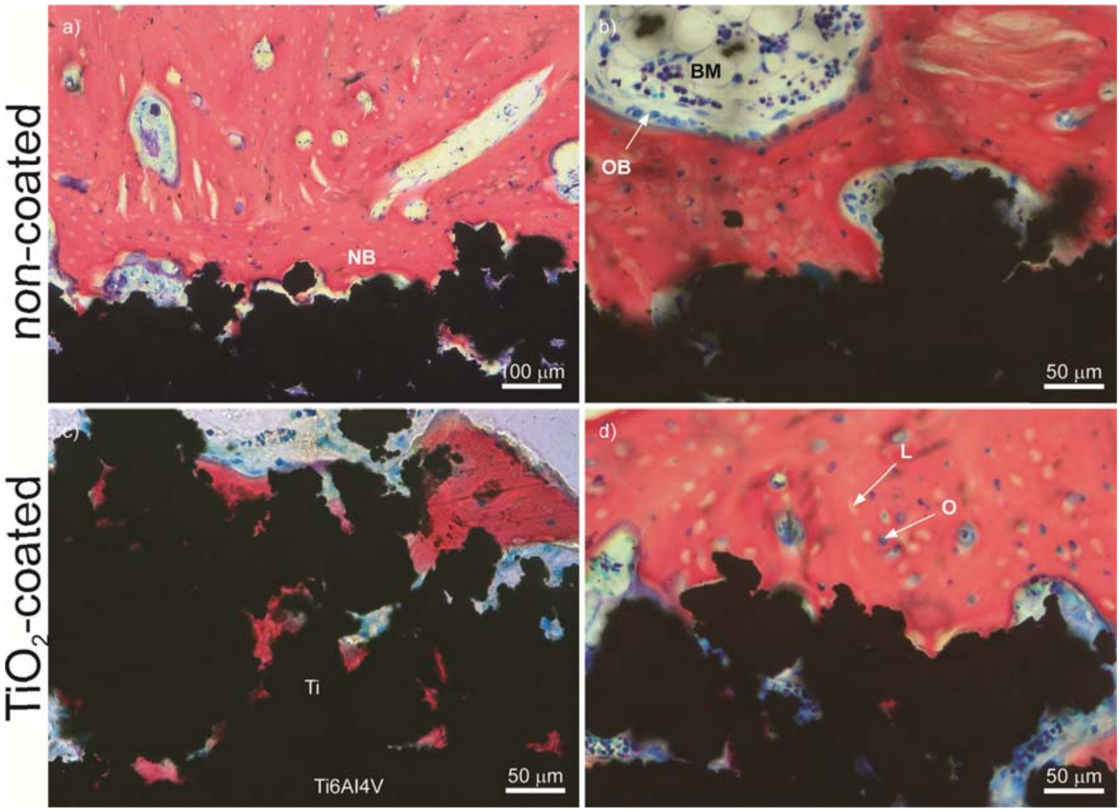

Figure 32: Histological analysis of new mineral bone formation on the non-coated and TiO_2-coated porous titanium. (a, b) A section from the non-coated porous titanium. (c, d) A section from the TiO_2-coated porous titanium. Note the lower magnification in (a). NB, new bone; OB, osteoblast; BM, bone marrow containing fat and blood cells; Ti, titanium; L, lacunae; O, osteocyte.

Occupation of the pores in the titanium surface layer by bone was clearly seen in the bulk cross-sections observed under SEM, which enabled a much more reliable quantification. In contrast to the observations of the slices in transmitted light, with which only the light-transmitting parts of the pores were visible, the total pore opening and the corresponding parts of the pores that were filled with newly formed bone were visible with the SEM. Figure 33 shows a characteristic SEM image of a polished cross-section of the porous region of the non-coated (sample 1) and TiO_2-coated sample (sample 5). The pores were filled, to a large extent, with new mineralised bone (grey phase). Interestingly, this new bone grew into the pores measuring from more than 100 µm (Figure 33, dotted-line square) to just a few micrometres (Figure 33, dashed-line square).

EDS was performed to identify the phases present and confirm the presence of the mineralised bone within the pores. Figure 34 shows the elemental concentration distribution in the bone-implant cross-sections for the non-coated and TiO_2-coated implants. The implant material is characterised by high concentrations of titanium, with a high carbon and chlorine content, indicating the location of the Epon resin in which the samples were mounted, whereas the high calcium and phosphorus concentrations indicate the presence of mineralised bone. Fully mineralised bone (Figure 34, light grey phase) was confirmed by quantitative EDS, which found a Ca/P ratio close to 1.7 for both the non-coated and TiO_2-coated implants.

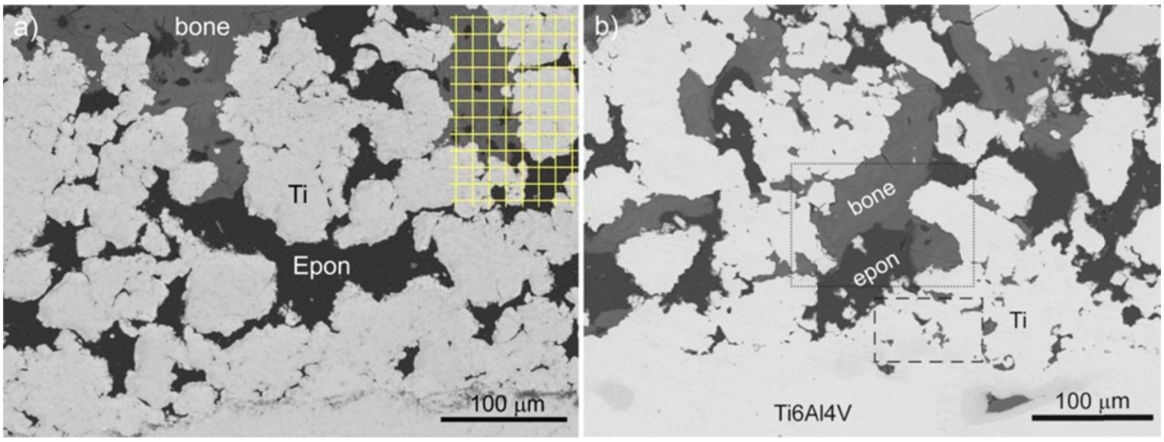

Figure 33: *SEM image of bone ingrowth.* (a) Sample 1, non-coated implant, (b) Sample 5, TiO_2-coated porous titanium, showing bone growth into the porous titanium region. Dotted square: large pore region; dashed square: small pore region. Yellow grid presents a part of a point grid that was used for quantitative point analyses.

a) non-coated

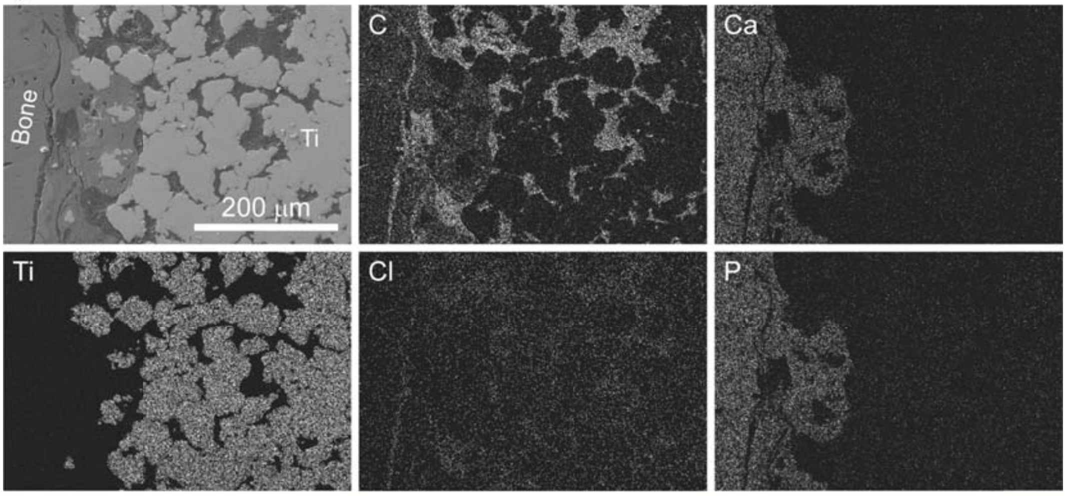

b) TiO_2-coated

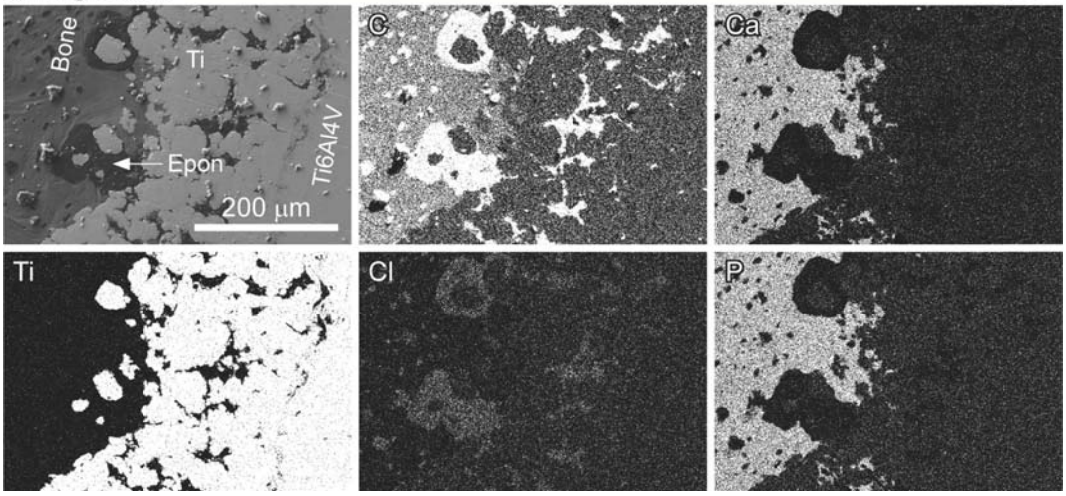

Figure 34: *EDS mapping of a bone implant cross-section.* (a) Non-treated porous titanium, showing (from left to right): SEM image, and elemental composition of C, Ca, Ti, Cl and P. (b) TiO_2-coated porous titanium, showing (from left to right) SEM image, and elemental compositions of elements C, Ca, Ti, Cl and P.

Comparison of the EDS mapping of bone implant cross-sections confirmed that the bone occupied a large portion of the pores in the TiO_2-coated sample with the titanium layer (Figure 34b), but this was not the case for the non-coated implants (Figure 34a). Bone ingrowth was also evaluated quantitatively, with the analysis strictly limited to the porous regions and the point analysis used for the quantification. The analysed region was covered with a point grid using a point separation that was approximately the same size as the average pore size, and then the ratio of hits into the bone *versus* hits into the pores including the bone was evaluated. As the point ratio is equal to the area and volume ratios, we could quantify the bone ingrowth (Figure 35). As expected, greater bone ingrowth occurred with the TiO_2-coated implants, as shown by the highly significant difference ($p<0.01$) of 22 % for the non-coated implants compared to 44 % for the TiO_2-coated implants. In addition, the bone-to-implant contact, which was evaluated using a lineal analysis, was approximately the same for both the non-coated and TiO_2-coated implants, i.e., approximately 45 %.

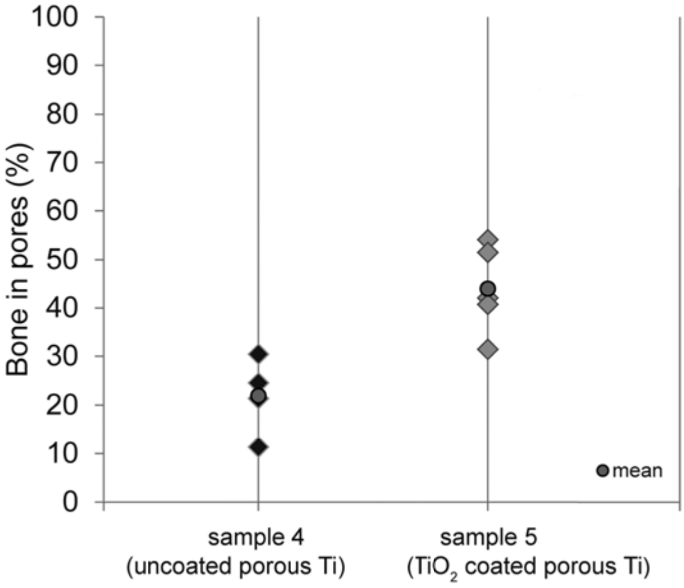

Figure 35: Percentage of bone ingrowth. Percentages of bone seen in the pores of non-treated porous titanium sample (left), and TiO_2-coated porous titanium (right). ◊ value for single measurement, • average of all measurements. ($p<0.01$), TiO_2 coated *versus* uncoated samples.

4.2 Bioactive glass

4.3 Bioactive glass synthesis

Bioactive glass (BAG) was prepared by a sol-gel synthesis in order to obtain particles small enough for coatings inside the pores of porous implants, and to avoid the milling required to form smaller particles after the melting procedure. To coat the pore walls within the porous coating with an interconnective pore throat size of 1 to 30 µm[131] and pore size ranging from 100 µm[166] down to 1 µm, particles have to be smaller than 1 µm, preferentially in the nanometre range.

Different compositions of BAGs were prepared in order to compare and to choose the best candidate for coating in terms of bioactivity, antibacterial properties, crystallinity and sintering properties. The compositions and names of the BAGs are presented in Table 3.

Usually bioactive glass is prepared by melting or polymeric sol-gel synthesis. Bioactive glasses prepared by melting and milling with compositions that are commercially available are presented in Figure 36: bioactive glass 45S5 Bioglass® (NovaMin, Figure 36a) and bioactive glass 53S4P BonAlive® (Vivoxid Ltd., Figure 36b).

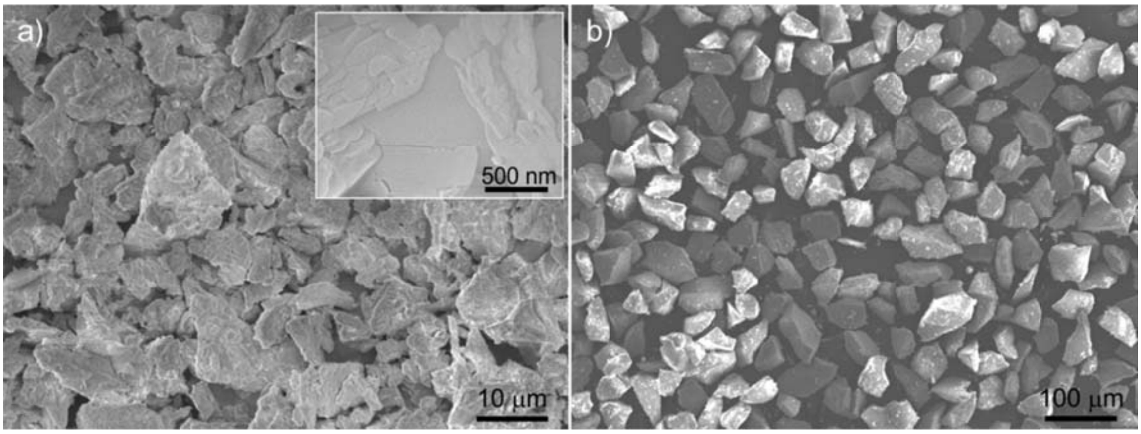

Figure 36: BAG particles. (a) BAG 45S5 Bioglass® (NovaMin); (b) 53S4P BonAlive® (Vivoxid).

In this study BAG powder was prepared by sol-gel process, where polymeric sol-gel, was used to prepare the first batch of BAG. For the polymeric sol-gel route an acidic catalyst is used to accelerate the hydrolysis and after gelation the bulk wet gel is dried and then ground to obtain powder (route 1, Figure 39a). Polymeric sol-gel BAG powder with a composition (mol.%) $70SiO_2$-$30CaO$ (named 70S) is presented in Figure 37. As the size of the BAG particles prepared by polymeric route was still too big, further milling would be unavoidable for use in coatings. The measured particle size d_{50} for those BAG powders was ~100 µm (Table 13).

To avoid milling, and to achieve a smaller particle size, the sol-gel process was modified. A slow gelation, which is usual for a standard polymeric route, was accelerated by a sudden increase of the pH after hydrolysis completion. Ammonia was poured into the sol while vigorously stirring (route 2 in Figure 39a). The sol immediately transformed into a wet fluffy gel that in contrast to the above procedure became a powder after drying. The size of the particles slightly decreased ~60–80 µm (Figure 37b and Table 13). The insets in Figure 37a and Figure 38a show the surface of the sol-gel BAG particle at a higher magnification. The surface of particles prepared by the sol-gel is highly porous and particles are composed of nanosized sub-units, while the surface of the melt-derived particles is smooth (Figure 36a). Even though the particle size was not drastically decreased the surface area was increased due to a different surface structure.

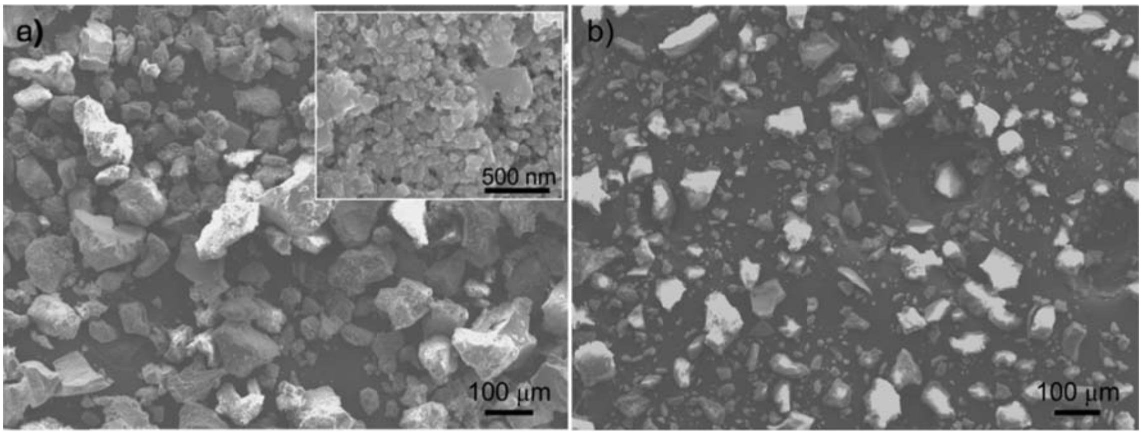

Figure 37: BAG particles. (a) BAG powder prepared by polymeric sol-gel route; (b) BAG powder prepared by polymeric sol-gel route with accelerated gelation.

As the particle size obtained using the polymeric sol-gel route, with both slow and fast gelation, was still not sufficiently small to avoid milling and contamination, we replaced the acid catalyst with a base and accelerated both the hydrolysis and condensation reactions at the same time. The BAG particles were prepared by the so-called particulate sol-gel route. Reactants were slowly dropped into the mixture of water and ethanol, where they hydrolysed and condensed due to the high pH reached in the mixture by the addition of ammonia. The pH was kept high enough to make particulates, but still below the pH limit for calcium hydroxide precipitation. As sudden pH increase can also result in unwanted phase formation, ammonia was carefully added dropwise and the pH was kept constant throughout the whole synthesis to achieve the same conditions for all the drops of reagents. Instead of a polymeric sol (Figure 40a), which is later transformed to a viscous gel, a colloid sol was formed. The colloid sol has the form of a white suspension (Figure 40b). A schematic presentation of the conventional polymeric route for BAG synthesis and the developed particulate route is presented in Figure 39.

Such a colloidal sol gave much smaller particles compared to the polymeric route. They were spherical with a size between 100 and 200 nm, but highly agglomerated. The average agglomerate size that depends on the synthesis conditions varied from 11 to 13 µm and was still smaller than the size of the non-agglomerated particles prepared by the polymeric sol-gel route.

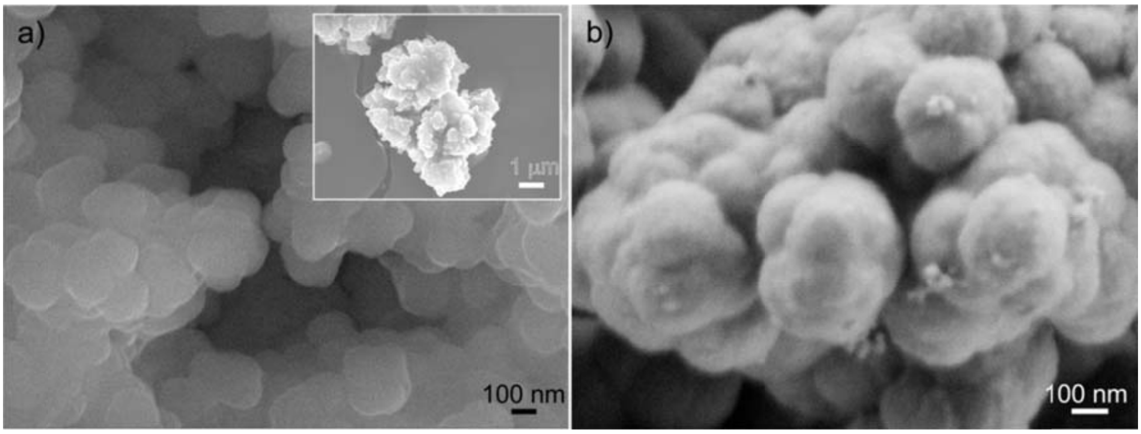

Figure 38: BAG powders prepared by the particulate sol-gel route: (a) BAG 53S, the inset show the BAG agglomerate and (b) BAG 70S. Note the marker difference.

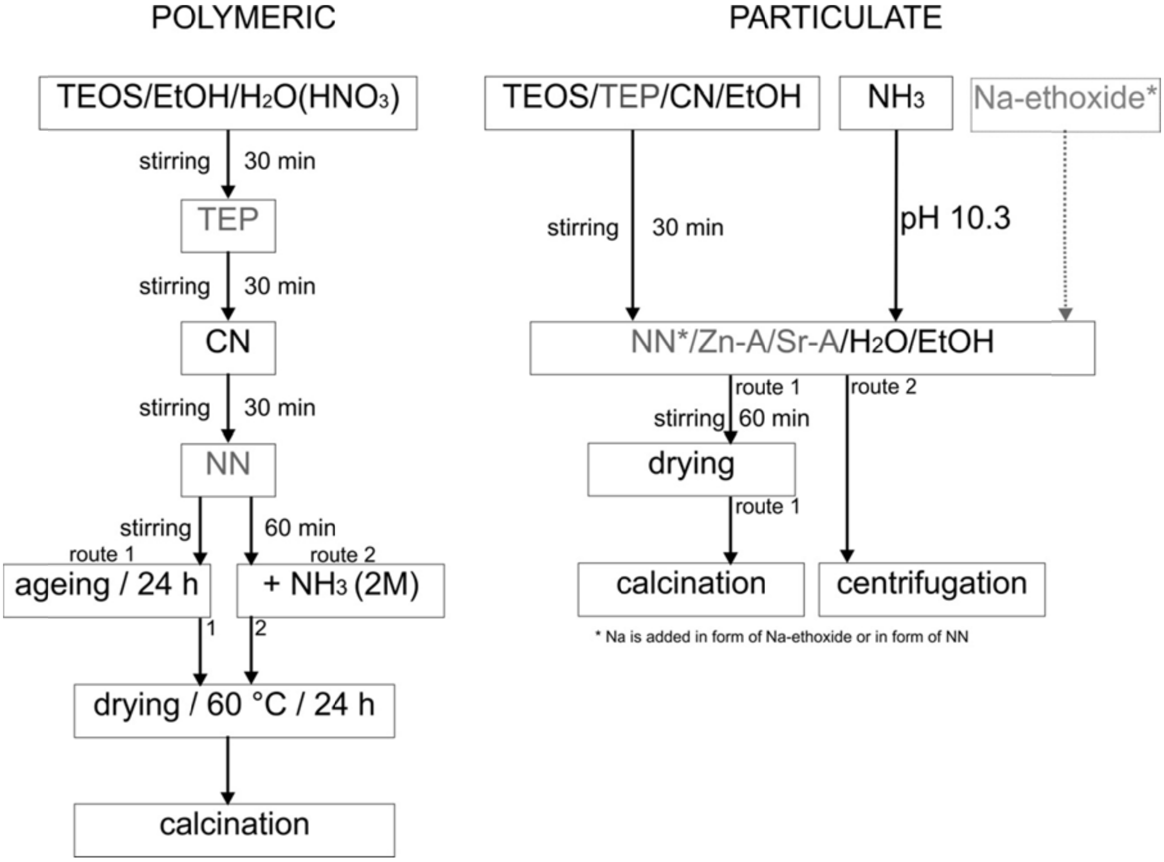

Figure 39: Schematic presentation of polymeric and particulate sol-gel routes for BAG. Reagents in grey are added according to BAG composition, reagents in black are added in all BAG compositions. See abbreviations in chapter 3.2.2.1.

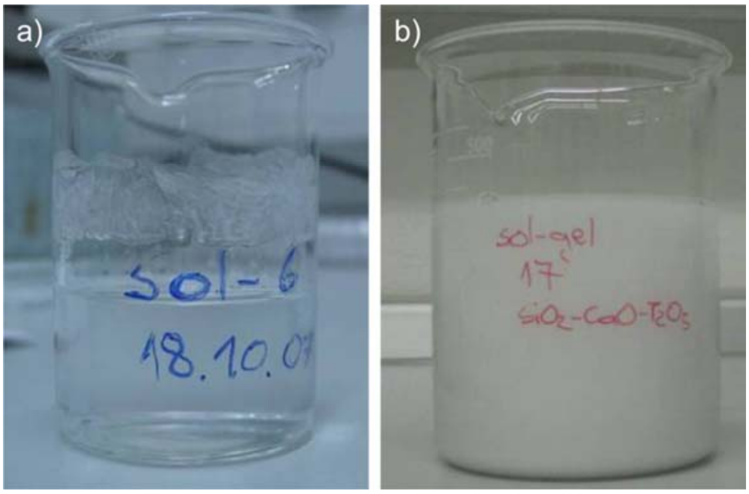

Figure 40: (a) Polymeric and (b) particulate sol.

The particle sizes for BAG prepared by different methods are presented in Table 13. Commercial BAGs (45S5Bioglass® and 53S4P BonAlive®) have a very different particle size, where 45S5 is most probably milled. The particle size of the glass BonAlive® 53S4 is similar to the BAGs prepared by the polymeric sol-gel route in this study, where the size was slightly smaller when the gelation was accelerated. A considerable decrease can be seen when the BAG was prepared by particulate sol-gel. The particle size is around 100–200 nm, however the powder is strongly agglomerated, as shown in Figure 38, therefore the measured value represents the size of the BAG agglomerate.

Table 13: Particle size of BAG prepared by different methods and with different compositions, measured with a laser scattering particle analyser

Synthesis method	BAG name	d_{50} (µm)	
melting	45S5 (NovaMin®)	9	commercial
sol-gel	53S4 (BonAlive®)	81	
polymeric sol-gel	70S	93	self-prepared
polymeric sol-gel	53S	107	
polymeric sol-gel /accelerated gelation	70S	66	
polymeric sol-gel /accelerated gelation	53S	60	
polymeric sol-gel /accelerated gelation	58S4Sr	82	
polymeric sol-gel /accelerated gelation	58S4Zn	59	
particulate sol-gel	53S	13	
particulate sol-gel	70S	11	

To avoid particle agglomeration, the zeta-potential (ZP) was measured during BAG synthesis to see what causes the agglomeration. As presented in Figure 41, the sol containing only SiO_2 and P_2O_5 was stable, with a negative potential around -40 mV. When nitrates (Ca and Na) were added into the sol the ZP jumped to +14 mV, close to the isoelectric point, which caused agglomeration of the fine particulate sol particles. The agglomeration of the particles was caused by the change in ZP during the sol-gel synthesis. We found that smaller BAG particle could not be reached during the sol-gel synthesis due to the low surface charge of the particles during the synthesis.

To increase the ZP the powder was washed with water and ethanol by centrifugation after synthesis (route 2, Figure 39b), as reported by Hong[92] and Labbaf[94]. Washing should eliminate the residual unreacted species and organic components, thus lowering the conductivity and therefore increasing the ZP.

When BAG powder was washed the pH decreased by more than one unit, however the ZP did not change. By adding more ammonia the ZP increased to 40 mV (Figure 41), resulting in a more stable suspension and smaller particles. Unfortunately, this was caused by washing away the loosely bound Ca and Na ions from the silica network. The BAG composition after centrifugation is presented in Table 14 below the dotted line, whereas the compositions without centrifugation are presented above the dotted line. The final composition of BAG powders was determined, after calcination, by SEM EDS analyses. Two powders, 53S and 70S, were washed. It can be seen that the concentration of Ca and Na is strongly decreased and the residual glass is therefore mainly SiO_2. The ratio between SiO_2 and P_2O_5 before and after centrifugation remained similar, which shows that P content is not affected with the centrifugation.

Due to the drastically changed BAG compositions, the centrifugation was not used for further experiments and was also not performed on the BAG 58S4Sr and 58S4Zn.

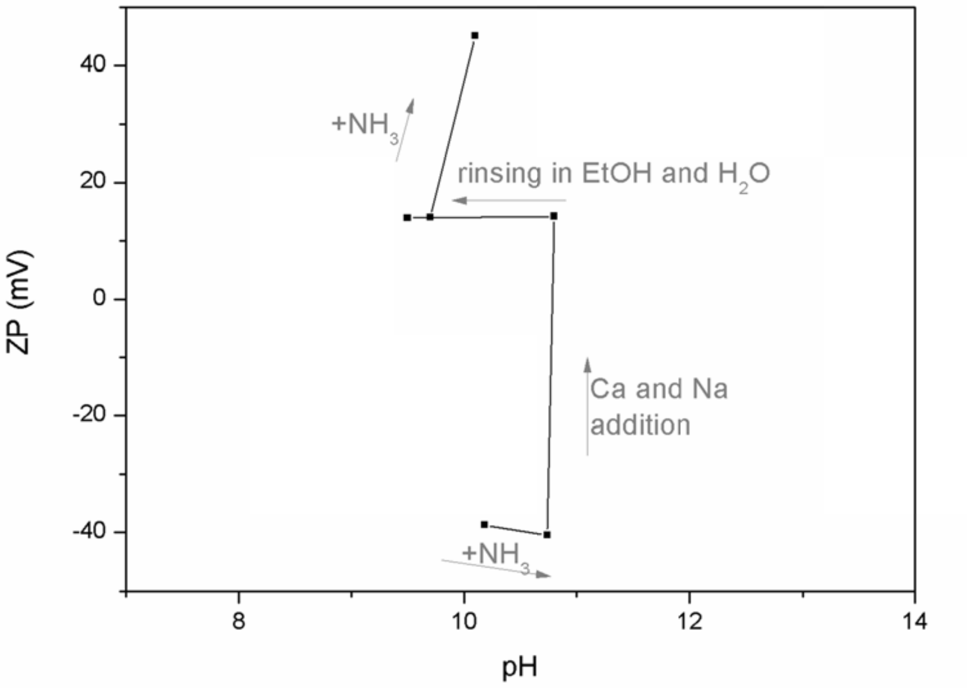

Figure 41: Dependence of ZP of the BAG sol on the reactants' addition during the particulate sol-gel process.

Table 14: BAGs compositions determined by EDS analyses. ± values are standard deviations, the mean value were determined by averaging 4 measurements. Powders were MW dried.

BAG	wt.% / *mol.%						
	SiO_2	CaO	P_2O_5	Na_2O	SrO	ZnO	
70S*	69.7±0.3	30.3±0.3	/	/	/	/	without washing
53S	53.8±0.6	21.8±0.3	1.7±0.2	22.7±0.3	/	/	
58S4Sr	56.6±2.2	31±1.6	8.4±0.6	/	4±0.2	/	
58S4Zn	59.6±1.6	28.6±0.9	6.9±0.4	/	/	4.9±0.3	
70S*	84.6±1.4	15.4±1.4	/	/	/	/	with washing
53S	85.9±0.3	7±0.3	6.5±0.4	0.6±0.1	/	/	

4.3.1 Sintering studies

To determine the appropriate sintering temperature, dilatometry, thermogravimetric analysis (TG), differential scanning calorimetry (DSC) and X-ray diffraction (XRD) were carried out.

Differential scanning calorimetry and thermogravimetry curves for two BAG compositions are presented in Figure 42. As the heating process proceeds, a three-step weight loss is observed for the BAG 53S, ending in a final weight of 43 % of the starting mass and a two-step weight loss for the BAG 70S ending in 46 % of the starting mass. The first loss between 50–150 °C is about 25 % for both compositions and is accompanied by a broad endothermic peak in the DSC curve that corresponds to a loss of water. Up to a temperature near 480 °C the mass remains quite stable, while there is a second big loss of about 22 % at around 500 °C. The DSC shows a sharp endothermic peak in this area for which the mass spectra showed the presence of NO and O_2 groups (M30 and M32). As both compositions had this peak, the nitrate groups belong to calcium nitrate tetrahydrate used as a precursor for CaO. Above 550 °C no significant mass loss (6 %) was observed for BAG 70S, while BAG 53S has another broad DSC peak between 620 and 660 °C with an accompanying additional 13 % of mass lost. This peak is correlated to the loss of NO and O_2 groups from $NaNO_3$ as a starting precursor for the Na_2O. A small (3 %) loss of mass for BAG 53S is observed close to 800 °C, also coming from the loss of NO and O_2 groups, whereas no peak is observed for BAG 70S at this temperature. The DSC curve shows that nitrates from calcium nitrate cannot be removed till 600 °C and therefore the calcination temperature should be higher than 600 °C. Due to the calcination, the overall DSC curve shows exothermic behaviour.

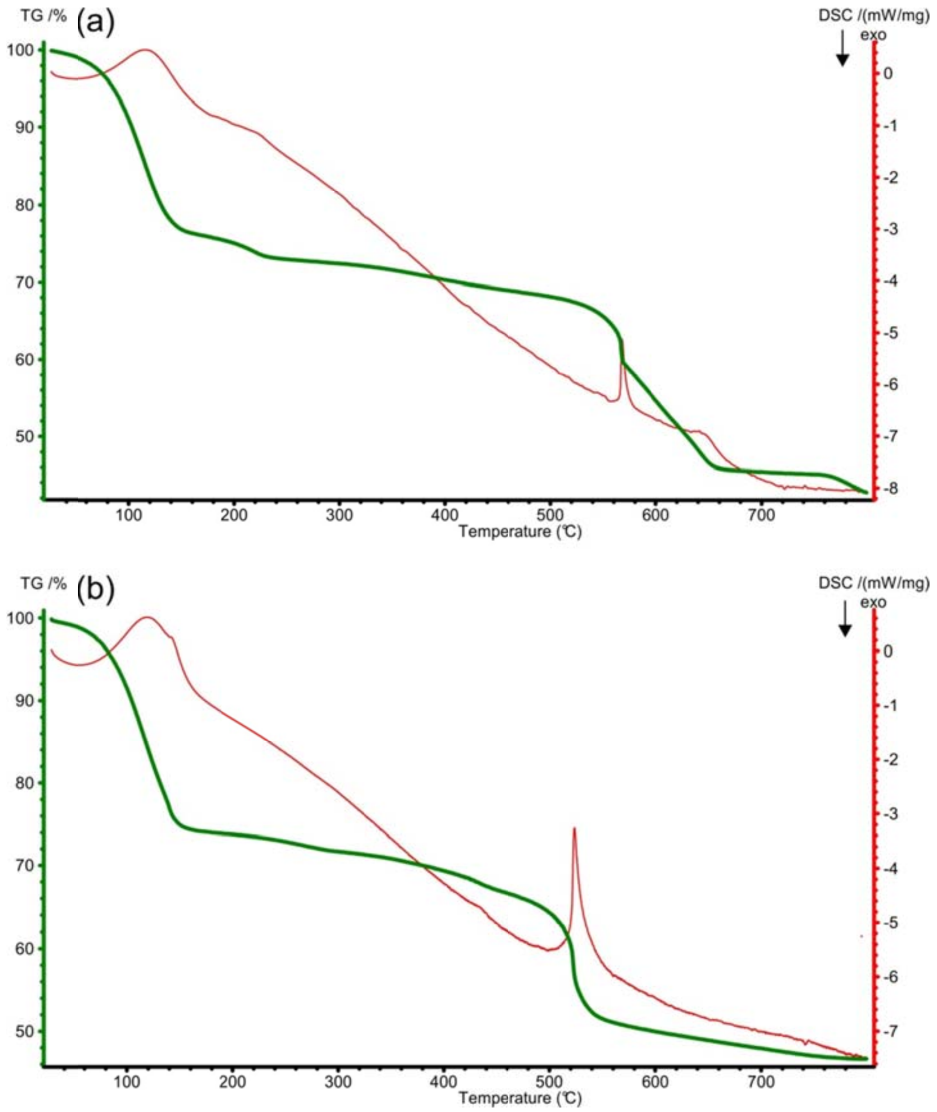

Figure 42: TG and DSC curves for (a) BAG 53S and (b) BAG 70S.

In Figure 43 the TG and DSC curves for BAG prepared from nitrates as well as acetates are presented, BAG containing Sr. As peaks in the DSC curve are not clearly visible, mass spectra curves are added to the graph. The weight loss is significant till 570 °C, similar to previous compositions, and is diminishing at higher temperatures. The overall weight loss is 41 %. Mass spectra showed a loss of water between 50–150 °C. The largest loss of nitrate groups, coming from decomposition of calcium nitrate, is present at 550 °C, whereas another two peaks are detected at 220 °C and 400 °C. The gaseous product from the decomposition of acetate, CO_2, appeared at around 400 with the highest concentration at 560 °C and another small peak at 620 °C. No peaks were detected after this temperature.

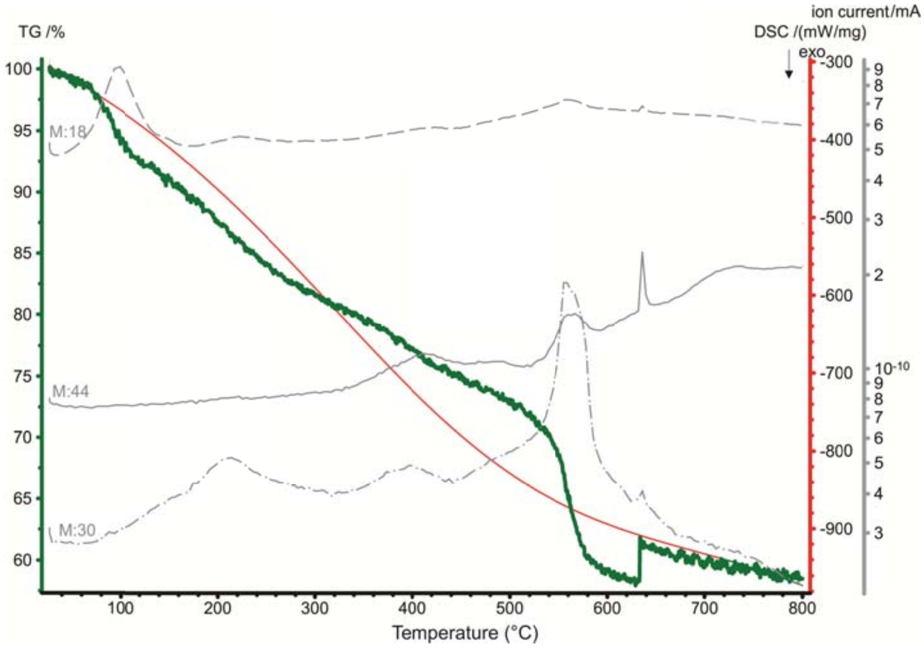

Figure 43: TG, DSC and MS curves for BAG 58S4Sr.

Dilatometric curves of powder compacts of different BAG compositions are presented in Figure 44. According to the results BAG 70S, 58S4Zn and 58S4Sr can be sintered at similar T, i.e., 850 °C, 810 °C and 850 °C, respectively. When Na is added into the BAG composition the sintering starts at much lower temperatures ~ 600 °C and at 650 °C the shrinkage turns into expansion due to formation of gases from species that were not removed during the BAG calcination. After the removal of all the gases the shrinkage can be seen again and is completed at 810 °C. The shrinkage during sintering, except for 53S, is around 8 %.

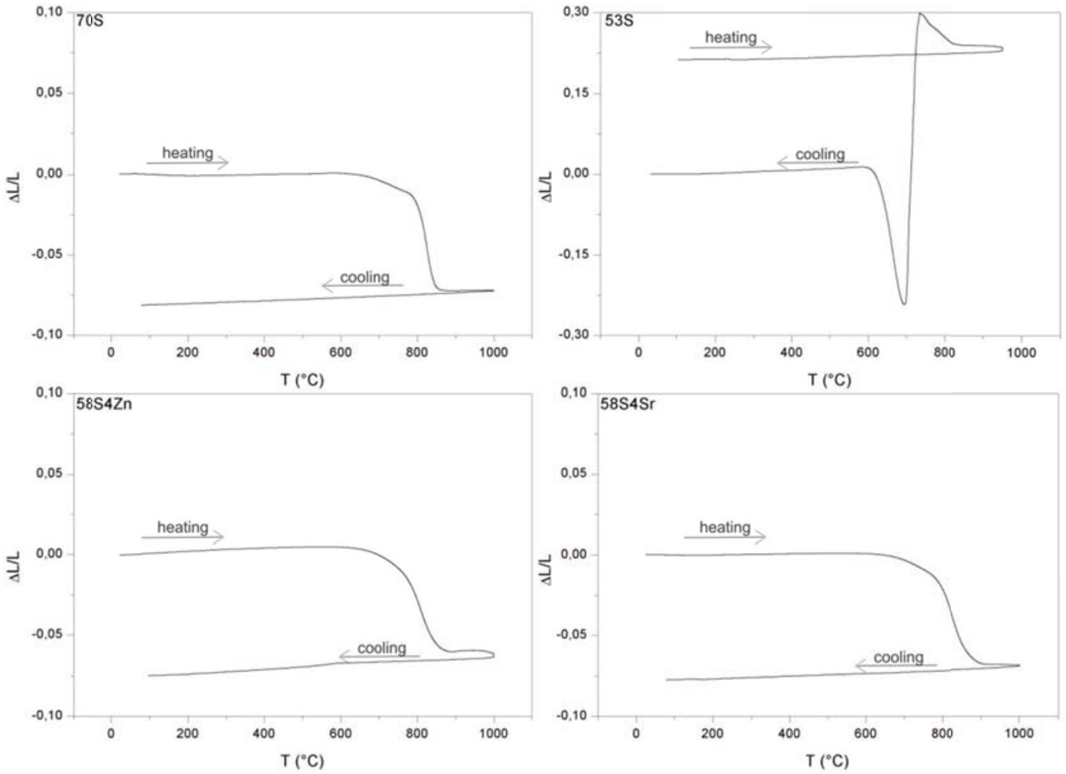

Figure 44: Dilatometer curves for BAG 70S, 53S, 58S4Zn and 58S4Sr.

According to the literature data the bioactivity is decreasing with the crystallinity of BAG, therefore the crystallization that may occur during sintering was determined by XRD.

The XRD spectra are presented in Figure 45. As shown in Figure 45a, the two-component BAG 70S stayed completely amorphous till 900 °C, which is above its sintering temperature (850 °C). The BAG 58S4Zn, despite Zn incorporation, remained amorphous till its sintering temperature (Figure 45c), whereas a broad peak in BAG 58S4Sr (Figure 45d) was detected, corresponding to formation of Calcium silicate crystalline phase. The highest affinity for crystallization was observed for BAG 53S, where at 800 °C the peaks corresponding to calcium sodium silicate and silica peaks are detected (Figure 45b).

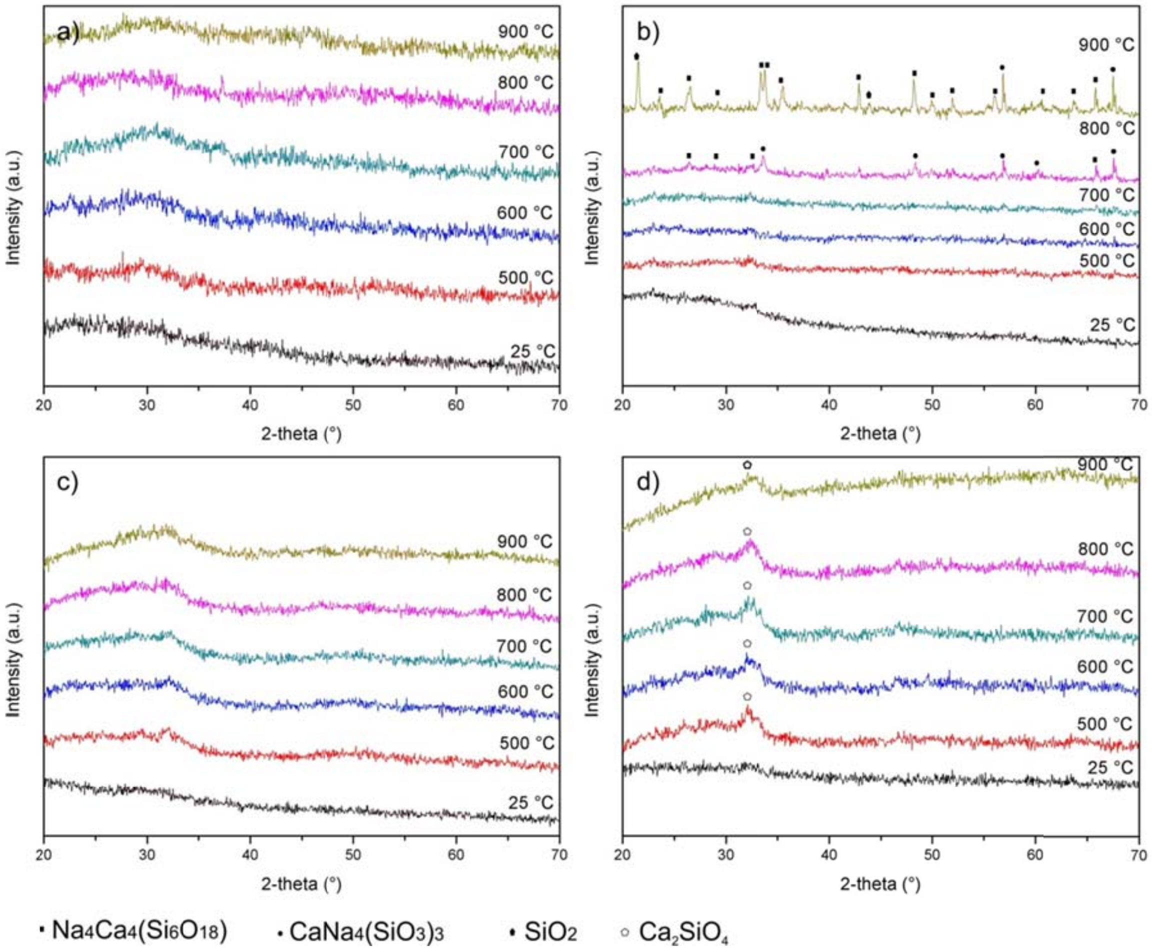

Figure 45: XRD spectra at different temperatures for BAG compositions: (a) 70S, (b) 53S, (c) 58S4Zn and (d) 58S4Sr.

Figure 46 presents SEM images of BAG samples sintered at temperatures evaluated with a dilatometer. The BAG powders were previously calcined at 600 °C for 2 hours. Calcination is necessary to remove the residual nitrates (see page 42, Figure 42). The same calcination T was also used for BAG 53S that should be calcined at 800 °C, but at this T it begins to crystallize and to sinter. Due to uncompleted calcination and consequential bubbles formation the pellet became highly porous (Figure 46a). Other samples were less porous but had a lack of homogeneity, as seen in the backscattered electron image (Figure 46b, c). To improve homogeneity a standard drying of powder prepared by particulate sol-gel method in a heating chamber was replaced by microwave (MW) drying. The more homogenous composition of MW dried and sintered BAG can be seen in Figure 46d.

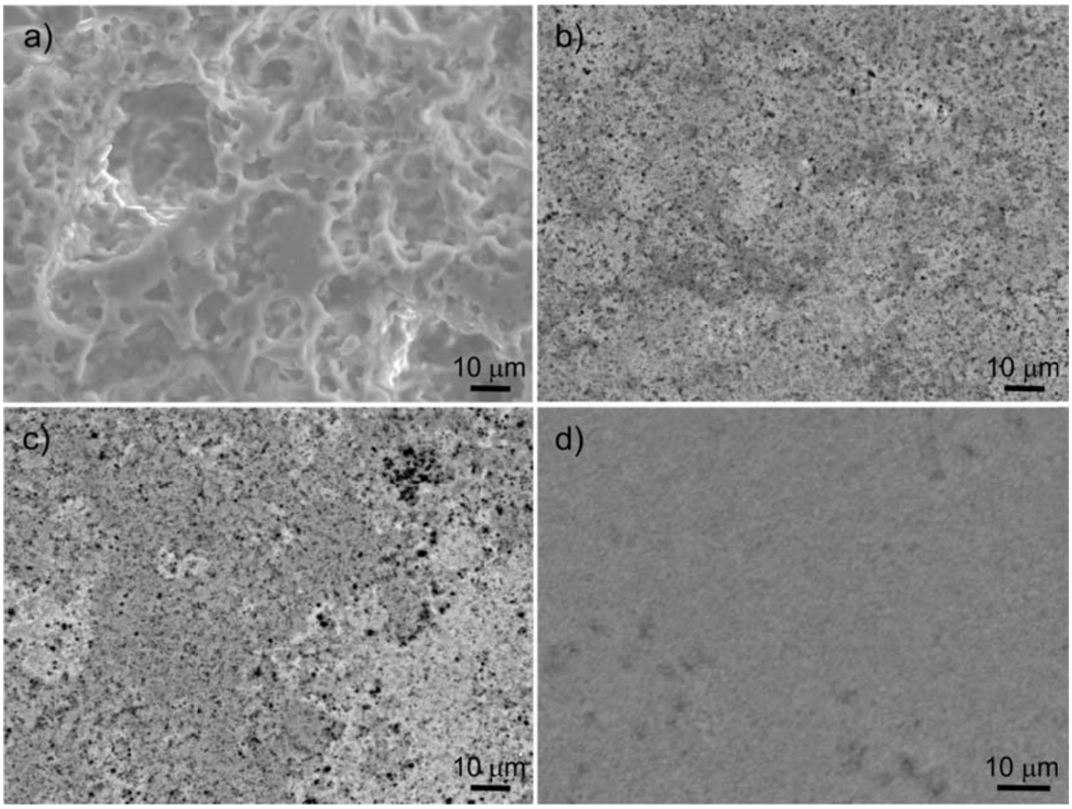

Figure 46: SEM image of BAG after sintering: (a) BAG 53S, (b) BSE image of BAG 58S4Sr, (c) BSE image of BAG 70S dried at 70 °C, (d) BSE image of BAG 70S dried in microwave oven.

To avoid the formation of gases and high porosity of the BAG 53S due to calcination during sintering, sodium nitrate was replaced with sodium ethoxide. The sol-gel process had to be modified in order to prevent an increase of the pH above 11 due to basic ethoxide. The amount of NH_4OH was therefore lower and the pH was mainly controlled by the ethoxide dropping (route 3 in Figure 39). TG measurements showed that the overall mass loss is 40 %, similar to the BAG 53S prepared from nitrates (Figure 47). There are three main weight losses. The first two endothermic DSC peaks, from 50 to 150 °C, are ascribed to the loss of water. The second loss ascribed to decomposition of acetates is from 150 to 350 °C. The third mass drop starts at 600 °C for which the mass spectrum shows the presence of NO and mainly CO_2. By using ethoxide instead of salts the thermal conversion to oxides is finished at 720 °C. Those samples therefore had to be calcined at higher temperatures than the ones synthesised from the salts. According to the dilatometric curves the sintering started at 800 °C, therefore pellets were sintered at 900 °C. The sintered pellet had no macropores (Figure 48b) but were partially crystalline (Figure 45b and grey dots in Figure 48b).

For the further experiments, as well as for *in vivo* tests, Na in a form of $NaNO_3$ was used due to simpler sol-gel route and because at final BAG was meant to be used as a coating in porous system, where bubbling is not a disadvantage.

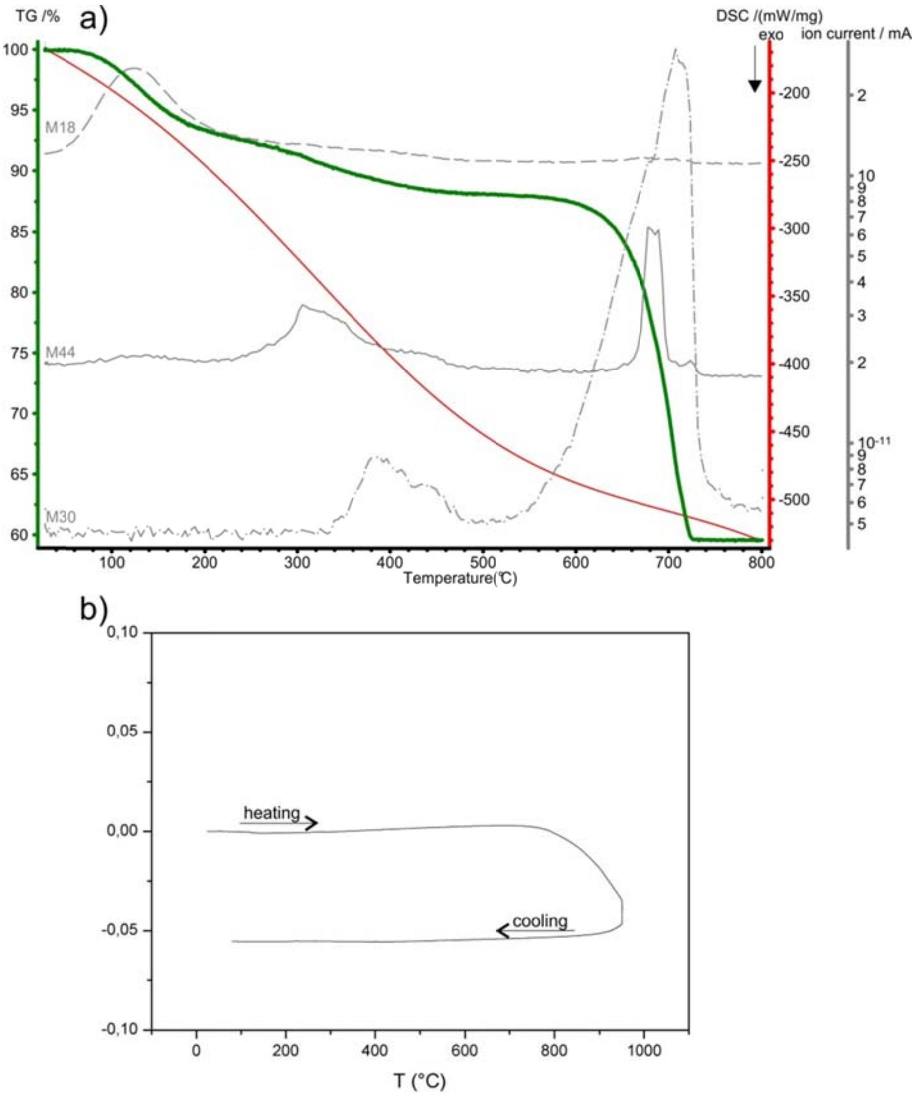

Figure 47: (a) TG, DSC and MS curves and (b) dilatometer curve for BAG 53S prepared from sodium alkoxide as a Na_2O precursor.

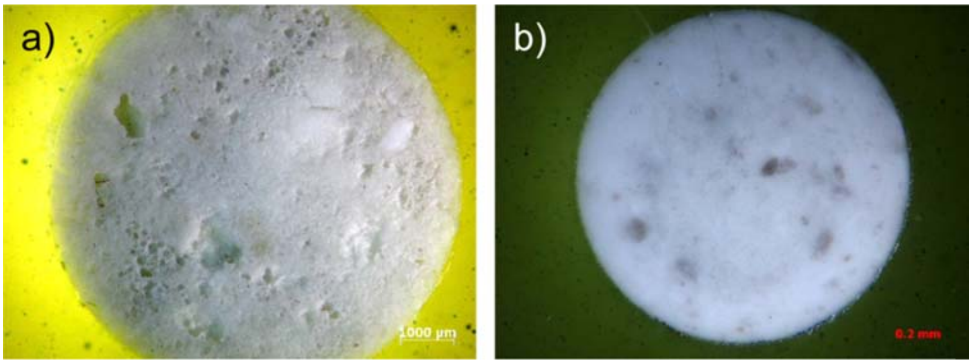

Figure 48: Optical micrograph of sintered BAG 53S pellet prepared by sol-gel from; (a) nitrates and (b) alkoxides.

4.3.2 FTIR

Figure 49 shows the FTIR spectra, in the 400–2000 cm^{-1} spectral range, for BAG powders after calcination at 600 °C. Bands are located at around 463, 810, 930, 1070, 1210, 1420 and 1490 cm^{-1}. The bands positioned at 463, 810, 930, 1070, 1210 are related to the silica network; the band at 463 to Si-O-Si symmetric bending, 810 to Si-O to symmetric stretching of bridging oxygen between tetrahedron, at 930 to Si-O stretching of non-bridging oxygen (NBO), 1070 and band at 1210 cm^{-1} to symmetric and asymmetric stretching of Si-O-Si. The band at around 1070 also belongs to the P-O stretching vibrations[92]. The band at around 1420 cm^{-1} found in a spectrum of BAG 53 is assigned to the asymmetric stretching vibration of ionic nitrate[132] left in the glass after a thermal treatment at 600 °C. The bands at 880 and 1490 cm^{-1} found in the BAG 58S4Zn spectrum may be attributed to vibrations of the C-O groups from acetates also left after the thermal treatment of glass.

The main difference between the spectra is in a shoulder at 930 cm^{-1} that indicates the presence of NBOs and is ascribed with two NBO per silica tetrahedron, i.e., $Si\text{-}O^-$ that is ionically bound to Ca^{2+} or Na^+ counter ions or are showing the presence of Si-OH groups. Si-OH groups are important for the bioactivity for HAp nucleation[133] as are NBOs, as they break the lattice connectivity and thus assure faster degradation of the material and faster leaching of ions. The strongest band is present in BAG 53S that has consequentially the lowest network connectivity and should therefore be the most bioactive. A strong band at this wavelength is also seen in BAG 70S and a weaker band for BAG 58S4Sr. BAG containing 4 % of Zn has a narrow, almost no band for NBO groups, thus this BAG has a very good silica network connectivity.

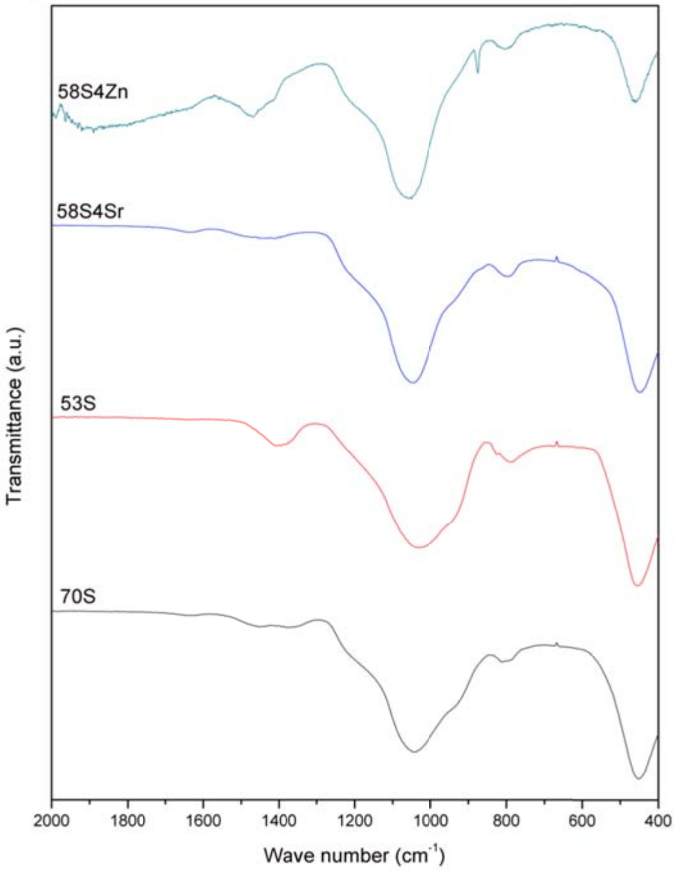

Figure 49: FTIR spectra of powders; 70S (black), 53S (red), 58S4Zn (blue) and 58S4Sr (green).

4.3.3 pH change of the BAG immersed in SBF

The pH change of the BAG powder and the sintered pellet immersed in SBF was measured with time (Figure 50). The pellets were sintered at temperatures evaluated by sintering studies (810 °C for 58S4Zn and 53S, 850 °C for 70S and 58S4Sr). The change of the pH induced by the powders was measured in a suspension and for the pellets on their surface. The pH values were measured to access the possible effect of an increased pH on bacteria and cell growth. SBF was used to achieve similar conditions to a human environment.

Different BAG powders a caused different pH change in the range between 8 and 10. The highest values were reached with BAG 70S and 53S; 70S due to the smaller particle and agglomerate size and 53S due to the Na_2O content. It is worth to mention the difference between the curves for the same BAG powder composition, 53S, but prepared by different methods, particulate and polymeric. Much bigger polymeric BAG (53S pol) particles with a smaller surface area are dissolving slower and are therefore not increasing the pH so fast.

The pH measured in SBF close to the surface of the sintered BAG is lower than for the powder suspensions. The highest pH value isa not reached anymore by BAG 70S but by 53S, which became highly porous after sintering due to the loss of nitrates. The lowest pH increase is actually reached by 70S, which is pointing at its lower solubility. The difference in pH for sintered BAG is, however, not as big as it is for BAG powders. Also, the absolute values are lower (< pH9).

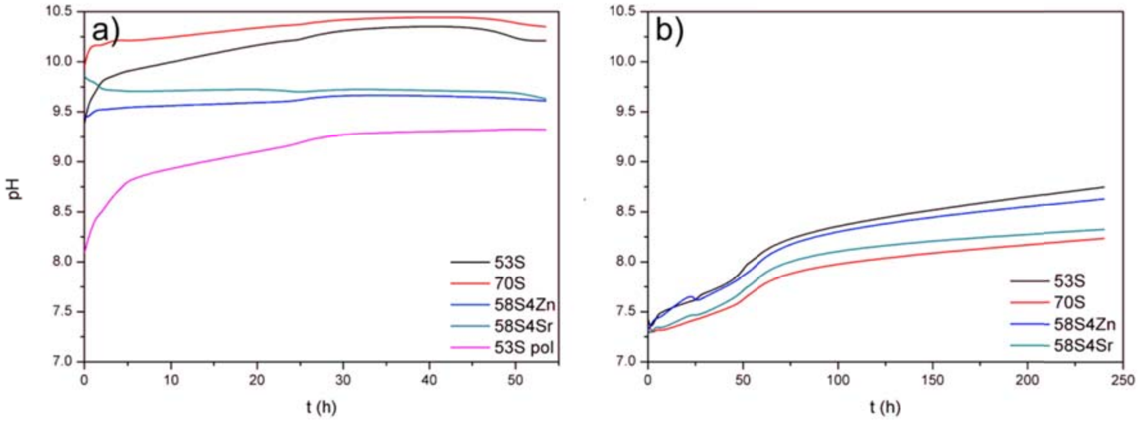

Figure 50: pH change of BAG during immersion in SBF: (a) for BAG powder dispersed in SBF and (b) close to the surface of sintered BAG pellets.

4.3.4 Bioactivity testing

Bioactivity of the BAG was evaluated the same way as for the TiO_2 coatings; by immersing sintered BAG pellets in acellular SBF. However, the time of immersion for BAG was much shorter, 5 days, because the HAp formation was much faster. All the compositions showed excellent acellular bioactivity. After 5 days of immersion all the surfaces were covered with cauliflower-like HAp (Figure 51).

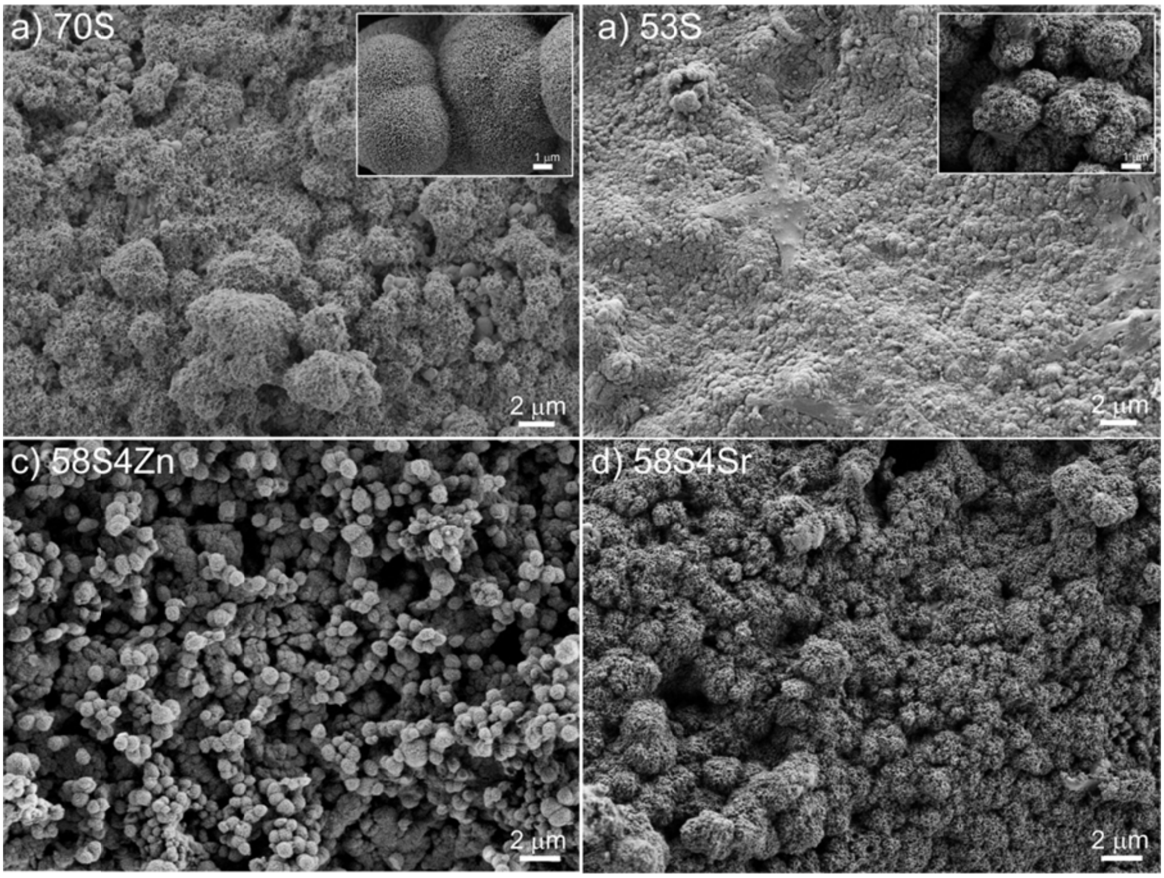

Figure 51: Hydroxyapatite layer formed on BAG surface after 5 days immersion in SBF for BAG compositions: (a) 70S; (b) 53S; (c) 58S4Zn; (d) 58S4Sr.

The most dense layer was formed on BAG 53S. No BAG can be seen on the surface as it is completely covered with HAp crystals. The least bioactive was BAG 58S4Zn where the HAp crystals were small and the rate of their formation was the lowest. The HAp crystals were not observed on the surface until day 5, whereas for other compositions the HAp was formed on the surface already after day 1.

The formation of HAp with time is presented on BAG 70S in Figure 52. The beginning of the HAp formation can be seen already after 24h, after 3 days the surface is almost fully coated and after 1 month there is a thick HAp on the surface. The dissolution of BAG in SBF is also seen on these pictures as around 0.5 µm holes in the BAG surface after 1 and 3 days, but not after 1 month, when HAp has completely overgrown the surface.

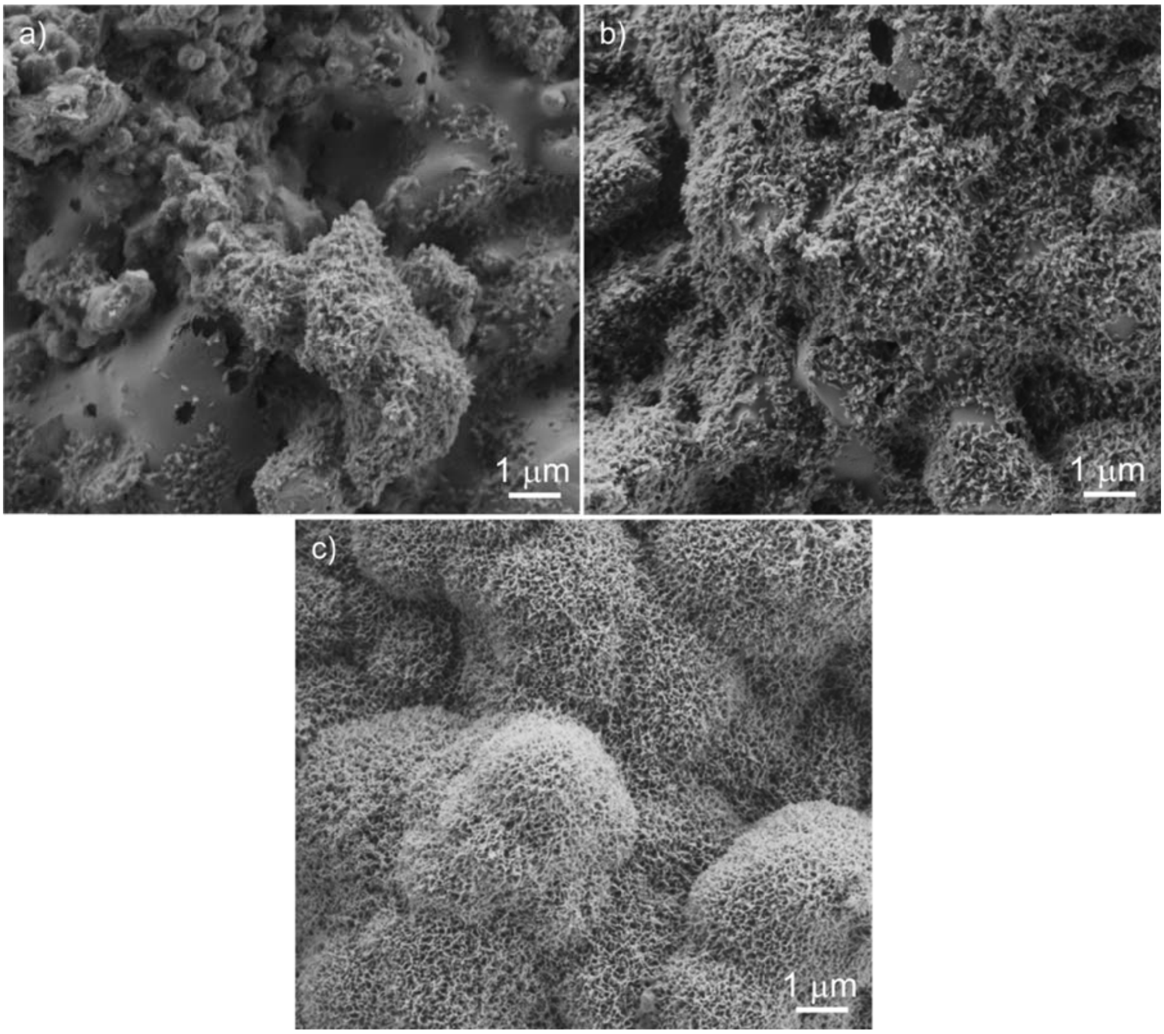

Figure 52: Hydroxyapatite formation on BAG 70S pellet sintered at 850 °C for different immersion times in SBF: (a) 24 h; (b) 3 days; (c) 1 month.

The HAp crystalline phase was confirmed by EDS detection of Ca/P ratio that was 1.67, which is a characteristic ratio for HAp. A more precise analysis to confirm HAp was made with FTIR spectroscopy (Figure 53) that can distinguish HAp from other calcium phosphate phases by splitting of the P-O bending peak near 610 cm^{-1} and 566 cm^{-1}.

The unsoaked BAG sample has bands at around 1210, 1070, 810, 465 cm^{-1} that are related to the Si-O-Si stretching of bridging oxygen and the peak around 930 cm^{-1} that is attributed to non-bridging oxygen. The latter corresponds to Si-O$^-$ vibrations, whose negative charge is compensated by cationic species (Ca^{2+}) or simply to Si-OH groups[134, 135]. After 5 days of immersion the intensities of the silica network are diminishing and new bands arise at 566 and around 1068 that are related to P-O bending. The band at ~880 cm^{-1} corresponds to CO$_3^{2-}$, incorporation of carbonate into the apatite, resulting in nonstoichiometric HAp – hydroxycarbonated apatite[136, 137]. After 1 month the silica network is not seen anymore. Vibrations corresponding to PO$_4^{3-}$ are clearly visible instead. The splitting of the bending peaks near 610 and 566 cm^{-1} is a clear evidence for crystalline hydroxyapatite[134, 138].

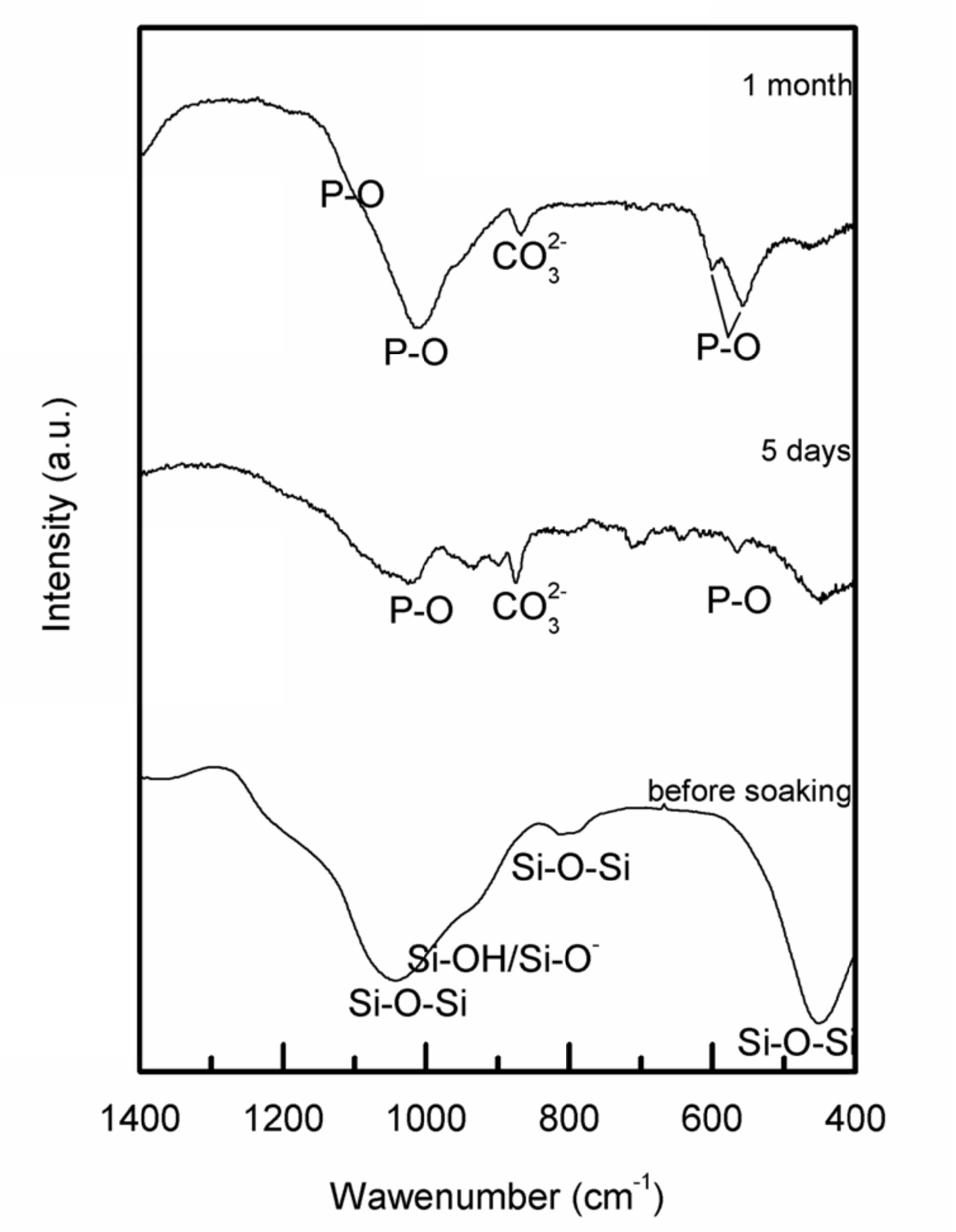

Figure 53: FTIR spectra of BAG 70S before soaking in SBF, after 5 days and after 1 month of soaking.

4.3.5 Bacterial testing

In order to evaluate and to compare the effect of different compositions, pH and dissolved BAG ions from sintered BAG pellets on bacteria growth, bacteria tests were performed in two ways. First, the optical density at a wavelength of 600 nm (OD600) of the supernatants was measured to evaluate the effect of BAG dissolution on bacteria in the surroundings. Then biofilm formation on surface of BAG sintered pellets was quantitatively evaluated by counting the colony forming units (CFU) upon detachment of the biofilm after incubation of BAG with bacteria.

Optical densities (OD) of the supernatants after 24, 48 and 120 hours were measured to see the effect of leaching ions from the BAG on bacteria in the surroundings. The results of OD600 are presented in Figure 54. The OD600 between 0.3 and 0.5 corresponds to 10^8 cells/ml.

No growth was observed for S. *epidermidis* after 24 hours due to bacteria sensibility. To start their growth, they had to be gently mixed with a pipette. The inhibition effect on bacteria growth can be seen for BAG 53S and for BAG 58S4Sr, for both S. *epidermidis* and S. *aureus*. Some inhibitory effect is also demonstrated by the two component BAG 70S, but the effect is present only after the first day of bacteria growth and is almost completely diminished after 48 hours. There was a strong influence of dissolved ions from BAG 58S4Sr on S. *epidermidis*. The same composition has a smaller effect on less sensible bacteria, S. *aureus*, where the bacteria growth is strongly inhibited after the first 24 hours but is lost after a longer incubation time.

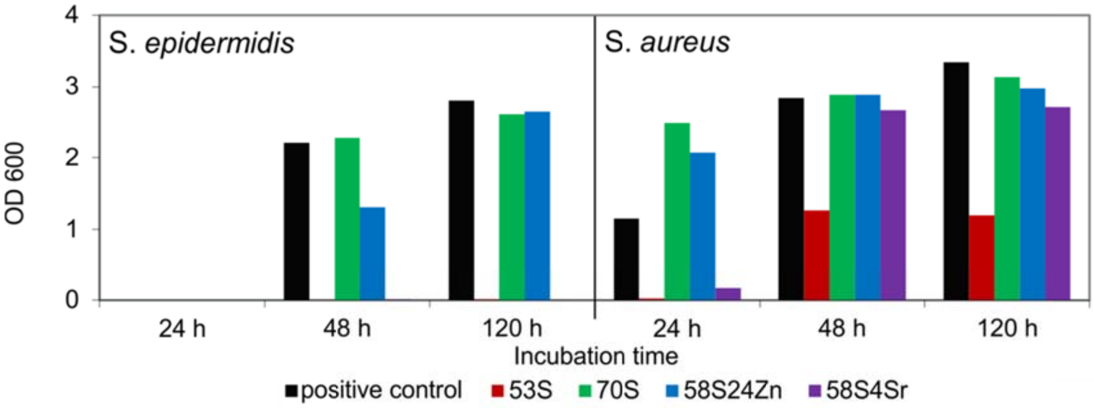

Figure 54: OD600 measurements. Comparison of S. *epidermidis* and S. *aureus* growth in BAG surrounding for different BAG compositions as a function of time.

4.3.5.1 Bacterial growth on BAG surface

Biofilm growth was tested on sintered BAG pellets incubated together with bacteria. A clear difference was observed between the different BAG compositions (Figure 55). A strong antibacterial activity was shown by the 53S and 58S4Sr BAG compositions, where the effect was more pronounced for S. *epidermidis*. For S. *aureus* the amount of viable CFU on BAG 53S and 58S4Sr slowly grew with incubation time and was lower for BAG containing Sr. In contrast, the amount of CFU of S. *epidermidis* for BAG 70S remained almost the same and that of S. *aureus* was even drastically lowered over time. After 120 hours the viable cells on 70S reached the same value as 53S. The highest number of CFU was measured on BAG 58S4Zn.

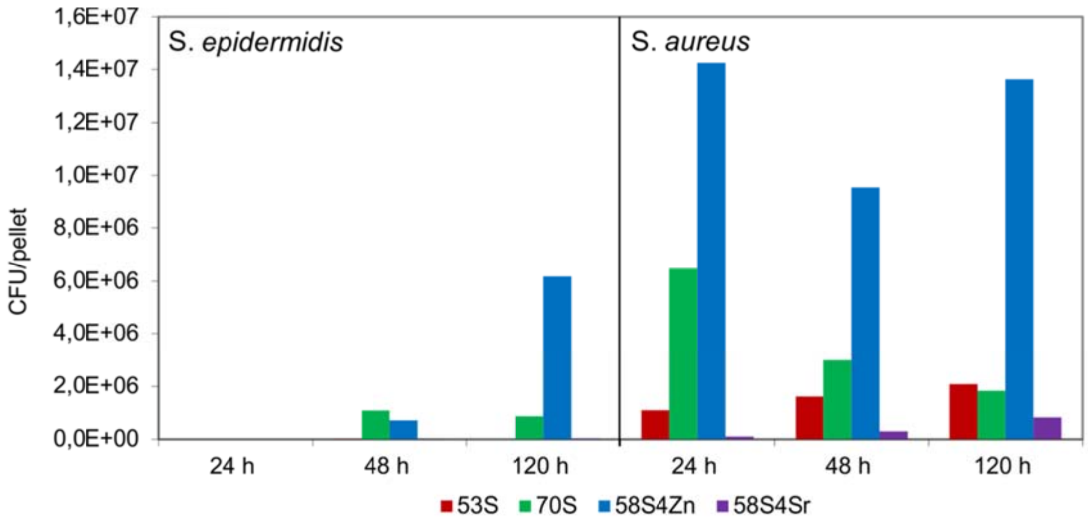

Figure 55: Staphylococcal biofilm evaluation on sintered BAG pellets. Comparison of viable S. *epidermidis* and S. *aureus* CFU recovered from different BAG compositions as a function of time.

The biofilm formation was qualitatively evaluated by SEM observations. For BAG 70S only a few separated S. *epidermidis* bacteria were found on its surface. In contrast, a lot of S. *aureus* were attached to its surface. A biofilm was observed already after the first day (Figure 56a). After 48 hours the amount of bacteria adhering to the surface was reduced (Figure 56b) but the biofilm formation was again found on the surface after 120 hours. In Figure 56d, showing a biofilm at higher magnification, the formation of extracellular polymeric matrix (ECM) bonding together bacteria, can already be seen.

Figure 57 shows the surface of BAG 53S before (a) and after incubation with S. *epidermidis* (b, c) and S. *aureus* (d, e, f). No bacteria were found on the surface of sintered BAG, however another important feature was observed. After soaking in tryptonic soya broth (TSB - bacteria culture broth), BAG 53S started to dissolve which is shown as micrometre-sized pores formed on its surface (Figure 57 b, d). After 120 hours of incubation BAG surface became covered with spheres, strongly resembling hydroxyapatite that is formed when BAG is soaked in simulated body fluid.

Bioactive glasses doped with ZnO and SrO showed a completely different effect on the bacteria. While there were biofilms formed on BAG 58S4Zn already after 24 h for both S. *epidermidis* (Figure 58a, larger bacteria aggregates are marked with red) and S. *aureus* (Figure 58b, c), BAG 58S4Sr strongly inhibited bacteria growth, as there were no bacteria found on the surface of any of these samples.

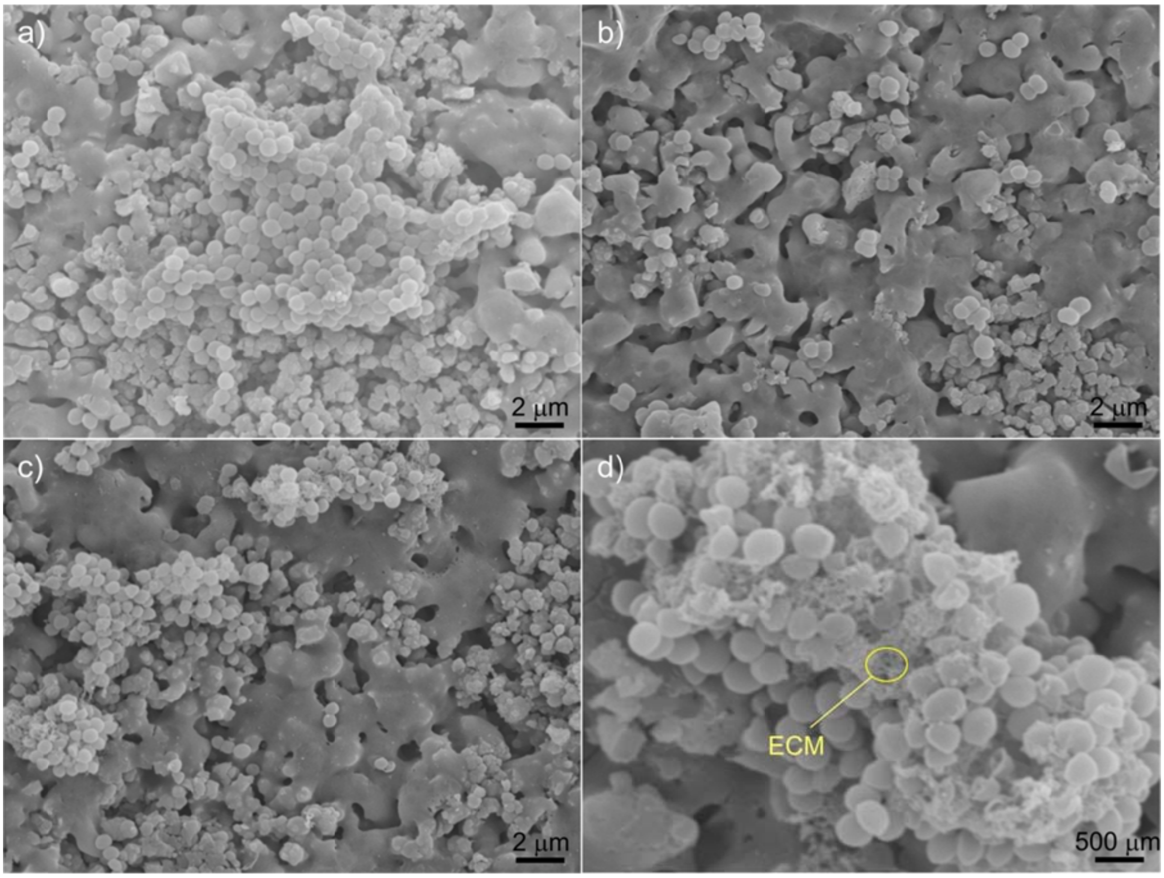

Figure 56: Biofilm formation on BAG 70S. S. *aureus* bacteria on the surface of BAG after (a) 24 h, (b) 48 h, (c) 120 h and (d) higher magnification of bacteria in a biofilm.

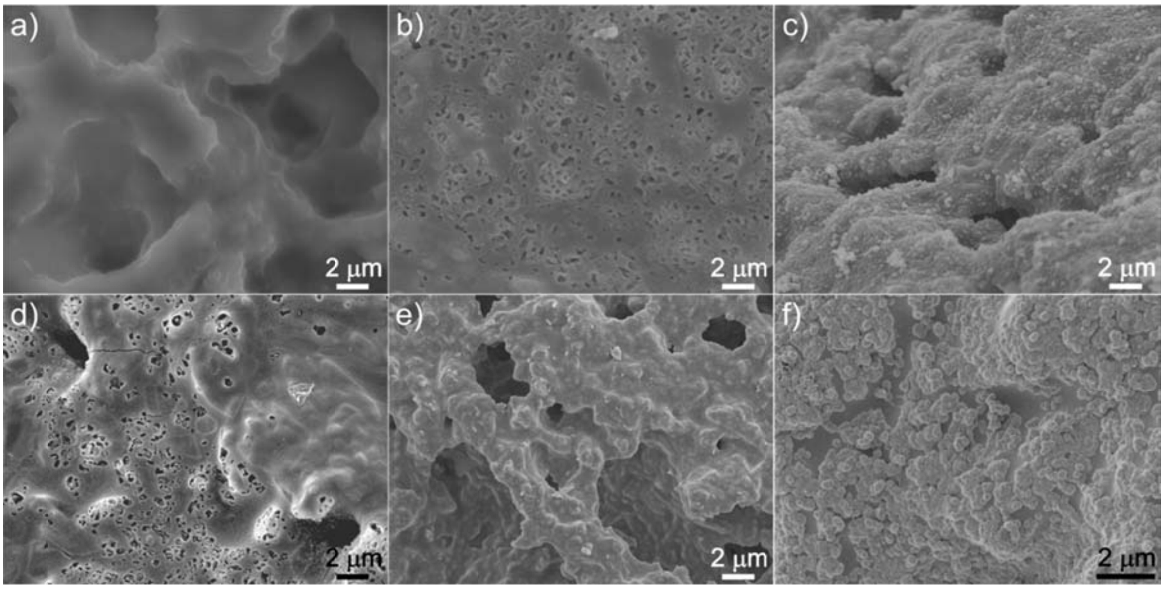

Figure 57: Antibacterial effect of BAG 53S. Surface of the BAG (a) before soaking and after incubation with S. *epidermidis* for (b) 24 and (c) 48 hours. Surface of the BAG after incubation with S. *aureus* for (d) 24, (e) 48 and (f) 120 hours.

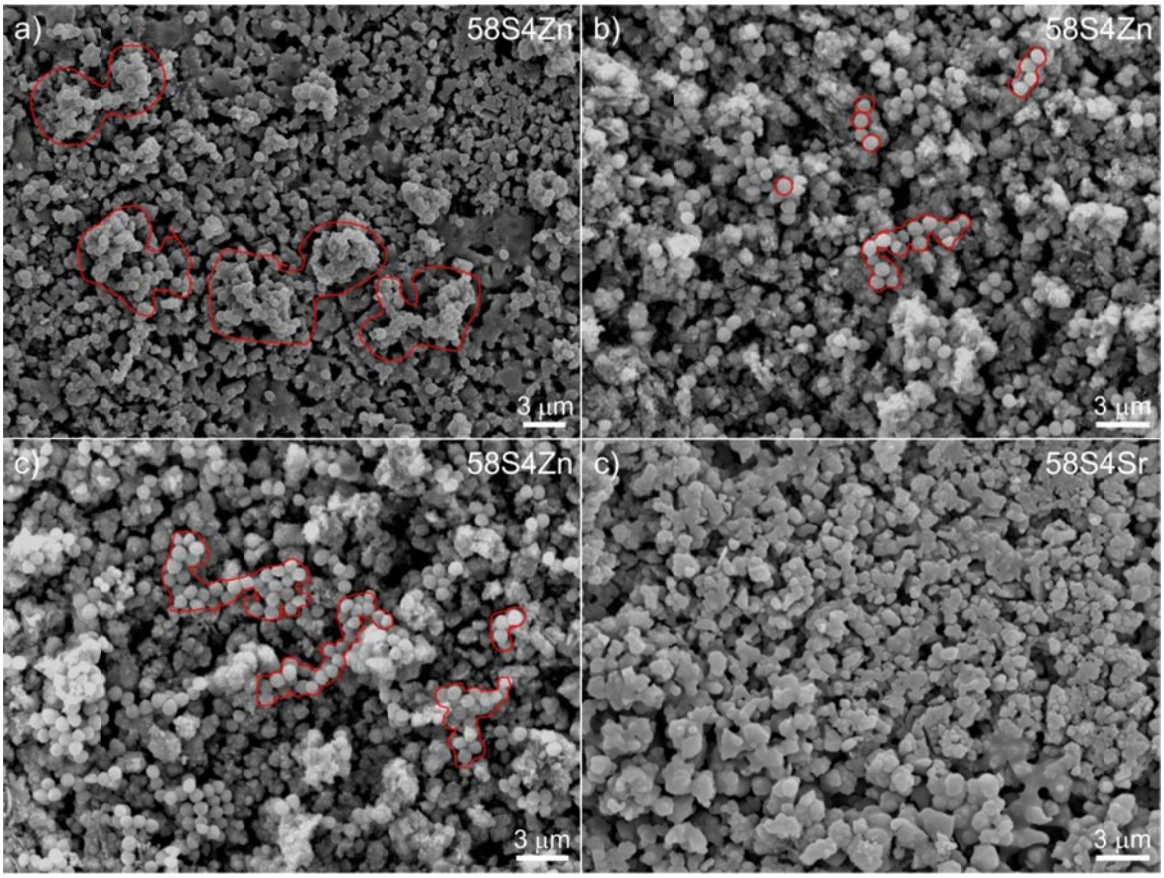

Figure 58: Biofilm formation on BAG 58S4Zn and biofilm inhibition of BAG 58S4Sr. (a) S. *epidermidis* biofilm after 24 hours; (b) S. *aureus* after 24 and (c) 120 hours. (d) Surface of BAG 58S4Sr after 120 hours incubation with S. *aureus*.

4.3.6 BAG coatings

Finally, the BAG powder of selected compositions was applied on a flat Ti6Al4V alloy surface or infiltrated into the porous Ti layer on a Ti6Al4V sample.

4.3.6.1 BAG coatings on flat surfaces

BAG coatings were applied on flat surfaces in order to analyse the interface between the BAG and the Ti-alloy as well as between the BAG and the hydrothermally applied TiO_2 coating. Instead of a porous surface that was used for *in vivo* tests, a flat surface was used to simplify the process for TEM sample preparation. Namely, coatings on porous surfaces would be difficult to prepare and analyse.

BAG was applied on the surface of flat Ti6Al4V discs by electrophoretic deposition from an ethanol suspension. As described in previous sections, sol-gel synthesis resulted in agglomerated BAG powders. The size of the agglomerates after calcination was more than 10 µm and the powders dispersed in ethanol suspension were not stable, the zeta-potential was low (Figure 59). Ethanol was used to prevent BAG dissolution, which occurs in water suspensions. Such an unstable suspension was not suitable for coatings, therefore BAG powders had to be de-agglomerated. De-agglomeration was achieved by the addition of the deflocculant polyethylene imine (PEI 1800). The particle size after the addition of PEI was lowered to about 1 µm (Table 15). The increase in ZP by PEI addition is presented in Figure 59.

Table 15: Particle size of BAG prepared by different methods and with different compositions

Synthesis method	BAG	d_{50} (µm)
particulate sol-gel/microwave/PEI	53S	0,8
particulate sol-gel/microwave/PEI	70S	1,3
particulate sol-gel/microwave/PEI	58S4Zn	0,7

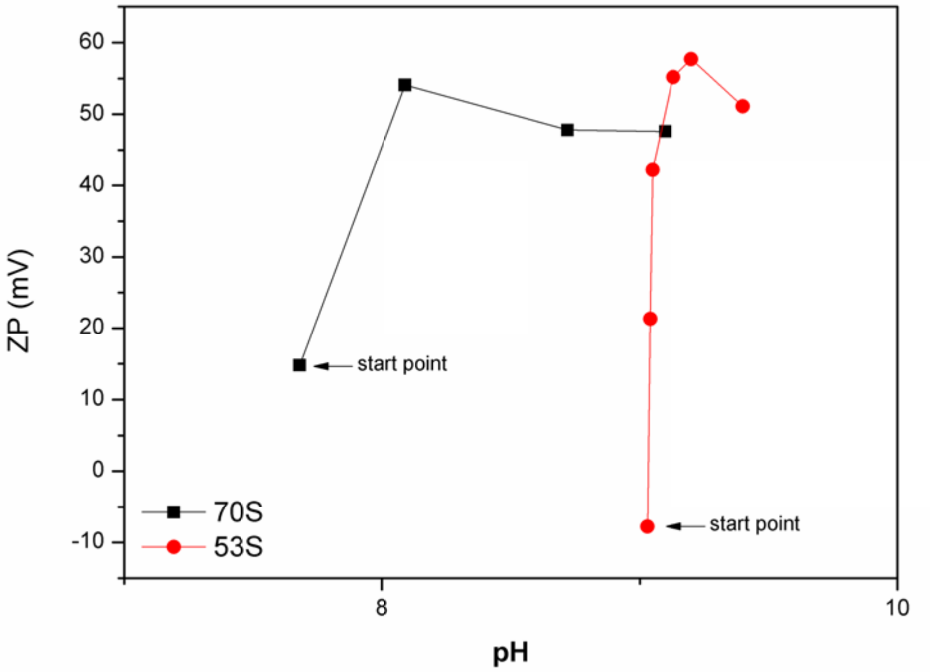

Figure 59: Dependence of ZP of BAGs on the PEI addition. Amount of PEI in the start point is 0 %, for each further measurement 0.2 % of PEI according to the mass of BAG was added.

For EPD 4 wt.% of BAG in an ethanol suspension was used. The Ti-alloy served as the negative electrode on which positively charged BAG was deposited. Coatings were applied at 10 V for 1 min. A BAG coating on a flat Ti-alloy is presented in Figure 60. After deposition, the coatings were dried in air and sintered in a vacuum furnace, to avoid oxidation of the Ti-alloy, at temperatures determined by dilatometry experiments, i.e., 810 °C for BAG 53S and 850 °C for BAG 70S. Further characterization of the BAG coatings on Ti-alloy or TiO_2 coating is described in section 4.3.7.

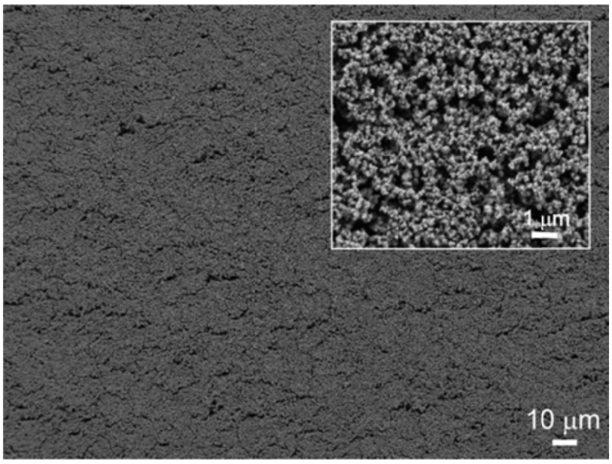

Figure 60: Green BAG coating deposited by EPD on Ti-alloy.

4.3.6.2 BAG coatings on porous surfaces

The BAG coatings in this study that were used for *in vivo* tests were prepared on Ti6Al4V substrates with a porous Ti layer. Therefore, BAGs were applied to the porous Ti-layer by vacuum infiltration. As for the previously described EPD, a stable ethanol suspension had to be prepared for vacuum infiltration. BAG particles had to be de-agglomerated to be able to obtain a small enough particle size to coat the smallest of the pores in the porous Ti layer implant (see Figure 8).

After vacuum infiltration the samples were sintered at temperatures determined from dilatometry, 810 °C for BAG 53S, under vacuum to avoid oxidation of the Ti-alloy substrate. Cross-sections of the implant with BAG-infiltrated porous Ti-layer are presented in Figure 61a and b (different magnifications). In the optical micrograph (Figure 61a) the bioactive glass appears as a light phase within the porous titanium layer (dark phase) on the bulk T6Al4V substrate (dark phase in the lower part of the image). It is obvious that the bioactive glass has impregnated the porous titanium layer throughout the whole thickness of layer. Conversely, in the SEM image (Figure 61b) the metal is white, while the bioactive glass appears as a grey porous phase with a few micrometres large partially sintered particles. The BAG is also found in very small pores.

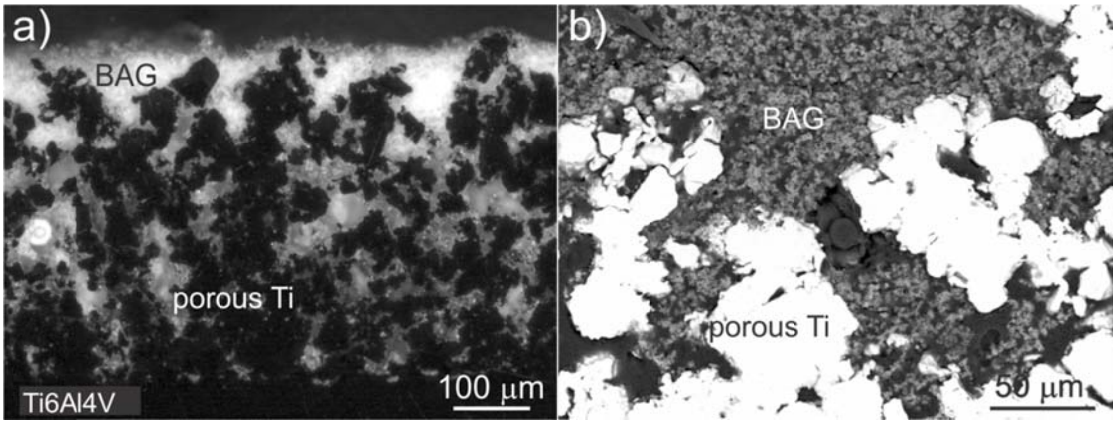

Figure 61: (a) Optical micrograph (polarized light) of polished cross-section of the Ti6Al4V implant with porous titanium layer impregnated with bioactive glass. (b) SEM micrograph at higher magnification.

4.3.7 TiO_2/BAG coatings

To verify the interaction of BAG with the substrate material and possible interaction of the TiO_2 interlayer on the composition and structure after sintering on Ti6Al4V, the cross-sections of the coating were examined by TEM. For easier handling and examination the coatings were prepared on flat substrates. A cross-section of the BAG 53S coating is presented in the optical micrograph and SEM image in Figure 62.

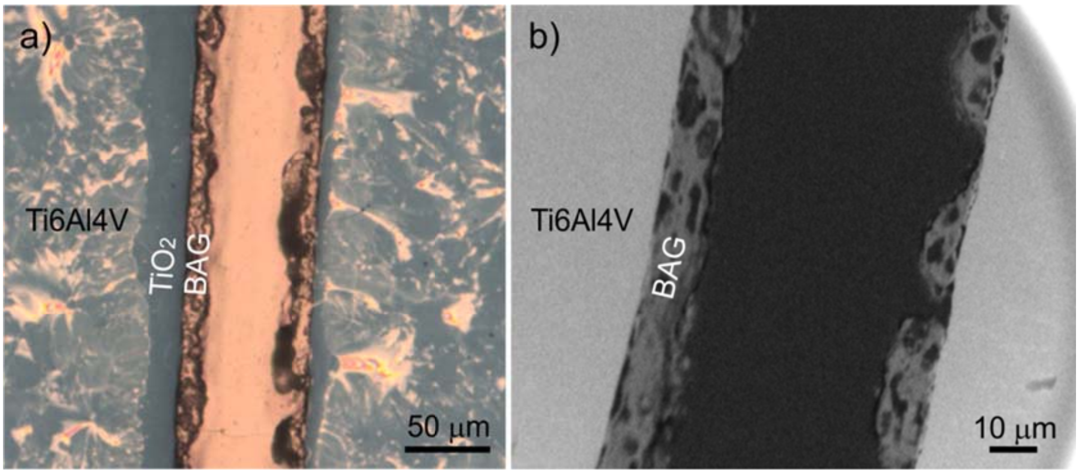

Figure 62: Cross-section of BAG 53S coating on Ti6Al4V; (a) optical micrograph and (b) SEM image.

Sintering of BAG on Ti6Al4V substrate resulted in the formation of an intermediate reaction layer between the substrate and the BAG. In the case of BAG in direct contact with the alloy the interlayer was ~ 1 µm thick (Figure 63 b and c), whereas it was much thicker, 3 µm, when a titania layer was formed with hydrothermal treatment (HT D3) before the BAG deposition (Figure 63a). This interlayer was composed of Ti as well as Si ions, seen in EDS mapping below each TEM image for different coating in Figure 63. In the upper BAG layer only Si and Ca was detected and in the substrate only Ti can be seen.

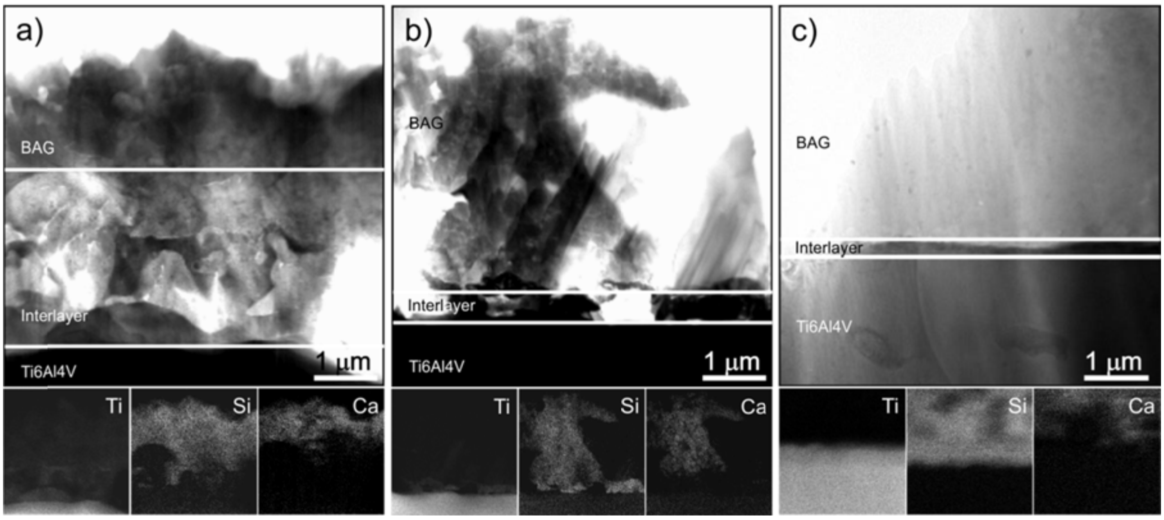

Figure 63: TEM images of BAG coatings on Ti6Al4V substrate. (a) BAG 70S on TiO_2 coated Ti6Al4V, (b) BAG 70S on Ti6Al4V without TiO_2 layer and (c) BAG 53S on Ti6Al4V substrate without TiO_2 layer with Ti, Si and Ca EDS maps.

More detailed analyses of the reaction layer and the BAG phase are presented below in Figs. 63, 64 and 65.

Results of the quantitative EDX analyses of different layers of cross-section for the sample coated with BAG 70S without TiO_2 coating (Figure 64) were 60–80 at.% SiO_2, 10–35 at.% CaO, matching with the BAG 70S composition. About 5–10 at.% of TiO_2 was also present in the glass region. The 1 µm interlayer was composed of 28–35 at.% of Si and 72–65 at.% of Ti, corresponding to Ti_xSi_y. In the substrate only elements found in Ti6Al4V alloy were detected; 93 at.% Ti, 5.4 at.% Al and 1.6 at.% of V. In the glass phase two regions were analysed: a region away from the substrate at the top of the BAG coating, marked with a rectangle A, and a region closer to the substrate and reaction layer, marked with a rectangle B. Both regions were found to be crystalline (diffraction pattern A and B in Figure 64) with a large amount of Ti in the region closer to the substrate and a smaller amount in the region away from the substrate.

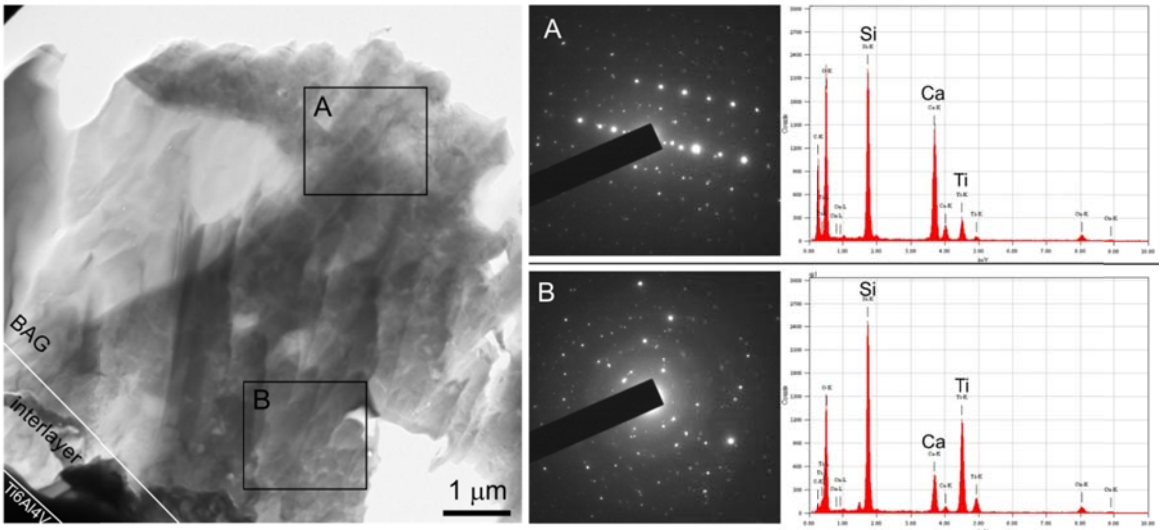

Figure 64: TEM image of BAG 70S coating on Ti6Al4V substrate without TiO_2 layer (left) and diffraction patterns for upper (A) and lower (B) BAG coating with corresponding EDS spectra.

The quantitative EDS analyses of the different layers in the cross-section for the sample coated with both TiO_2 and BAG 70S (Figure 65), with a 3µm-thick-reaction layer, showed that the composition of the coating next to the substrate contains mostly elements from the substrate alloy together with a small amount of Si and Ca. No oxygen is detected in this region. Further away from the substrate, still in the region marked as interlayer, the Ca and Si content is increasing and oxygen is still not present, however more C is also detected. The reaction layer has about 25 at.% of Si and 75 at.% of Ti, showing during the formation of silicides (Ti_xSi_y, $Ti_xSi_yC_z$). The glass region contains together with oxygen a lot of Si, increasing the amount of Ca and also a lot of Ti (50–70 at.% of SiO_2, 20–30 at.% of CaO and 10–20 at.% of TiO_2). The amount of Ti is higher compared to the sample coated just with BAG and without TiO_2. A diffraction pattern taken in the glass and reaction zone region, marked with squares A and B, respectively, showed that the glass phase is preferentially amorphous (Figure 65b with a diffraction pattern A), whereas the reaction layer is composed of nanocrystallites (Figure 65c with a diffraction pattern B) that are 2–5 nm big (Figure 65d) and are surrounded by an amorphous matrix. The d values of the ring in the diffraction pattern belongs to titanium silicides (Ti_5Si_4,

Ti_5Si_3, TiSi). Measured and experimental d values are presented in Table 16.

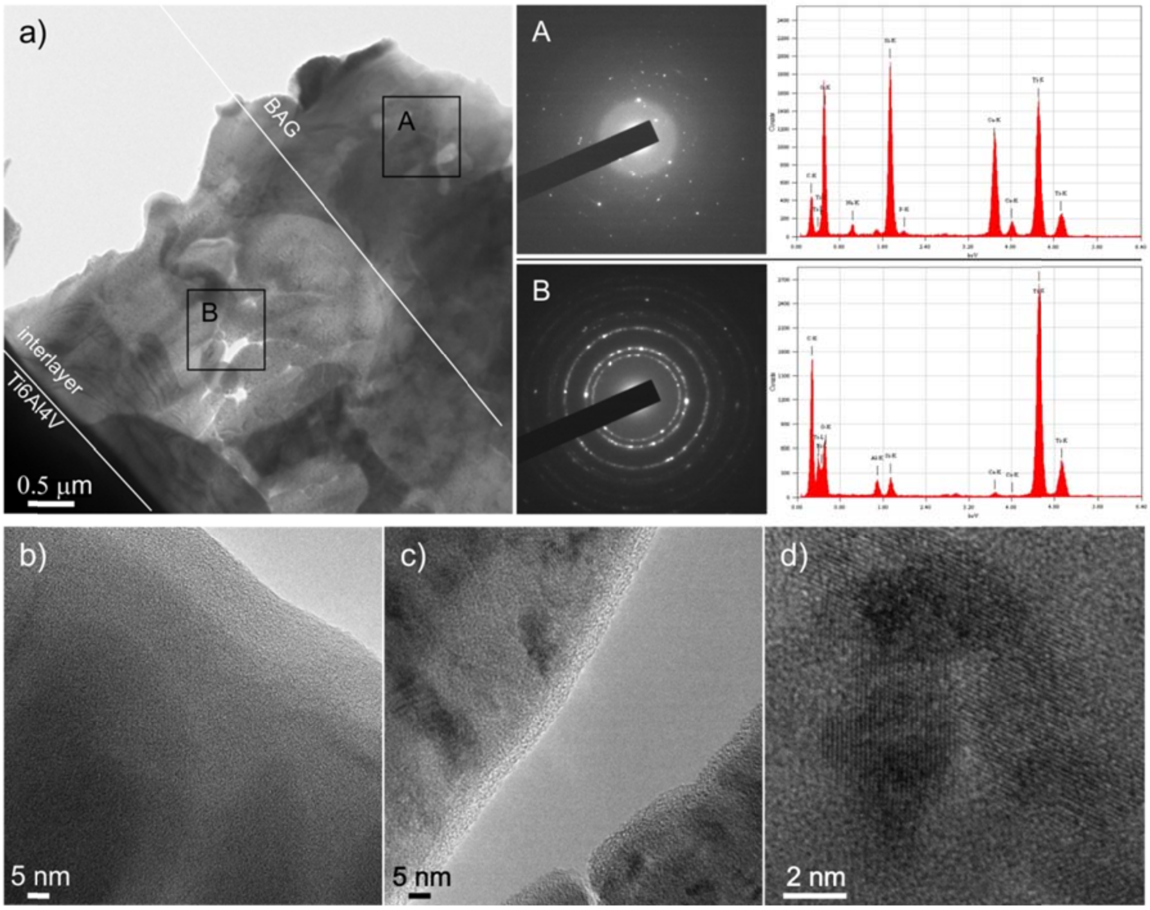

Figure 65: (a) TEM image of BAG 70S coating on TiO_2 coated Ti6Al4V substrate (left) and diffraction patterns for A and B region (A-glass coating, B-interlayer) with corresponding EDS spectra; (b) TEM image of region A; (c, d) TEM image of region B.

Table 16: Measured d values of diffraction rings in the interlayer diffraction pattern compared to experimental values of Ti_xSi_y.

		Ti_5Si_3		Ti_5Si_4		TiSi	
diff.	$d_{meas.}$ (Å)	$d_{exp.}$ (Å)	{hkl}	$d_{exp.}$ (Å)	{hkl}	$d_{exp.}$ (Å)	{hkl}
1	2.46	2.436	210	2.413	213	2.435	210
2	2.12	2.116	112	2.123	310	2.189	211
3	1.51	1.508	222	1.511	413	1.515	221
4	1.30	1.286	004	1.300	119	1.323	303
5	1.05					1.045	610

Similar results were also obtained with a different BAG composition, BAG 53S. The BAG was applied directly on the Ti6Al4V alloy without any TiO_2 coating. The intermediate reaction layer between the BAG and Ti-alloy was composed of titanium silicides (25 at.% Si and 75 at.% Ti). The BAG layer composition was 60–70 at.% SiO_2, 10–20 at.% CaO, 5 at.% P_2O_5 and 5–10 at.% Na_2O. Some 5–10 at.% TiO_2 was also detected in this layer. The BAG layer was found to be partially crystalline. Around 50–150 nm large crystallites (marked with A in Figure 66) were embedded in a glassy matrix (marked with B in Figure 66). The EDS spectra in Figure 66 showed that the glass phase contained more Ti than the crystalline phase (marked with A in Figure 66). The crystallites had a lower amount of Ca and were mainly composed of SiO_2.

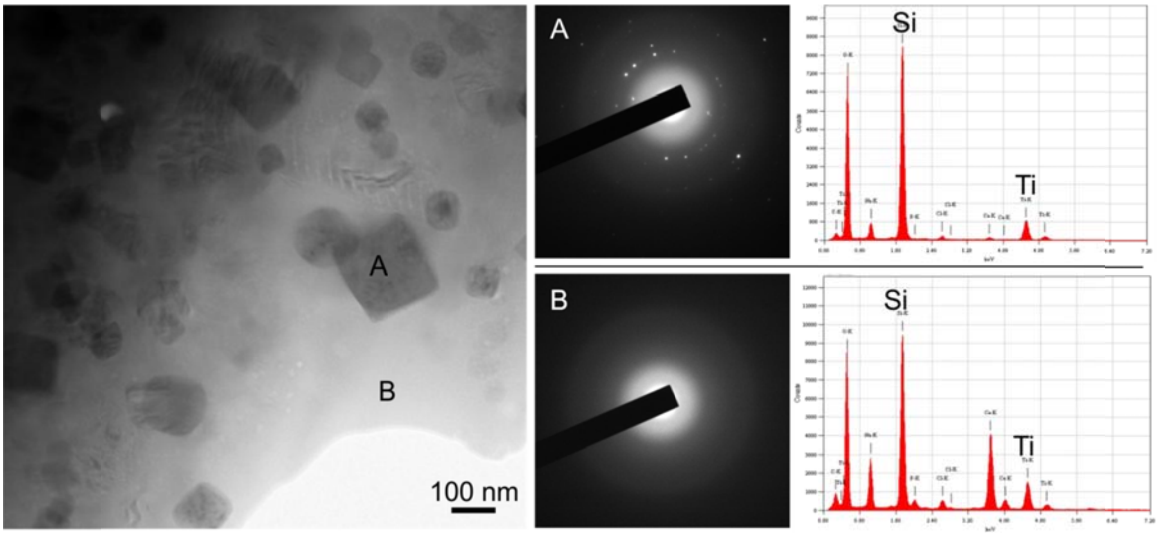

Figure 66: TEM image of BAG 66S coating on Ti6Al4V substrate without TiO_2 layer (left) and diffraction patterns for (A) crystallites and (B) glass phase, with corresponding EDS spectra.

4.3.8 *In vivo* tests

On the basis of the presented results, we decided to modify the composition of the BAG to be tested *in vivo*. This way the number of animals was minimised. Instead of using two BAG compositions, 53S and 70S, we lowered the amount of Na (only 10 wt.%) in 53S and thus lowered the possible pH effect on cells and still keep the good bioactivity. The new BAG composition was 66S (in wt.% $66SiO_2$-$20CaO$-$10Na_2O$-$4P_2O_5$).

Finally, samples of Ti6Al4V cylinders with a porous Ti-layer were implanted into the rabbit tibia to examine the response of the tissue on the BAG and to compare the osseointegration of BAG infiltrated porous layer implants with non-coated implants. After 10 weeks the rabbits were sacrificed and samples were prepared for histological and SEM observation.

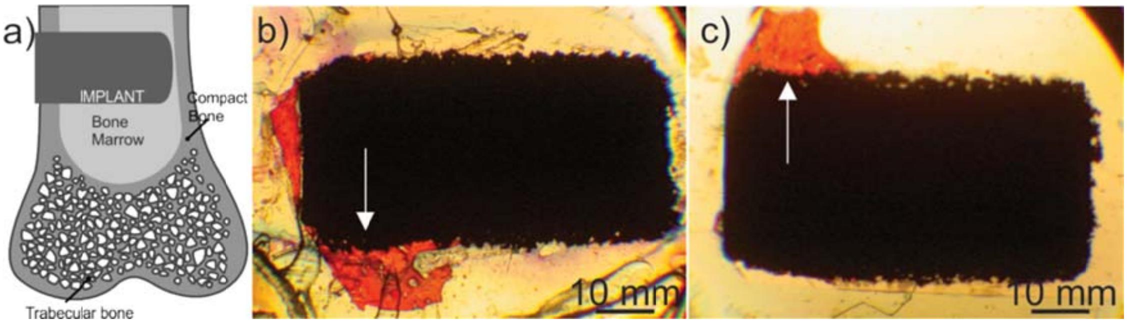

Figure 67: (a) Schematic presentation of the implant position in the bone tibia. (b) Macroscopic images of the histological preparations of samples with BAG coating, and (c) without BAG. The arrows show the area of interest (the part of the implant in contact with compact bone). The mineralized bone is stained red and the implant is black.

Figure 67a illustrates the position of the implants in the rabbit tibia: only a small part of the 6-mm-long cylinder (<2 mm) was fixed in the compact bone, while the rest extended into the bone marrow. Some of the implants were in good contact with bone only on one side. The bone overgrew the outer part of the implant fixed in compact bone, and further expanded on the part positioned in the bone marrow. The area of interest was within this 2 mm of the bone-implant interface, as indicated by arrows in Figure 67b and c.

Figures 68a and b represents characteristic areas of the polished cross-sections of the samples with or without BAG. In both cases, the bone has grown over the metal as well as into the pores of the titanium layer. However, there is a clear difference in the depth of bone growth within the porous titanium layer: the bone overgrew the whole porous area of the samples with BAG within the pores (Figure 68a), while in the case of the samples without BAG, only the outer part of the porous layer is occupied with the newly formed bone (Figure 68b). In addition, in both types of samples relatively good bone-to-implant contact can be observed. A comparison between the porous titanium layer and flat Ti-alloy surface can be seen in Figure 68c. On the flat side of the implant, a large gap between the implant and the bone was formed that indicates that bone-to-implant contact is much worse for flat than for the rough surfaces.

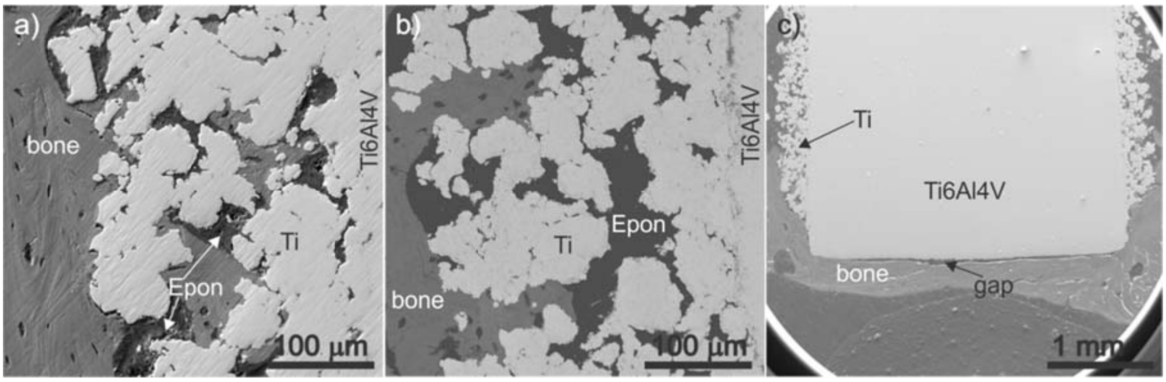

Figure 68: Scanning electron micrographs of polished cross-section of the sample (a) with BAG, and (b) without BAG. (c) Lower magnification image of the BAG-containing sample with and without porous titanium layer.

The presence of bone in the porous titanium layer was confirmed by EDS analysis of the polished cross-sections of the explanted implants. The atomic ratio of the calcium-to-phosphorus content was determined to be close to 1.7, which corresponds to the natural mineral phase of the bone. i.e., hydroxyapatite. Distribution of elements within the porous titanium layers with or without the BAG is illustrated in Figure 69a and b, respectively. The light dots indicate areas with a higher concentration of an analysed element. The implant material is identified with a high content of Ti, the C-rich areas confirm the presence of Epon resin in which the samples were mounted, while high calcium and phosphorus concentrations in the ratio of ~1.7 indicate the presence of mineralized bone. Si distribution revealed whether some BAG remained in the pores.

As can be seen in Figure 69a and b, Ca and P can be detected much deeper in the porous region of the BAG-containing samples compared to samples without BAG. For the latter, the high carbon content and absence of Ca and P in the deeper region of the Ti-layer confirm that the bone did not fill the pores close to the substrate;

instead, they were filled with Epon. The minor presence of Si in the sample with BAG indicates that the BAG has dissolved during ten weeks of implantation. The small amount of Si was also detected in the sample without BAG, therefore in both samples, Si presence could be the consequence of grinding with SiC grinding papers. This proves that, in the early stage, the BAG gradually dissolves, providing the necessary concentrations of ions for promoting the bone formation.

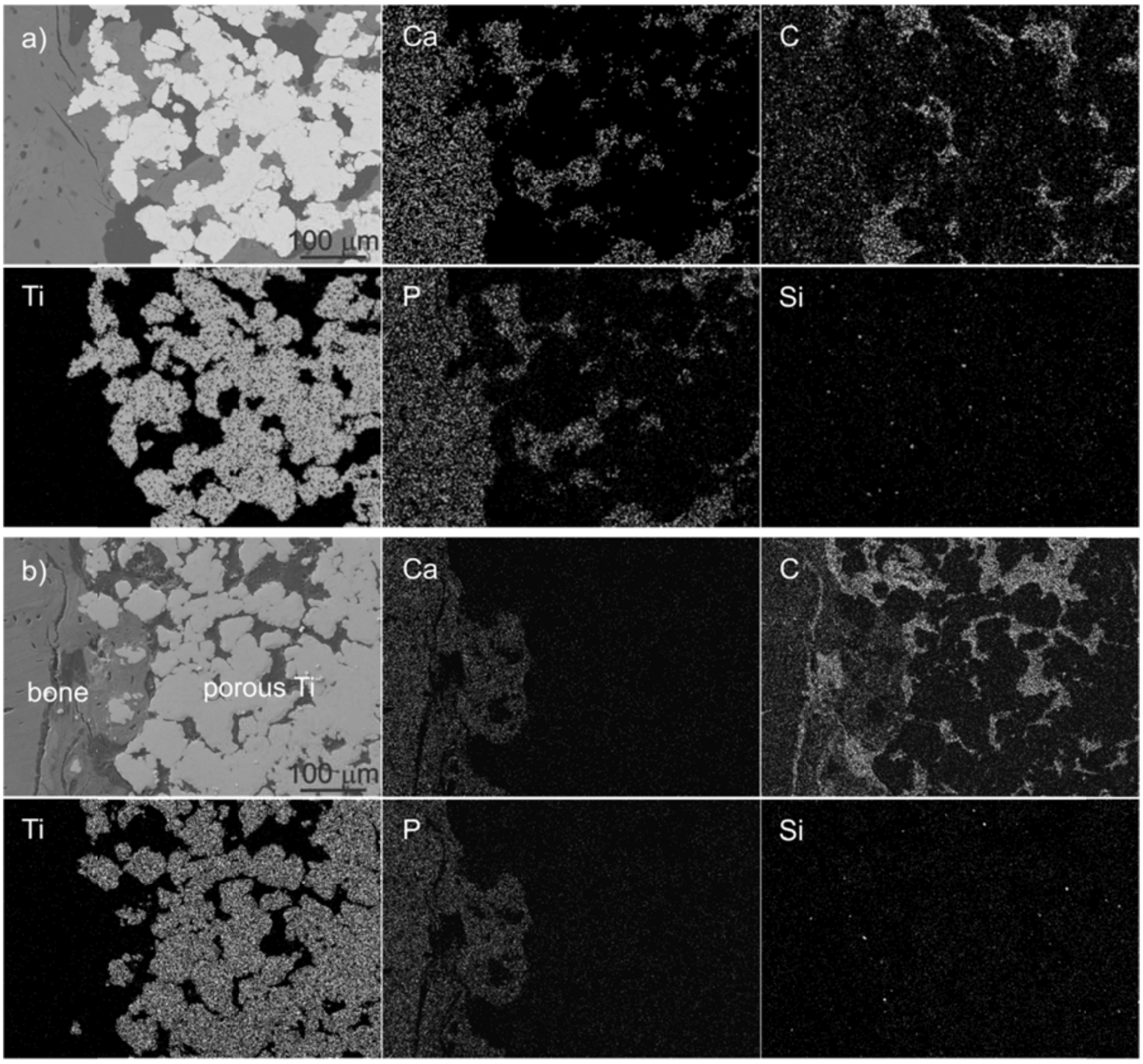

Figure 69: (a) EDS mappings of bone implant cross-sections for the sample with BAG, showing from left to right on top: SEM image, Ca, C; bottom: Ti, P, Si. (b) EDS mappings of the sample without BAG, showing from left to right on top: SEM image, Ca, C; bottom: Ti, P, Si.

The bone-to-implant contact and the bone ingrowth were also evaluated quantitatively. The analyses were performed on the part of implant that was in contact with the compact bone. The part of the implant that was in the bone marrow was excluded, although in the case of samples with BAG, the mineralized bone was also found in the porous region of the implant extending in the bone marrow. The bone-to-implant contact for the samples with and without BAG was equal, around 52 %. A much more beneficial effect of BAG was observed in the bone occupation of the pores. The pores of the samples with BAG were 38 % filled with bone, while significantly lower amount (p<0.05) of the pores without BAG were filled with bone, only 22 %.

Histological examinations of the stained slices were focused on the appearance of mineralized newly formed bone in pores and in contact with metal. Ten weeks after implantation, all the implants, with and without BAG, showed no sign of inflammation at the interface with the implant (Figure 70a and b). More mineralized bone (red) was observed in the pores of the samples prepared with BAG, where the bone also grew downwards on the implant surface into the bone-marrow region (see Figure 70c). Newly formed bone in the samples with BAG was also found in the porous regions of the implant that was away from the original compact bone and was actually lying in the medullary cavity of the tibia and surrounded by the bone marrow (Figure 70d). As the whole porous titanium layer of the implant was initially filled with BAG, bone formation was accelerated not just in the site of the implant facing compact bone, but also on the site of the implant facing bone marrow. In both kinds of implants, i.e., with or without BAG, the contact between the implant and the newly formed compact bone was similar, i.e., good contact with only a few gaps filled with adipose tissue.

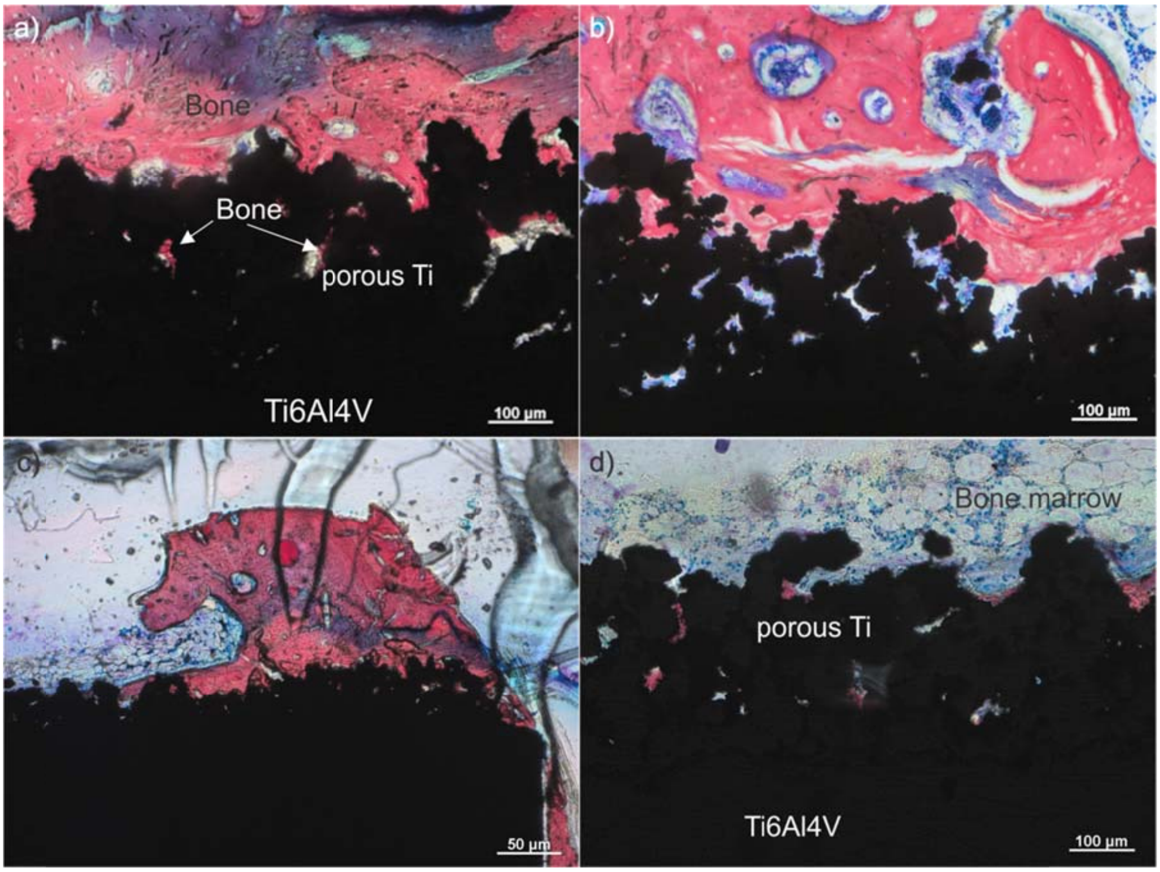

Figure 70: Characteristic histological sections of the samples (a) with BAG, and (b) without BAG. (c) Sample with BAG at lower magnification, and (d) part of the implant in the bone marrow. Mineralized bone is stained red. Osteoblasts and bone marrow cells in b are stained blue. The blue region in the upper part of the image (a) is an artefact caused during the staining with Stevenel's blue.

5 Discussion

5.1 TiO_2 coatings

5.1.1 Surface morphology of the HT-treated Ti6Al4V samples

Hydrothermal treatments started with experiments where the treatments were performed without the addition of Ti^{4+} ions (Ti^{4+} complex). In this case, it was not possible to obtain dense coatings, their thickness also never exceeded the crystal size. In contrast to literature reports, where the HT treatment is performed in order to crystallize the amorphous titania coating that is previously applied by some other method, e.g., chemical treatment, we used as a seed layer for further crystal growth only the natural titania layer that is always present on the surface of the Ti alloy. The treatment without Ti^{4+} resulted in a non-uniformly coated surface. However, it showed that the most nicely developed crystals with pinacoidal morphology were developed by the addition of NaOH. Similar to our experiment, Wong et al. also obtained a thickness of only a few tens of nm when they HT treated a NiTi alloy in water[46], however the coating in their study was composed of 10-nm-large grains, whereas in our study anatase crystals were up to 100 nm. A thicker coating was achieved when HT treatment was performed in water solution containing Ti^{4+} ions, by Cheng et al.[43]. Like in this study, when Ti ions were added into the solution all the coatings were denser, but also the crystal size was reduced. In contrast to Cheng et al. [43], Ti^{4+} ions in this study were simply added in the form of TiO_2 powder or $Ti(OH)_4$, where Cheng et al. dissolved the powder prior to the treatment to obtain a solution of Ti^{4+} ions. Moreover, their HT treatment had to be performed at two different temperatures to achieve both nucleation and crystallization, which was not the case in our study.

The formation of a film on Ti alloy substrates is described by the dissolution and re-precipitation of TiO_2 and also Ti in the substrate alloy[139]. Under alkaline conditions Ti and TiO_2 dissolves and re-precipitates in the following mechanisms[139]:

- $Ti + 4H_2O \rightarrow Ti(OH)_3^+ + OH^- + 2H_2$
  $TiO_2 + 2H_2O \rightarrow Ti(OH)_3^+ + OH^-$
- Precipitation: $Ti(OH)_3^+ + OH^- \rightarrow TiO_2 + H_2O$

As both reactions occur during the hydrothermal treatment it is possible to dissolve TiO_2 in the suspension as well as amorphous TiO_2 that is always present on the surface, and precipitate them again on the surface of the alloy where nuclei are formed by heterogeneous nucleation. But as described above, the dissolution and re-precipitation of the naturally formed titania layer was not enough to form dense crystalline coatings.

The addition of Ti^{4+} ions resulted in more homogeneous coatings, but there were also other factors that were influencing the crystal size and morphology.

Temperature influenced the density of the coating. When the temperature was increased from 150 to 200 °C coatings became denser as the solubility of the TiO_2 was greater, and therefore more Ti^{4+} ions were available for precipitation on the Ti-alloy substrate. The influence of temperature can be seen for the HT treatment in the TiO_2 suspension with the addition of NaOH (Figure 12) and with the addition of TMAH (Figure 13b compared to d). By increasing the temperature the ratio between dissolution and precipitation rate is changing. Both are increasing with temperature. However, when the solubility is lower (at lower T) the precipitation rate is higher than the solubility[139], which according to Divya Rami et al. results in more bipyramidal, elongated anatase crystals in their c-direction[139]. This was also observed in our HT treatments at 150 °C in NaOH were needle-like anatase particles were formed (Figure 12a, b compared to c and d) and in HT with TMAH, but only for the lowest TiO_2 concentration. The effect of temperature was also seen by Wong et al., who for the HT treatment of NiTi samples in water by raising the temperature from 120 to 180 °C increased the density and the thickness of the film from 5 to 56 nm[140].

The increase of pH in TiO_2 suspensions also helped to produce coatings with a greater amount of crystals compared to the treatment at lower pH due to the greater amount of Ti^{4+} ions available at higher pH. The pH influence can be seen in Figure 12a compared to b.

The effect of the concentration of Ti^{4+} ions is clearly seen also for the treatment in $Ti(OH)_4$ suspensions. There were many more available Ti^{4+} ions in the $Ti(OH)_4$ suspension than in the TiO_2 suspension, even though the starting concentration was calculated to be 5 wt.% for both, but the solubility under the hydrothermal conditions was much greater for the $Ti(OH)_4$ powder (Figure 14a compared to Figure 16a). The effect is similar to the one seen in Figure 13c, where the concentration of TiO_2 suspension was raised to 30 wt.%. As there was too much material available for growth the faceted crystals could not be formed. The addition of citrate helped to form anatase crystal facets, but 0.5 wt.% seemed not enough (like it was for TiO_2 suspensions) as the concentration of soluble Ti^{4+} ions was greater. Increasing the citrate concentration did not help to gain the desired morphology. Moreover, anatase was forming unusual anatase shapes due to non-equilibrium conditions, which were described to form from Ti-isopropoxide as a starting precursor by Horvat et al[127].

The addition of NaOH and TMAH was used for raising the pH and thus making conditions favourable for anatase formation, as it is reported elsewhere[141]. NaOH was added to obtain the desired pH for anatase crystals, as well as TMAH, by which besides pH, an increase in solubility was also achieved. The increase in solubility was not promoted just by the pH, but also by the TMAH itself. When TMAH instead of NaOH was used at the same pH, a greater amount of particles and smaller particles were formed (see Figure 12 and Figure 13). Dong et al. [142] explained how TMAH helped to provide Ti^{4+} ions: it reacts with the titanium, forming tetramethylammonium titanate, which then decomposes during the hydrothermal treatment, providing free titanium ions. TMAH thus helps to produce more free Ti^{4+} ions for crystal growth and in particular it seems to help the nucleation, as the coatings with TMAH are denser (see Figure 13).

With the addition of ammonium citrate, anatase with larger {001} facets was formed. The growth of **{**001} facets was also enabled with the addition of citric acid. However, this only happened when the amount of NaOH and TMAH was increased compared to other treatments, due to the acidic nature of the citric acid, which reduce the pH of the suspension to low values (pH ∼ 2). In order to increase the pH to values appropriate for anatase conditions, an additional concentration of NaOH and TMAH had to be added. This resulted in surfaces coated mostly with spherical particles and with some plate-like (with large {001} facets) anatase particles grown in the grooves of the substrate. The formation of amorphous-like particles can be explained by the high concentration of TMAH that increases the solubility and nucleation, but does not form well-crystallised anatase shapes, as seen in Figure 13d. It is also possible that a few plate-like anatase crystals were formed by the same help of TMAH, as it was reported that TMAH (TMA^+ groups) can selectively adsorb to the (001) planes through hydrogen bonding, which is also the case for amine groups[142, 143]. Thus the addition of TMAH should also help to form truncated bipyramidal anatase crystals. Although citrate ions are widely used in the HT synthesis of ZnO for the reduction of growth of ZnO {001} planes[144] this is not the case with TiO_2. The surface of TiO_2 in pH values that were used in this study, pH 10 or 12, is highly negative, therefore the inhibition of growth of the {001} facets in the HT treatment with the addition of ammonium citrate was caused by the adsorption of positive ammonium groups. The statement is further supported by the formation of a truncated bipyramidal crystal with the HT treatment in acidic conditions where NH_4NO_3 was used (see Figure 11a). The pH value during that treatment was 5 and according to the ZP measurements the surface of TiO_2 in these conditions is still negatively charged. Therefore, the NH_4^+ groups were also able to bond to the {001} crystal planes and thus reduce their growth rate. However, the treatment in acidic conditions was not further used due to the thickness rarely exceeding the crystal size and presence of TiO_2 crystals with an unknown morphology.

5.1.2 Characteristics of TiO_2 coating

A strongly adhered TiO_2 coating, with an adhesion shear strength of more than the required 22 MPa, showed improvements in many areas. The concentration of released ions, after one month of immersion in the physiological solution at 36.5 °C, was lower for the coated samples compared to the non-coated samples. The concentrations of titanium, aluminium, and vanadium were not in proportion to the original composition of the alloy; due to the higher solubility of aluminium and vanadium, more of these ions were released into solution from both the non-coated and coated samples compared to titanium. According to the leaching test with one month immersion time, the release of Ti and Al can be completely inhibited, while V is still released. However, with a simple leaching test in the physiological solution we cannot predict the *in vivo* situation, but we can still presume that the crystalline TiO_2 coating prepared by hydrothermal treatment, that is less soluble than natural amorphous TiO_2, reduces the amount of aluminium and vanadium as well as titanium to which the surrounding tissue is exposed.

The photocatalytic activity of the TiO_2 coating was proven by a simple qualitative test where the resazurin dye solution was discoloured and quantitatively by measuring the EPR signal. The EPR signal of the TiO_2 coated sample confirmed a significant photocatalytic activity compared to the Degussa powder P25 with known good photocatalytical properties. Although the powder has a much greater surface area than the TiO_2 coating on the disk, the EPR signal of the coating was increased 10-fold and the signal for TiO_2 P25 22-fold compared to the blank.

Besides photocatalytic activity the TiO_2 coatings induce a change in the wetting behaviour, which was even more pronounced when the samples were UV irradiated. This increased hydrophilicity of the TiO_2 coating can be assumed to have beneficial effects on bone-cell attachment. The change in the nature of metals, in this case the titanium alloy and titanium, from hydrophobic to hydrophilic, is especially important for porous titanium coatings in order to attract the cells into the pores. A lot of data in the literature relates to the strong antibacterial effect of the radicals formed by photocatalytically activated anatase[145].

5.1.3 Bioactivity of TiO_2 coatings

A common feature of all bioactive materials is a HAp layer formation on their surface when they are exposed to physiological fluids. It is a complex mechanism that involves cellular processes. However, it can be predicted using in vitro studies by soaking in acellular simulated body fluid. Non-coated and non-treated titanium alloys do not exhibit any ability to form apatite in an SBF solution, even after prolonged soaking under the conditions of the widely used Kokubo test[124], which was also confirmed in the present study. Though the non-treated Ti6Al4V sample retained its surface morphology while soaking for 3 weeks in SBF (Figure 28a), apatite formation was observed on some hydrothermally treated samples (Figure 29). The Ca/P ratio was confirmed by EDS to be 1.67, which is the stoichiometric ratio of hydroxyapatite. Compared to other bioactive materials, such as hydroxyapatite and bioactive glass, the apatite formation time was longer for the TiO_2-coated samples (3 weeks), but this was a valuable improvement over the lack of apatite formation with non-treated Ti6Al4V.

Moreover, bioactivity was observed only for the TiO_2 coatings with specific morphologies. In our experiments, amorphous TiO_2 coatings or coatings with round-shaped crystals (anatase crystals with no sharp edges) never induced apatite formation (Figure 28), which was also observed by Grigal et al.[146] The importance of crystallinity for apatite formation has already been reported by Wu and Wang [147, 148].

Although an in-depth study of the mechanism of hydroxyapatite formation on TiO_2 coatings was not performed as part of the present study, the results provide strong indications that the bioactivity is promoted not only by the surface area or thickness of the TiO_2 coating, as reported by [147, 148], but also by the morphology of the anatase crystals. Various levels of bioactivities can be explained by the effects of TiO_2 coating morphology, as well as by the different reactivities of the anatase facets. Indeed, the {001} anatase facets have been reported to be the most reactive [149], which could be also reflected in their higher bioactivity.

The thickest and most dense hydroxyapatite layer apparently formed on the TiO_2 coating with pinacoidal anatase crystals and the addition of Ca^{2+} ions (Figure 29d). The bioactivity expressed by apatite formation on this surface can be ascribed to the presence of the Ca^{2+}, as seen in the XPS analysis of the coating (see Figure 19d). This finding confirms that Ca^{2+} ions are beneficial for the bioactivity of the coating, in addition to providing a suitable morphology of the TiO_2 coating, which we think is a prerequisite for apatite formation.

The TiO_2 bioactivity in most reports is described by the formation of Ti-OH groups on the surface of TiO_2. These OH groups induce apatite nucleation indirectly by forming calcium titanate on its surface[150]. The Ti-OH groups are negatively charged as the pH of the surrounding fluid is 7.4[151]. Negatively charged OH groups then attract positive Ca^{2+} ions and a Ca-titanate is formed. With accumulating Ca, the surface becomes positively charged, and thus it starts to combine with phosphate ions from the SBF to form calcium phosphate. With time amorphous calcium phosphate transforms to the most stable form at that pH, hydroxyapatite. This widely accepted idea was also confirmed by Han et al[152], who UV irradiated samples to form abundant OH groups (negatively charged) on the surface that causes a lower wetting angle and were also responsible for the negative charge of the titania in SBF and therefore the bioactivity of the UV irradiated samples was much higher.

In our experiment we found that hydroxyapatite is precipitated from SBF better if the TiO_2 particles in the coating contain larger {001} facets. It is known that {001} facets have a much higher energy (0.90 J/m^2) compared to lower surface free energy (0.44 J/m^2) of thermodynamically stable {101} facets[153]. And the coating with the higher free energy Ti ions exhibit better bioactivity[154]. The {001} facets also have a high density of surface undercoordinated Ti atoms that are responsible for more active sites[152]. The Ti-OH groups are responsible for the precipitation of HAp.

No reports were found about the dependence of bioactivity on different anatase morphology. The difference is often ascribed to the different, usually negative zeta potential of the TiO_2 coating in SBF as IEP of the titania is below the pH of the SBF. Such negatively charged titania then interacts with positively charged Ca ions in the fluid and in some cases positively charged titania reacts with phosphate ions[150, 151, 155]. However, none of the reports have considered that their coating prepared at different treatment conditions could have a different anatase morphology having different developed facets with different surface energy or possibly a different zeta potential.

5.1.4 *In vitro* tests of TiO_2 coatings

The results of the *in vitro* studies show that the grain morphology of the anatase coating plays an important role in cell adhesion and proliferation. Both the HOC and HEC attached well to the TiO_2 coating with pinacoidal crystals (sample 3, HT E2). Though the growth of HOC strongly decreased after day 3, the HEC continued to grow and further colonise the sample until day 9. Thus, compared to the sample with bipyramidal crystals (sample 2, HT D1), the smaller pinacoidal crystals (sample 3, HT E2) are obviously more favourable for cell adhesion and spreading. This finding is similar to hydroxyapatite formation in simulated body fluid, which was also only seen for the sample with pinacoidal crystals. Though anatase coatings have been reported to promote cell adhesion and proliferation [156], and a difference exists between the anatase and rutile forms of TiO_2 coatings[157], no reports have investigated the influence of different anatase crystal morphologies. Feng et al.[158] showed that the surface energy, the number of surface hydroxyl groups, and the surface charge can all have a significant effect on osteoblast behaviour, and a positive surface charge has also been shown to stimulate cell attachment and spreading on anatase[159]. The crystal planes in anatase have different surface properties than those of rutile, which results in selective adsorption and activity in these planes[160] and can explain the different activities of the various coatings in simulated body fluid, as well as cell attachment. Accordingly, bipyramidal anatase crystals have a negative effect on cell adhesion, whereas pinacoidal anatase crystals are more favourable. The cell proliferation was better for pinacoidal anatase than for the non-coated samples, which can be ascribed to the more hydrophilic surface of the TiO_2-coated alloy.

Compared to the non-coated Ti6Al4V alloy (Figure 30), there was lower HOC and HEC cell adhesion and proliferation on the non-coated porous titanium layer (Figure 31), which supports the assumption that wetting plays a major role; the wetting angle of the porous titanium was higher than that of the Ti6Al4V alloy (130° and 91°, respectively). However, the results for the TiO_2-coated samples with a porous titanium layer seem to disagree with this assumption; compared to the non-coated reference (sample 4, Figure 31), the TiO_2-coated sample (sample 5, Figure 31) did not reveal a positive effect on cell adhesion. Due to the hydrophilicity of the TiO_2 coating, the cells may have migrated into the pores instead of adhering to the surface and could not be detached completely, resulting in under-counting. This explanation is further supported by *in vivo* tests.

5.1.5 *In vivo* test of TiO_2-coated samples

The *in vivo* tests showed statistically significant difference ($p<0.01$) between the non-coated and TiO_2-coated alloy with a porous titanium surface layer. Though bone-to-implant contact was approximately the same (~45 %) in both cases, the newly formed bone grew much deeper into the porous structure of the TiO_2-coated samples. As a result, the bone ingrowth percentage was double that of the non-coated porous titanium. Interestingly, the newly formed bone was also observed in the smallest pores, close to the substrate alloy. Most of the previous reports on a suitable pore size for successful osseointegration[161-165] have suggested that the pores should be of an appropriate size to allow the bone cells to enter and attach; the lower limit in biomedical implants is approximately 30 µm[164], though most reports have suggested it to be closer to 100 µm. As seen in Figure 33, the pores as small as only a few micrometres had evidence of new bone, which indicates that the size of the pores is not a limiting parameter for the successful ingrowth of new bone. The conclusion regarding the minimum pore size for the cells can be presumed to have been based on the results from hydrophobic metal surfaces. As shown above (Figure 27), the anatase TiO_2 layer produced by the hydrothermal treatment alters the wetting behaviour of the naturally hydrophobic titanium metal in such a way that it becomes more hydrophilic. Thus, the favourable wetting behaviour of TiO_2-coated implants was probably the main reason for the growth of the new bone cells into the smallest pores throughout the thickness of the titanium layer. The importance of wetting, in combination with surface roughness and pore size, for was also confirmed by meta analyses of *in vitro* results in a more extensive study by Gasik et al.[166]

5.2 Bioactive glass

5.2.1 Bioactive glass synthesis

The sol-gel method is widely used for bioactive glass preparation. Mostly it is prepared by a polymeric sol-gel route using nitric acid as a catalyst. In this study BAG powders with four different compositions were successfully prepared using a basic catalyst NH_4OH, which resulted in a smaller particle size compared to the melt-derived or polymeric-sol-gel-route-derived glasses. The size of the BAG powder was reduced from 90 for polymeric to around 11 µm for particulate after the dispersion (Table 13), which is the size of the BAG agglomerate. The size of an individual BAG particle, measured on SEM images, is even smaller, between 100 and 200 nm.

Using ammonia in the polymeric sol-gel route slightly decreased the size of the BAG particles, but not as much as reported in the literature. Xia et al. claims that they were able to prepare BAG particles using this method that were smaller than 50 nm[91]. However, they measure the particle size only on TEM images where it is clearly seen that particles smaller than 50 nm are just individual subunits of much larger agglomerates, most probably strongly connected by the Si-O-Si bond formed during condensation. Similar results were obtained by Hong et al. who were able to homogeneously disperse as-prepared BAG in an ethanol solution[92]. However, in their BAG synthesis they used the centrifugation and washing of BAG precipitates with water, which was observed during this study to cause the elimination of Ca^{2+} ions from the BAG compositions, especially the one with a low network connectivity (results not shown). This explains why they were able to disperse particles in ethanol, as silica itself, without Ca^{2+} ions, has a high ZP (Figure 41). The composition of their BAG after centrifugation was not reported, neither was the crystal phase formed during the sintering that could reveal if there was Ca present.

There are a few reports trying to prepare BAG with a basic catalyst[92-94]. Meiszterics et al. who used NH_4OH as a catalyst for both hydrolysis and condensation was unsuccessful due to the unwanted precipitation[93] of calcium salts. The precipitants in their study were most probably formed due to a too high and too sudden pH rise of the system by mixing ammonia directly with other reactants. In our study $Ca(OH)_2$ precipitation was avoided by the dropwise addition of calcium nitrate into the mixture of water, ethanol and other nitrates or acetates (Figure 39) that contained excess of water for keeping the calcium nitrate soluble and most important the pH of that mixture (pH10.5) was carefully maintained by the dropwise addition of NH_4OH, where the pH value never exceeded the minimum value for $Ca(OH)_2$ precipitation that was calculated for the system to be at pH11.3, neither it exceed the pH value for silica dissolution. In another study Labbaf et al.[94] tried to prepare the bioactive glass by adding Ca into the system by diffusion through the surface of the SiO_2 particles. Calcium nitrate was introduced into the system when SiO_2 particles were already precipitated and was deposited on the silica particles. As Ca had to diffuse into the particles from their surface after they had already been formed, they had problems to incorporate Ca into the network and were able to obtain the composition only with a maximum 15 mol.% of calcium.

With the dropwise addition of the reactants and a controlled pH all four BAGs were prepared with the desired compositions (Table 14), avoiding unwanted precipitation. All the glasses were amorphous after calcination, except when using Na-ethoxide precursor (Figure 45).

The main drawback of the particulate sol-gel synthesis is unwanted agglomeration of the particles that is caused by the addition of salts into the sol, especially Ca^{2+} ions that are a source of the ions necessary for bioactivity and HAp formation. Silica itself is very stable since the silanol groups are the adsorption sites for water and the silica is stabilized by the layer of adsorbed water that prevents coagulation even at the IEP[74], but the addition of Ca lowers the stability of the sol and with that the size of the particles. To lower the particle size to be able to produce a stable suspension for the deposition and to fill the smallest pores in the porous substrates, BAG powder was de-agglomerated after calcination by the addition of PEI, which decreases the size to around 11 µm and also increased the ZP of the ethanol suspension.

After sol-gel synthesis, the BAGs had to be calcined in order to eliminate the residual organics and nitrates. The calcination temperature has to be lower than the sintering temperature and the crystallization temperature, which is the case for all compositions except BAG 53S that is containing Na_2O. In this composition, prepared under the previously described condition, a DSC peak correlated to the loss of NO groups was detected at around 800 °C (Figure 42) which is far beyond the onset temperature for sintering, and it is finished at 810 °C (Figure 44b). To avoid sintering of the particles during calcination in this composition, the calcination temperature was left at 600 °C and therefore residual nitrates in the BAG 53S were removed only during sintering. This caused bubbling of the BAG sample thus making it highly porous (Figure 46a). Decomposition of the nitrates at such high temperatures can be avoided by using a different catalyst, as reported by Lucas-Gyrot et al.[167], or by changing precursors for Na_2O. The latter was used in this study. $NaNO_3$ was replaced by Na-ethoxide. This led to a higher calcination temperature (650 °C) and also a higher sintering temperature (900 °C). Sintered BAG pellets had no macroporosity (Figure 47). As the bubbling of the material caused problems in the bulk pellets and was not causing problems in the thin coatings, $NaNO_3$ as precursor was kept for BAG synthesis used *in vivo* studies due to a lower sintering temperature.

The BAGs prepared by the particulate sol-gel method stayed amorphous till their sintering temperature, except BAG 53S, where crystallization started arund 800 °C with the formation of calcium sodium silicates. It is known that the crystallization of BAG reduces bioactivity but it was also reported that calcium sodium silicate decomposes and transforms to amorphous hydroxyapatite when exposed to body fluid and is an easily degradable mineral *in vivo*[168], and therefore this crystal structure can still be highly bioactive.

Another drawback of the sol-gel synthesis is the inhomogeneous structure of BAG that is a consequence of the migration of Ca^{2+} ions through the silica structure during drying and its aggregation[169]. To avoid that, instead of slow drying in an oven where the reaction of condensation still proceeds, the drying was done in a microwave oven. The heating produced by microwave energy allowed a fast dehydration. The faster drying thus resulted in a more homogenous composition.

5.2.2 Bioactivity

The bioactivity of bioactive glasses was estimated by *in vitro* studies by soaking sintered discs in acellular simulated body fluid in the same manner as for TiO_2 coatings. All four compositions were immersed in SBF in order to see, compare and to choose the best candidate for further *in vivo* studies.

According to the time needed for the HAp formation and according to the density of HAp formed after 5 days of immersion, the most bioactive BAG was BAG 53S containing Na_2O. A similar bioactivity was also observed for BAG 70S. As seen in the FTIR spectra these two compositions had a large number of non-bridging oxygen species (NBO: $Si\text{-}O^- \; Ca^{2+}/Na^+/H^+$). These NBOs are responsible for breaking the continuity of the network between the Si atoms, thus making the glass easier to dissolve. And by dissolution the Ca^{2+} and Na^+ ions are released in surroundings and are further replaced by H^+ from the SBF solution forming silanol groups that are playing a key role in the bioactivity[133, 170, 171]. A corresponding increase in the pH also promotes the breaking of Si-O-Si bonds and thus the formation of even more Si-OH groups. Therefore, BAG 53S reaching higher pH values than 70S (Figure 50) is also resulting in faster HAp formation. BAG 53S was also the only composition that partially crystallized during sintering (seen in XRD spectra in Figure 45 and in TEM images in Figure 66). Although it is known that the crystallinity of BAG reduces the rate of HAp formation[172, 173], this composition still retained the highest bioactivity, which was most probably compensated by high dissolution of amorphous phase.

The BAG containing Sr also showed good bioactivity; it was densely covered with HAp after 5 days of immersion. This is in contrast to Zn that had delayed HAp formation where after 5 days surface was covered by HAp only partly. The difference between those two glasses and also the other two compositions is seen again in the band corresponding to NBO in the FTIR spectra; in contrast to 58S4Zn, the 58S4Sr has a band at 930 cm^{-1}. Zn is classified as an intermediate oxide, i.e., it can act as a glass modifier or a glass former[174]. And when 4 wt.% of Zn is added to the glass composition (858S4Zn), it seems that Zn starts to act as a glass former; The peak at 900 cm^{-1} that is almost not visible for bioactive glass containing Zn is explained by the lack of NBO in the silica network. As an intermediate oxide Zn created a more stable glass structure with the formation of covalent links between the silica tetrahedral and thus the formation of more bridging oxygen (BO) species rather than NBO. With increasing BO over the NBO the number of nucleation sites for HAp (Si-OH groups) is low, the dissolution rate is reduced and therefore the HAp formation is slower. Some reports show that Zn added to BAG increases the acellular bioactivity[107, 175, 176], however other studies showed that Zn has the opposite effect: Aina et al. have shown that Zn is responsible for the reduction of leaching and the dissolution activity of BAG and an inability to form HAp[177]. Similarly, Jaroch et al. showed that Zn retards the rate of HAp formation and Haimi et al. showed reduced BAG degradation properties[108]. The lack of NBO in the FTIR spectra of BAG containing more than 1 wt.% of ZnO has also been observed by El-Kady et al.[178].

The FTIR band at 930 cm^{-1} for BAG 58S4Sr is present because Sr is a network modifier; it acts like Ca with which it can even be replaced. So the addition of Sr instead of Zn is to obtain a lower network connectivity. It was also reported by other authors that Sr incorporated BAG increases the acellular bioactivity and has a faster degradation[179, 180]. Usually Ca was replaced by Sr that due to its larger atomic size expands the glass network and makes it less connected[181]. In this study Sr was not replacing Ca but Sr was added in the first place to the composition to achieving antibacterial properties, and therefore the role of Sr was in forming more NBOs.

According to the findings in this study and reports described above we can approximately predict the bioactivity from the molar composition of the BAGs. To explain: the composition of BAG 53S should be the most bioactive as it contains the lowest amount, only 53 wt.%, of silica (network former) and a large amount of modifiers, together 43 wt.% of Ca and Na. It also contains 4 wt.% of P_2O_5 which in bioactive glasses does not go to network, it forms orthophosphate species that remove cations for charge balancing NBOs and thus increasing the network connectivity. However, P supersaturation on the other hand drives precipitations of HAp. BAG 70S has a high amount of SiO_2, but compared to 58S4Sr and 58S4Zn contains the same amount of Ca, no phosphate to increase the connectivity (as it is Sr and Zn containing BAG, 8 wt.%) and also has no additional network formers (like Zn). As Sr is a network modifier and Zn can act also as a network former, it is obvious that between those two glasses Sr should have better bioactivity also due to the slightly larger atom that expands the network and reduces the rigidity of the network.

5.2.3 Antibacterial properties

Antibacterial properties are desired for biomedical materials as they can help to prevent infections in the first stage of implantation and thus help the bone cells in their "race for the surface" with bacteria. Bioactive glasses have already been reported to have antibacterial properties, some of them by themselves,[55 119, 182] and some of them by adding different antibacterial agents, among which Ag is one of the most popular[56, 183, 184]. The exact mechanism of antibacterial properties is still not known. It has been suggested to be based on several factors, including high pH and osmotic effects caused by dissolved ions. In this study two BAG compositions were prepared in order to increase the bioactivity and antibacterial effect; BAG 58S4Sr and 58S4Zn. Sr is mostly known to promote bone growth[185] but was also suggested to have a negative effect on bacteria growth[34]. Zn is known for its antiseptic properties [105, 186, 187] as well as for bone regeneration[188, 189].

The optical density (OD600) measurements showed that only BAG 53S and the 58S4Sr ionic dissolution product have an effect on bacteria growth. BAG containing Na_2O reached the highest pH values (Figure 50), around 8.5, which could be the reason for the bacteria growth inhibition. On the other hand, the low pH of 58S4Sr was similar to those of 70S, however their effect on bacteria was totally different. The difference was especially noticeable for the more sensitive S. *epidermidis* and during the first day of incubation also for S. *aureus,* where 70S had no and 58S4Sr had high inhibitory effect. The same trend was followed when growth was evaluated on the surface of BAGs by CFU counting. However, due to the higher concentration of ions near the BAG surface compared to the concentration in the surroundings, the intensity of inhibition was bigger when bacteria growing on BAG surface were counted (CFU) compared to bacteria growth in the surroundings (OD600).

No inhibition of bacteria growth was seen for BAG containing Zn, although this BAG was expected to have the greatest inhibitory effect according to the well-known antibacterial properties of ZnO. The reason for such a contradictory result is most probably in the ion-leaching activity of Zn-containing glass. It was already reported that BAG containing only 5 wt.% of Zn reduces the solubility of bioactive glass and therefore its bioactivity[108, 177]. The low bioactivity of Zn-containing glass was also proved in this study (Figure 51). If the degradation rate of BAG is slow, the amount of Zn ions cannot be sufficiently high to influence the bacteria. Besides that, a lower degradation rate reduces the concentration of Ca^{2+} and other released leached alkali ions that act bactericidal by depolarising the bacteria membrane[123]. Slower solubility is caused by better network connectivity of the Zn-containing BAG which can be seen in the FTIR spectra (Figure 49). The intensity of the NBO band at ~930 cm^{-1}, belonging to $Si\text{-}O^-$ bound to Ca^{2+} and Na^+ ions, is the weakest for BAG 58S4Zn. The number of NBO is thus small and therefore the number of Si-O-Si bonds is greater. On the other hand, the band for NBO species that also plays an important role in bioactivity, as they break the continuity in the lattice, is much more intensive for BAG containing Sr and Na. This explains the reason why both compositions decrease bacterial growth although BAG 53S reaches much higher pH values than 584Sr. Moreover, BAG 58S4Sr reaches the same pH values as the two-component BAG 70S, which in contrast had no influence on the bacteria growth, shown by OD600 measurements (Figure 54), CFU counting (Figure 55) and strong biofilm formation on its surface (Figure 56). The antibacterial effect was also shown by Guida et al. where Sr added to glass ionomer cements showed antibacterial properties although there was no pH increase due to the acidic nature of the cements.[110] BAG 53S is not just reaching the highest pH values that could be detrimental for bacteria, but is also having the highest solubility as seen by the fast degradation process (Figure 52) and the lowest network connectivity (large number of NBO). Therefore, we cannot say that antibacterial properties of BAG are caused by the high pH values reached during the dissolution process, as reported elsewhere[55, 118, 190]. They are mostly referred to non-physiological concentrations of ions dissolved from BAG, as reported by Sawai et al. and Stoor et al.[117, 123]. It has also been shown that the bactericidal activity of BAG in comparison with a NaOH reference solution has a significantly higher minimum inhibitory concentration than NaOH with the same pH[191].

As the possibility of bacterial adhesion and biofilm formation is a remarkable problem concerning biomedical devices it is of great importance that for BAG coatings on Ti-alloy implants a BAG with a suitable composition is selected, not just for bioactivity but also for antibacterial properties.

5.2.4 *In vivo* tests of BAG coatings

To assure both the above-desired properties of the metallic implant, bioactivity and antibacterial properties, a four-component BAG containing SiO_2, CaO, Na_2O and P_2O_5 was chosen for the *in vivo* tests. The BAG with similar composition, however with higher amount of Na_2O, proved to be the most bioactive when tested in acellular SBF and also had the greatest bacteria growth inhibitory effect. BAG was applied into the porous surface layer of a Ti implant by vacuum infiltration. The porous surface layer has an advantageous effect on the implants: while a gap between the bone and parts of metal with a flat surface was observed in almost all the samples after explantation from rabbit tibia, the new bone was well attached to the porous layers with or without the coating (Figure 68).

The ability of bioactive glasses to enhance bone formation has been presented in many previous scientific reports[50, 73]. In addition, stimulation effects on angiogenesis as well as antibacterial and inflammatory effects were reported [53, 54, 119, 120] and also confirmed in this study. These effects have been ascribed to the availability of ionic products dissolved from the bioactive glass, especially calcium and silicon ions, which were recently reported to play a key role in bone regeneration. The ions released during dissolution of the BAG in the porous metallic structure stimulate several families of genes and activate some growth factors that control osteogenesis[71-73]. Moreover, the surrounding bone is in direct contact with the surface apatite formed during BAG dissolution, without the intervention of any fibrous tissue and consequently a tight chemical bond is formed with the apatite[54, 63]. In spite of all that, due to its poor mechanical properties the application of BAG in orthopaedic surgery has still been limited to non-loaded applications.

The above-described advantages of bioactive glass have been reported on the basis of numerous *in vitro* and *in vivo* studies of BAGs with different chemical compositions and in different forms, such as granules or coatings on metals, while the enhancement of osseointegration of porous metallic structures by impregnation with bioactive glass has not been reported before. This is partly due to the technological limitations given by the relatively coarse particles of melt-derived bioactive glasses or their limited resorbability defined by their composition and crystallinity. Differently, the bioactive glass used in this study is characterized by small particle sizes that enable impregnation of the porous titanium. After the thermal treatment, a porous BAG structure with high resorbability is formed within the pores of the titanium layer on implant. The high resorbability of the bioactive glass is reflected in its absence in the porous titanium layer of the implanted grafts after ten weeks of implantation in rabbit tibia and, instead, the presence of newly formed bone. The bone was observed throughout the thickness of the porous layer, which confirms that the dissolution product of the bioactive glass in the pores provided an appropriate and stimulating environment for the bone growth. Conversely, this was not the case for the implants without BAG, where the bone formed only within the outer part of the porous Ti-layer. In the case of implants with BAG, the new bone has also formed in the smallest pores, in the deepest parts of the porous titanium layer and also in the site of the implant facing bone marrow, thus, everywhere where the implant surrounding was saturated with calcium and silicon ions released from the bioactive glass. The porous structure of BAG obviously contributed to fast resorption: in ten weeks, the entire BAG was replaced with a newly formed bone, which indicates favourable dissolution kinetics under physiological conditions.

Considering everything, the *in-vivo* animal study confirmed that the nanoparticulate bioactive glass prepared by sol-gel introduced into the porous titanium surface layer on implants promotes osseointegration. Within ten weeks, the bioactive glass was completely resorbed and substituted with well-attached, newly formed bone, which overgrew the entire thickness of the porous structure. The percent of pores occupied by bone was increased from 22 % to almost double this value (38 %) for the implants contacting BAG, which represent significant ($p<0.05$) improvement as it implies faster bone ingrowth during the first weeks after implantation. The bone-to-implant contact on the other hand was the same for the samples with and without BAG (around 52 %) which is most probably connected to the very high solubility of BAG with the composition containing Na_2O (see Figure 57). Due to too fast dissolution, most of the released ions from the outer surface of the implant might had been transported away from the surroundings of the implantation site before new bone could be formed, which is not the case inside the pores where BAG is protected from fluid motions.

5.3 TiO_2/BAG coatings

In previous sections two coatings, TiO_2 and BAG, were described separately, although both have one common feature: to improve osseointegration. However, BAG serves only as a temporary coating that helps to promote bone bonding in the early stages after implantation and is dissolved already after 10 weeks (shown by *in vivo* tests), while TiO_2 on the other hand is a permanent coating that improves bioactivity and hydrophobicity and also hinders the release of undesired metal ions. To combine all these properties we prepared a multifunctional coating of porous Ti, TiO_2 and BAG. BAG would improve osseointegration in the first days and then after its dissolution, when surrounding tissue would be exposed to the metal, TiO_2 would serve as a protection barrier for the release of metal ions from the Ti-alloy and as a more appropriate surface for cells as hydrophobic metal itself.

The sintering of BAG on non-coated and on a TiO_2-coated Ti-alloy resulted in the formation of intermediate layer, composed of 2–5 nm big Ti_xSi_y crystallites, at the BAG-titanium contact, whereas the layer was thicker on the TiO_2-coated alloy. Such a layer was already reported by other authors[192, 193] and is ascribed to contribute to the improved adhesion of the BAG to the substrates. The adhesion of BAG within the porous coating, however, is not relevant. We suppose that the Ti-silicide may, due to the silicon's presence, contribute to an improved biological response, even after the bioactive glass has dissolved.

When both coatings were applied, TiO_2 and BAG, the BAG coating stayed preferentially amorphous, whereas the BAG coatings applied directly on the Ti6Al4V crystallized. And because the crystallinity of the BAG reduces the dissolution rate and thus the bioactivity, a TiO_2 intermediate layer is beneficial when BAG is used as a coating on Ti-alloy. However, the TiO_2 layer increased the amount of Ti present in the bioactive glass coating. The Ti diffused to the BAG coating during sintering, but to a greater extent when the TiO_2 was present. 5–10 at.% of Ti was found in the glass region without TiO_2 coating and 10–20 at.% in the glass region on TiO_2 coated alloy. The presence of Ti^{4+} in the glass region would therefore result in free Ti^{4+} ions that would go into surroundings of an implant after BAG dissolution, which is the opposite to what we tried to achieve by TiO_2 coating prepared by hydrothermal synthesis. However, the release of the metal ions from the BAG would not be continuous as it is from metal implants. The amount of Ti ions released from BAG coating during first week after implantation cannot be compared to a continuous release from a non-coated implant throughout its lifetime. And after the complete dissolution of BAG, the surrounding tissue will be exposed directly to a metal surface, so it is important that the some barrier for metal ions still exist in the long term.

The coatings, TiO_2 and BAG, prepared in this study can be used as individual coatings or together. But when used together a risk of released Ti^{4+} ions from the BAG during its dissolution in the first weeks after implantation has to be taken into account. Both coatings are beneficial for orthopaedic and dental implants where osseointegration in the early stages after implantation is critical for good implant fixation and faster healing of patients. The hydrothermal treatment is also a very easy and cheap method that would not increase the cost of the implant, whereas for the preparation of bioactive glass the coating prices of the pure reactants for sol-gel synthesis should be taken into account for the final product. However, the use of BAG prepared in this study by the particulate sol-gel method can be extended for other products such as additives for toothpaste treating hypersensitivity, fillers for polymeric scaffolds to improve osseointegration or as bone fillers for non-load bearing applications.

6 Conclusions

In the present work, samples with improved osseointegration were prepared by applying two different coatings. Ti-alloy samples with or without a porous Ti-layer were coated with a layer of TiO_2 by hydrothermal treatment and/or a particulate bioactive glass prepared by sol-gel synthesis.

The procedure described for the hydrothermal treatment represents a simple, single-step technique for coating the Ti6Al4V alloy with a protective, bioactive, photocatalytic layer of anatase TiO_2 that is firmly bonded to the Ti-based substrate.

The crystal growth during hydrothermal treatment is a dynamic equilibrium of dissolution and precipitation that is affected by the solution concentration, temperature and additives. By changing one parameter all the other parameters are affected, therefore it is hard to predict the right conditions. However, from the current study it can be concluded that for the formation of a homogeneous anatase coating with a truncated bipyramidal morphology, that was shown to be important for cell adhesion and for bioactivity, there must be sufficient Ti^{4+} ions, which is reached in the first stage using a higher temperature, high pH, and addition of TMAH. Besides dissolution, also the re-precipitation rate has to be high enough for the particles to grow, which was achieved by NaOH as a mineralizer. For the proper anatase morphology with truncated crystals ammonium citrate was added, which lowered the surface energy of the {001} facets, thus making them less prone to further growth.

We have shown that in a mixture of different additives, such as NaOH, TMAH, and citric acid, a layer of pinacoidally shaped anatase can fully cover the surface of the alloy substrate, even on highly complex surfaces such as dental screws and porous titanium coatings. The layer is strongly attached to the substrate (>22 MPa), providing the shear strength required for use as a protective coating for implants. The results suggest that with the anatase TiO_2 coating, the direct exposure of the body to the toxic elements aluminium and vanadium will be strongly reduced. A lower concentration of these ions is released into physiological solutions at 36.5 °C.

The coating converts the originally hydrophobic implant surface to a hydrophilic surface, particularly after UV irradiation. The bioactivity of the titanium alloy is also enhanced by the TiO_2 coating; in SBF, apatite-like formation was observed after 3 weeks. This apatite formation depends on the morphology and the size of the TiO_2 crystals and is further promoted by Ca^{2+}.

Ti6Al4V alloy discs and discs with a porous titanium layer were hydrothermally treated to produce an anatase coating with favourable properties for osseointegration. The non-coated and coated samples were tested *in vitro* and *in vivo*. The *in vitro* tests confirmed that there were no cytotoxic effects associated with the TiO_2 coating. The grain morphology of the anatase coating appears to play an important role in cell adhesion and proliferation; the bipyramidal anatase crystals caused cell detachment, whereas the pinacoidal anatase crystals were favourable for cell proliferation.

The *in vivo* tests after 10 weeks of implantation showed an improvement in the bone ingrowth for the TiO_2-coated samples compared to the non-coated, though the bone-to-implant contact remained approximately the same (45 %). Due to the hydrophilic behaviour of the TiO_2 coating, the bone occupied the pores throughout the thickness of the porous titanium layer, even in the smallest pores that were only a few micrometres in diameter.

Thus, the results of this study show that the anatase surface morphology and the wetting properties have large effects on the osseointegration. Based on the favourable physical and chemical properties (high adhesion strength, enhanced wetting, and the decreased release of metal ions) and the favourable *in vivo* behaviour shown here, we can conclude that a hydrothermal treatment to achieve a TiO_2 coating on the Ti6Al4V alloy and porous titanium offers a simple and cost-effective method for improving osseointegration. This method is particularly advantageous for coating the internal walls of porous titanium layers applied to implants to provide better support to the bone.

In this study titania was proven to be bioactive, but the rate of hydroxyapatite formation is still slow compared to other bioactive materials such as hydroxyapatite or other calcium phosphate ceramics and bioactive glasses. Therefore, bioactive glass was used as another coating as it is bio-resorbable, has very good bioactivity and can form a strong bond with soft and hard tissue. It was proposed that a combination of a porous titanium surface layer coated with BAG would significantly improve the osseointegration, therefore BAG powder synthesis was directed to the formation of particles small enough to be able to prepare a coating within the porous titanium structure. For this reason a particulate sol-gel method was developed in this study to prepare submicrometer-sized particles.

Bioactive glass powder was successfully prepared by the particulate sol-gel route, using basic conditions for the first time. 100–200-nm-large BAG particles were prepared, however they were highly agglomerated due to the large amount of Ca^{2+} ions that lowered the BAG particle stability in the suspension. With the addition of PEI, particles with an average size of 1 μm were achieved. Moreover, the inhomogeneity of the BAG powder that is usual for sol-gel synthesis was avoided by a controlled reactant addition, a strictly controlled pH during the synthesis, and by fast drying of the powder in a microwave dryer.

Four bioactive glass compositions were examined and compared to choose the best candidate for the *in vivo* tests. All four compositions showed good bioactivity, i.e., hydroxyapatite was observed on the surface after one day of immersion in simulated body fluid, except for the composition containing Zn. The delayed bioactivity of this glass was correlated with a lack of NBO groups in the silica network and is also ascribed to ZnO working as an intermediate oxide, thus creating a more stable glass structure. The very good bioactivity of 53S and 70S on the other hand was ascribed to a large number of NBO ($Si\text{-}O^- \; Ca^{2+}/Na^+/H^+$), which are responsible for breaking the continuity of the silica network, and thus making the glass more easy to dissolve and to release Ca^{2+} and Na^+ ions into the surroundings.

The antibacterial properties were also correlated to the network connectivity. The Zn-containing glass with a low degradation rate had therefore no effect on the growth of bacteria. A larger amount of NBO in the BAG compositions containing Sr or Na resulted in the inhibition of bacteria biofilm formation. As BAG dissolves faster, more Sr and Ca and other alkali ions are released from the glass to inhibit the bacteria growth, as well as the pH values on the BAG surface reaching higher values, which is detrimental for bacteria growth. However, we showed that the pH is not a critical factor for the antibacterial properties as BAG 70S reached the same pH values during dissolution as BAG 53S, but on the former we observed biofilm formation.

For the *in vivo* test BAG containing Na, was chosen due to excellent bioactivity and antibacterial properties of BAG 53S that has similar composition, but has higher amount of Na_2O. BAG was applied by vacuum infiltration into porous Ti. The high resorbability of the particulate bioactive glass was proven by *in vivo* tests and reflected in its absence in the porous titanium layer of the implanted grafts after ten weeks of implantation in rabbit tibia and, instead, the presence of newly formed bone. This bone was observed throughout the thickness of the porous layer, also in the smallest pores and in the site of the implant facing the bone marrow. Conversely, this was not the case for the implants without BAG, where the bone formed only within the outer part of the porous Ti-layer.

When the TiO_2 and BAG coatings were applied together on Ti6Al4V, we observed that an intermediate layer of titanium silicides was formed between the metal and BAG and this layer was thinner when the BAG was applied directly on the Ti-alloy (without TiO_2 coating). A positive contribution of the TiO_2 coating beneath the BAG coating was that the BAG stayed preferentially amorphous, whereas it crystallizes when applied directly on the Ti-alloy. However, more Ti^{4+} ions diffused into the BAG coating when the TiO_2 was present, which means more free Ti^{4+} ions released into the body during BAG dissolution.

It is supposed that both coatings, TiO_2 and BAG, applied together would improve osseointegration in the first days by BAG and then after its complete dissolution, when the surrounding tissue would be exposed to the metal, the TiO_2 would serve as a protection barrier for the release of metal ions from the Ti-alloy and as a more appropriate surface for cells as a hydrophobic metal itself.

7 Acknowledgements

First, I would like to thank my Ph.D. supervisor, Asst. Prof. Saša Novak Krmpotič for the encouragement, support and guidance during my work and study at the Jožef Stefan Institute, as well as for all the advice, ideas and fruitful discussions.

As this work was done as a part of the European project Meddelcoat, many people within this project have contributed to the work and many of the results presented would not be able to obtain without their help. Therefore, I would like to thank Prof. Dr. Jef Vleugels for giving me the opportunity to work and to perform TG, DSC and dilatometry analyses in his research group at MTM KU Leuven during my one-month scientific exchange, and Prof. Dr. Lieve Van Mellaert at KUL REGA institute for all the help with the bacteria tests. Dr. Annabel Braem and Dorien Hofmans are also acknowledged for helping me in the laboratory during my visit in Belgium. I would like to thank Prof. Dr. Marie-Françoise Harmand and Dorothée Pierron from Laboratoire d'Evaluation des Matériaux Implantables (LEMI), Technopole Bordeaux-Montesquieu, France for performing cell test, Marko Gradišar (Helipro d.o.o.) for helping me with preparing explanted *in vivo* sample for further observation and Dr. Matevž Gorenšek for performing *in vivo* tests. I would also like to thank Urška Dragin from the Faculty of Medicine for the preparation of histological sections and for helpful discussions and explanations. Thanks also to Dr. Elke Fuchs from Universität Bayreuth for performing DSC and MS analyses.

Thanks to Asst. Prof. Nina Daneu for introducing me innovative idea of TiO_2 coatings prepared by hydrothermal synthesis, for a great help and ideas at the beginning of this study, for the TEM analysis and interpretation. Without her the hydrothermal synthesis of TiO_2 coating would never be established.

Thanks also to Asst. Prof. Aleksander Rečnik for valuable discussions, as well as for the TEM analysis and interpretation of results.

I would also like to thank Prof. Dr. Miran Čeh for TEM analysis and interpretation of results and FEG-SEM analyses of *in vivo* samples.

Thanks also to Dr. Matjaž Mazaj from Institute of Chemistry for using his equipment for hydrothermal synthesis when starting with experiments and for FEG-SEM examinations of the samples.

Thanks to Prof. Dr. Radmila Milačič and Anže Martinčič from IJS O2 for the ICP-MS analysis, Dr. Janez Kovač for XPS measurements and Sandra Kure for EPR measurements.

Thanks also to Dr. Sebastjan Perko and Dr. Miha Čekada for the help with adhesion tests.

Thanks also to Medeja Gec for the TEM sample preparation.

I would like to thank Gregor Murn, Jaro Bele and Mateja Paščinski for their technical assistance.

I would also like to thank Dr. Katja Rade for constructive discussions, advice and help with the field emission SEM.

I would also like to thank my colleagues at the Department for Nanostructured Materials, especially the one from my office.
Thanks to Mateja Podlogar, Martina Lorenzetti and Dr. Katja König for their encouragement.

I am very grateful to Dr. Paul McGuiness for the English correction of the text.

Finally, I would like to thank my family for giving me the opportunity to study and of course, very special thanks to my boys Robi and Niko for their support and patience.

8 References

1. Ratner, B. D. *Biomaterials science: an introduction to materials in medicine* (Elsevier Academic Press, Amsterdam; Boston, 2004).
2. Hench, L. L. Bioceramics - from Concept to Clinic. *American Ceramic Society Bulletin* **72**, 93–98 (1993).
3. Dubok, V. A. Bioceramics - Yesterday, today, tomorrow. *Powder Metallurgy and Metal Ceramics* **39**, 381–394 (2000).
4. Yaszemski, M. J. *Biomaterials in orthopedics* (M. Dekker, New York, 2004).
5. Sarmiento-González, A.; Marchante-Gayón, J. M.; Tejerina-Lobo, J. M.; Paz-Jiménez, J.; Sanz-Medel, A. High-resolution ICP–MS determination of Ti, V, Cr, Co, Ni, and Mo in human blood and urine of patients implanted with a hip or knee prosthesis. *Anal Bioanal Chem* **391**, 2583–2589 (2008).
6. Sarmiento-Gonzalez, A.; Encinar, J.; Marchante-Gayon, J. M.; Sanz-Medel, A. Titanium levels in the organs and blood of rats with a titanium implant, in the absence of wear, as determined by double-focusing ICP-MS. *Analytical and Bioanalytical Chemistry* **393**, 335–343 (2009).
7. Sargeant, A.; Goswami, T. Hip implants - Paper VI - Ion concentrations. *Materials & Design* **28**, 155–171 (2007).
8. Patton, M. S.; Lyon, T. D. B.; Ashcroft, G. P. Levels of systemic metal ions in patients with intramedullary nails. *Acta Orthopaedica* **79**, 820–825 (2008).
9. Cadosch, D.; Chan, E.; Gautschi, O. P.; Filgueira, L. Metal is not inert: Role of metal ions released by biocorrosion in aseptic loosening—Current concepts. *Journal of Biomedical Materials Research Part A* **91A**, 1252–1262 (2009).
10. Kumar, V.; Gill, K. D. Aluminium neurotoxicity: neurobehavioural and oxidative aspects. *Archives of Toxicology* **83**, 965–978 (2009).
11. Verstraeten, S.; Aimo, L.; Oteiza, P. Aluminium and lead: molecular mechanisms of brain toxicity. *Archives of Toxicology* **82**, 789–802 (2008).
12. Dorner, T.; Haas, J.; Loddenkemper, C.; von Baehr, V.; Salama, A. Implant-related inflammatory arthritis. *Nature Clinical Practice Rheumatology* **2**, 53–56 (2006).
13. Hallab, N. J.; Caicedo, M.; Epstein, R.; McAllister, K.; Jacobs, J. J. In vitro reactivity to implant metals demonstrates a person-dependent association with both T-Cell and B-Cell activation. *Journal of Biomedical Materials Research Part A* **92A**, 667–682 (2010).
14. Muller, K.; Valentine-Thon, E. Hypersensitivity to titanium: Clinical and laboratory evidence. *Neuroendocrinology Letters* **27**, 31–35 (2006).
15. Liu, X. Y.; Chu, P. K.; Ding, C. X. Surface modification of titanium, titanium alloys, and related materials for biomedical applications. *Materials Science & Engineering R-Reports* **47**, 49–121 (2004).
16. Li, J. P.; Habibovic, P.; van den Doel, M.; Wilson, C. E.; de Wijn, J. R.; van

Blitterswijk, C. A.; de Groot, K. Bone ingrowth in porous titanium implants produced by 3D fiber deposition. *Biomaterials* **28**, 2810–2820 (2007).

17. Ryan, G.; Pandit, A.; Apatsidis, D. P. Fabrication methods of porous metals for use in orthopaedic applications. *Biomaterials* **27**, 2651–2670 (2006).
18. Butler, J. B. V.; Lansky, D.; Duwelius, P. J. Prospective evaluation of total hip arthroplasty with a cementless, anatomically designed, porous-coated femoral implant: Mean 11-year follow-up. *Journal of Arthroplasty* **20**, 709–716 (2005).
19. Weng, W. J.; Baptista, J. L. Preparation and characterization of hydroxyapatite coatings on Ti6Al4V alloy by a sol-gel method. *Journal of the American Ceramic Society* **82**, 27–32 (1999).
20. Gallardo, J.; Galliano, P.; Moreno, R.; Duran, A. Bioactive sol-gel coatings for orthopaedic prosthesis. *Journal of Sol-Gel Science and Technology* **19**, 107–111 (2000).
21. Fathi, M. H.; Doostmohammadi, A. Bioactive glass nanopowder and bioglass coating for biocompatibility improvement of metallic implant. *Journal of Materials Processing Technology* **209**, 1385–1391 (2009).
22. Schrooten, J.; Helsen, J. A. Adhesion of bioactive glass coating to Ti6Al4V oral implant. *Biomaterials* **21**, 1461–1469 (2000).
23. Stojanovic, D.; Jokic, B.; Veljovic, D.; Petrovic, R.; Uskokovic, P. S.; Janackovic, D. Bioactive glass-apatite composite coating for titanium implant synthesized by electrophoretic deposition. *Journal of the European Ceramic Society* **27**, 1595–1599 (2007).
24. Borrajo, J. P.; Serra, J.; Gonzalez, P.; Leon, B.; Munoz, F. M.; Lopez, M. In vivo evaluation of titanium implants coated with bioactive glass by pulsed laser deposition. *Journal of Materials Science-Materials in Medicine* **18**, 2371–2376 (2007).
25. Hijon, N.; Manzano, M.; Salinas, A. J.; Vallet-Regi, M. Bioactive CaO-SiO_2-PDMS coatings on Ti6Al4V substrates. *Chemistry of Materials* **17**, 1591–1596 (2005).
26. Koller, G.; Cook, R. J.; Thompson, I. D.; Watson, T. F.; Di Silvio, L. Surface modification of titanium implants using bioactive glasses with air abrasion technologies. *Journal of Materials Science-Materials in Medicine* **18**, 2291–2296 (2007).
27. Das, K.; Bandyopadhyay, A.; Bose, S. Biocompatibility and in situ growth of TiO_2 nanotubes on Ti using different electrolyte chemistry. *Journal of the American Ceramic Society* **91**, 2808–2814 (2008).
28. Ryu, H. S.; Song, W.-H.; Hong, S.-H. Biomimetic apatite induction of P-containing titania formed by micro-arc oxidation before and after hydrothermal treatment. *Surface and Coatings Technology* **202**, 1853–1858 (2008).
29. Chen, H.-T.; Chung, C.-J.; Yang, T.-C.; Chiang, I. P.; Tang, C.-H.; Chen, K.-C.; He, J.-L. Osteoblast growth behavior on micro-arc oxidized β-titanium alloy. *Surface and Coatings Technology* **205**, 1624–1629 (2010).
30. Yang, Y. Z.; Park, S. W.; Liu, Y. X.; Lee, K. M.; Kim, H. S.; Koh, J. T.; Menge, X. W.; Kim, K. H.; Ji, H. B.; Wang, X. D.; Ong, J. L. Development of sputtered nanoscale titanium oxide coating on osseointegrated implant devices and their biological evaluation. *Vacuum* **83**, 569–574 (2008).

31. Zhao, J. M.; Tsuru, K.; Hayakawa, S.; Osaka, A. Modification of Ti implant surface for cell proliferation and cell alignment. *Journal of Biomedical Materials Research Part A* **84A**, 988–993 (2008).
32. Zhao, L. Z.; Mei, S. L.; Wang, W.; Chu, P. K.; Wu, Z. F.; Zhang, Y. M. The role of sterilization in the cytocompatibility of titania nanotubes. *Biomaterials* **31**, 2055–2063 (2010).
33. Riley, D. J.; Bavastrello, V.; Covani, U.; Barone, A.; Nicolini, C. An in-vitro study of the sterilization of titanium dental implants using low intensity UV-radiation. *Dental Materials* **21**, 756–760 (2005).
34. Shiraishi, K.; Koseki, H.; Tsurumoto, T.; Baba, K.; Naito, M.; Nakayama, K.; Shindo, H. Antibacterial metal implant with a TiO_2-conferred photocatalytic bactericidal effect against Staphylococcus aureus. *Surface and Interface Analysis* **41**, 17–22 (2009).
35. Suchanek, W. L.; Riman, R. E. Hydrothermal Synthesis of Advanced Ceramic Powders. *ChemInform* **38**, no–no (2007).
36. Byrappa, K.; Yoshimura, M. *Handbook of hydrothermal technology : a technology for crystal growth and materials processing* (Noyes Publications, Norwich, N.Y., 2001).
37. Byrappa, K.; Adschiri, T. Hydrothermal technology for nanotechnology. *Progress in Crystal Growth and Characterization of Materials* **53**, 117–166 (2007).
38. Dove, P. M.; De Yoreo, J.; Weiner, S.; Mineralogical Society of America. *Biomineralization* (Mineralogical Society of America, Washington, DC, 2003).
39. Uchida, M.; Kim, H. M.; Kokubo, T.; Fujibayashi, S.; Nakamura, T. Structural dependence of apatite formation on titania gels in a simulated body fluid. *Journal of Biomedical Materials Research Part A* **64A**, 164–170 (2003).
40. Beusen, J.; Van Bael, M. K.; Van den Rul, H.; D'Haen, J.; Mullens, J. Preparation of a porous nanocrystalline TiO_2 layer by deposition of hydrothermally synthesized nanoparticles. *Journal of the European Ceramic Society* **27**, 4529–4535 (2007).
41. Ueda, M.; Uchibayashi, Y.; Otsuka-Yao-Matsuo, S.; Okura, T. Hydrothermal synthesis of anatase-type TiO_2 films on Ti and Ti-Nb substrates. *Journal of Alloys and Compounds* **459**, 369–376 (2008).
42. Ueda, M.; Kinoshita, T.; Ikeda, M.; Ogawa, M. Photo-induced formation of hydroxyapatite on TiO_2 synthesized by a chemical-hydrothermal treatment. *Materials Science & Engineering C-Materials for Biological Applications* **29**, 2246–2249 (2009).
43. Cheng, F. T.; Shi, P.; Man, H. C. A preliminary study of TiO_2 deposition on NiTi by a hydrothermal method. *Surface & Coatings Technology* **187**, 26–32 (2004).
44. Liu, F.; Wang, F. P.; Shimizu, T.; Igarashi, K.; Zhao, L. C. Formation of hydroxyapatite on Ti-6Al-4V alloy by microarc oxidation and hydrothermal treatment. *Surface & Coatings Technology* **199**, 220–224 (2005).
45. Obata, A.; Zhai, T.; Kasuga, T. Apatite-forming ability on titanium surface modified by hydrothermal treatment and ultraviolet irradiation. *Journal of Materials Research* **23**, 3169–3175 (2008).
46. Wong, M. H.; Cheng, F. T.; Man, H. C. Comparison of corrosion resistance and apatite-forming ability of NiTi treated by different low-temperature methods.

Journal of Alloys and Compounds **466**, L5–L10 (2008).

47. Rani, V. V. D.; Vinoth-Kumar, L.; Anitha, V. C.; Manzoor, K.; Deepthy, M.; Shantikumar, V. N. Osteointegration of titanium implant is sensitive to specific nanostructure morphology. *Acta Biomaterialia* **8**, 1976–1989 (2012).
48. Lopez-Esteban, S.; Saiz, E.; Fujino, S.; Oku, T.; Suganuma, K.; Tomsia, A. P. Bioactive glass coatings for orthopedic metallic implants. *Journal of the European Ceramic Society* **23**, 2921–2930 (2003).
49. Hench, L. L. Bioceramics. *Journal of the American Ceramic Society* **81**, 1705–1728 (1998).
50. Hench, L. L. The story of Bioglass (R). *Journal of Materials Science-Materials in Medicine* **17**, 967–978 (2006).
51. Li, R.; Clark, A. E.; Hench, L. L. An Investigation of Bioactive Glass Powders by Sol-Gel Processing. *Journal of Applied Biomaterials* **2**, 231–239 (1991).
52. Day, R. M.; Boccaccini, A. R.; Shurey, S.; Roether, J. A.; Forbes, A.; Hench, L. L.; Gabe, S. M. Assessment of polyglycolic acid mesh and bioactive glass for soft-tissue engineering scaffolds. *Biomaterials* **25**, 5857–5866 (2004).
53. Leu, A.; Leach, J. K. Proangiogenic potential of a collagen/bioactive glass substrate. *Pharmaceutical Research* **25**, 1222–1229 (2008).
54. Keshaw, H.; Forbes, A.; Day, R. M. Release of angiogenic growth factors from cells encapsulated in alginate beads with bioactive glass. *Biomaterials* **26**, 4171–4179 (2005).
55. Allan, I.; Newman, H.; Wilson, M. Antibacterial activity of particulate Bioglass (R) against supra- and subgingival bacteria. *Biomaterials* **22**, 1683–1687 (2001).
56. Bellantone, M.; Williams, H. D.; Hench, L. L. Broad-spectrum bactericidal activity of Ag_2O-doped bioactive glass. *Antimicrobial Agents and Chemotherapy* **46**, 1940–1945 (2002).
57. Di Zhang, E. M., Leena Hupa, Heimo Ylanen, Matti K Viljanen, Mikko Hupa Factors Controlling Antibacterial Properties of Bioactive Glasses. *Key Engineering Materials* **330–332**, 173–176 (2001).
58. Hoppe, A.; Guldal, N. S.; Boccaccini, A. R. A review of the biological response to ionic dissolution products from bioactive glasses and glass-ceramics. *Biomaterials* **32**, 2757–2774 (2011).
59. Shelby, J. E. *Introduction to glass science and technology* (Royal Society of Chemistry, Cambridge, 2005).
60. Lotfibakhshaiesh, N.; Brauer, D. S.; Hill, R. G. Bioactive glass engineered coatings for Ti6Al4V alloys: Influence of strontium substitution for calcium on sintering behaviour. *Journal of Non-Crystalline Solids* **356**, 2583–2590 (2010).
61. Tilocca, A. Structural models of bioactive glasses from molecular dynamics simulations. *Proceedings of the Royal Society a-Mathematical Physical and Engineering Sciences* **465**, 1003–1027 (2009).
62. http://www.rsc.org/education/eic/issues/2006nov/glassbones.asp (accessed: May 2012).
63. Kokubo, T. Apatite formation on surfaces of ceramics, metals and polymers in body environment. *Acta Materialia* **46**, 2519–2527 (1998).
64. Peitl, O.; Zanotto, E. D.; Hench, L. L. Highly bioactive P_2O_5-Na_2O-CaO-SiO_2 glass-ceramics. *Journal of Non-Crystalline Solids* **292**, 115–126 (2001).
65. Kim, H. M. Ceramic bioactivity and related biomimetic strategy. *Current*

Opinion in Solid State & Materials Science **7**, 289–299 (2003).

66. Elgayar, I.; Aliev, A. E.; Boccaccini, A. R.; Hill, R. G. Structural analysis of bioactive glasses. *Journal of Non-Crystalline Solids* **351**, 173–183 (2005).
67. Wallace, K. E.; Hill, R. G.; Pembroke, J. T.; Brown, C. J.; Hatton, P. V. Influence of sodium oxide content on bioactive glass properties. *Journal of Materials Science-Materials in Medicine* **10**, 697–701 (1999).
68. Arstila, H.; Hupa, L.; Karlsson, K. H.; Hupa, M. In vitro bioactivity of partially crystallised glasses. *Glass Technology: European Journal of Glass Science and Technology Part A* **48**, 196–199 (2007).
69. Filho, O. P.; Latorre, G. P.; Hench, L. L. Effect of crystallization on apatite-layer formation of bioactive glass 45S5. *Journal of Biomedical Materials Research* **30**, 509–514 (1996).
70. Xynos, I. D.; Edgar, A. J.; Buttery, L. D. K.; Hench, L. L.; Polak, J. M. Gene-expression profiling of human osteoblasts following treatment with the ionic products of Bioglass® 45S5 dissolution. *Journal of Biomedical Materials Research* **55**, 151–157 (2001).
71. Hench, L. L. Genetic design of bioactive glass. *Journal of the European Ceramic Society* **29**, 1257–1265 (2009).
72. Varanasi, V. G.; Owyoung, J. B.; Saiz, E.; Marshall, S. J.; Marshall, G. W.; Loomer, P. M. The ionic products of bioactive glass particle dissolution enhance periodontal ligament fibroblast osteocalcin expression and enhance early mineralized tissue development. *Journal of Biomedical Materials Research Part A* **98A**, 177–184 (2011).
73. Xynos, I. D.; Edgar, A. J.; Buttery, L. D. K.; Hench, L. L.; Polak, J. M. Ionic products of bioactive glass dissolution increase proliferation of human osteoblasts and induce insulin-like growth factor II mRNA expression and protein synthesis. *Biochemical and Biophysical Research Communications* **276**, 461–465 (2000).
74. Brinker, C. J.; Scherer, G. W. *Sol-gel science : the physics and chemistry of sol-gel processing* (Academic Press, Boston, 1990).
75. Martinez, A.; Izquierdo-Barba, I.; Vallet-Regi, M. Bioactivity of a CaO-SiO_2 binary glasses system. *Chemistry of Materials* **12**, 3080–3088 (2000).
76. Hench, L. L. Sol-gel materials for bioceramic applications. *Current Opinion in Solid State & Materials Science* **2**, 604–610 (1997).
77. Vallet-Regi, M.; Salinas, A. J.; Martinez, A.; Izquierdo-Barba, I.; Perez-Pariente, J. Textural properties of CaO-SiO_2 glasses for use in implants. *Solid State Ionics* **172**, 441–444 (2004).
78. Saravanapavan, P.; Jones, J. R.; Verrier, S.; Beilby, R.; Shirtliff, V. J.; Hench, L. L.; Polak, J. M. Binary CaO-SiO_2 gel-glasses for biomedical applications. *Bio-Medical Materials and Engineering* **14**, 467–486 (2004).
79. Saravanapavan, P.; Jones, J. R.; Pryce, R. S.; Hench, L. L. Bioactivity of gel-glass powders in the CaO-SiO_2 system: A comparison with ternary (CaO-P_2O_5-SiO_2) and quaternary glasses (SiO_2-CaO-P_2O_5-Na_2O). *Journal of Biomedical Materials Research Part A* **66A**, 110–119 (2003).
80. Saravanapavan, P.; Hench, L. L. Bioactive sol-gel glasses in the CaO-SiO_2 system. *Bioceramics* **192–1**, 609–612 (2000).
81. Pereira, M. M.; Hench, L. L. Mechanisms of hydroxyapatite formation on porous gel-silica substrates. *Journal of Sol-Gel Science and Technology* **7**, 59–

68 (1996).

82. Roman, J.; Padilla, S.; Vallet-Regi, M. Sol-gel glasses as precursors of bioactive glass ceramics. *Chemistry of Materials* **15**, 798–806 (2003).
83. Levy, S.; Van Dalen, M.; Agonafer, S.; Soboyejo, W. O. Cell/surface interactions and adhesion on bioactive glass 45S5. *Journal of Materials Science-Materials in Medicine* **18**, 89–102 (2007).
84. Pereira, M. M.; Clark, A. E.; Hench, L. L. Calcium-Phosphate Formation on Sol-Gel-Derived Bioactive Glasses in-Vitro. *Journal of Biomedical Materials Research* **28**, 693–698 (1994).
85. Ramila, A.; Vallet-Regi, M. Static and dynamic in vitro study of a sol-gel glass bioactivity. *Biomaterials* **22**, 2301–2306 (2001).
86. Ramila, A.; Balas, F.; Vallet-Regi, M. Synthesis routes for bioactive sol-gel glasses: Alkoxides versus nitrates. *Chemistry of Materials* **14**, 542–548 (2002).
87. Mami, M.; Lucas-Girot, A.; Oudadesse, H.; Dorbez-Sridi, R.; Mezahi, F.; Dietrich, E. Investigation of the surface reactivity of a sol-gel derived glass in the ternary system SiO_2-CaO-P_2O_5. *Applied Surface Science* **254**, 7386–7393 (2008).
88. Hong, Z. K.; Liu, A. X.; Chen, L.; Chen, X. S.; Jing, X. B. Preparation of bioactive glass ceramic nanoparticles by combination of sol-gel and coprecipitation method. *Journal of Non-Crystalline Solids* **355**, 368–372 (2009).
89. Lei, B.; Chen, X.; Wang, Y.; Zhao, N.; Du, C.; Zhang, L. Acetic acid derived mesoporous bioactive glasses with an enhanced in vitro bioactivity. *Journal of Non-Crystalline Solids* **355**, 2583–2587 (2009).
90. Chen, X. F.; Lei, B.; Wang, Y. J.; Zhao, N. Morphological control and in vitro bioactivity of nanoscale bioactive glasses. *Journal of Non-Crystalline Solids* **355**, 791–796 (2009).
91. Xia, W.; Chang, J. Preparation and characterization of nano-bioactive-glasses (NBG) by a quick alkali-mediated sol-gel method. *Materials Letters* **61**, 3251–3253 (2007).
92. Hong, Z.; Liu, A.; Chen, L.; Chen, X.; Jing, X. Preparation of bioactive glass ceramic nanoparticles by combination of sol-gel and coprecipitation method. *Journal of Non-Crystalline Solids* **355**, 368–372 (2009).
93. Meiszterics, A.; Sinkó, K. Sol–gel derived calcium silicate ceramics. *Colloids and Surfaces A: Physicochemical and Engineering Aspects* **319**, 143–148 (2008).
94. Labbaf, S.; Tsigkou, O.; Müller, K. H.; Stevens, M. M.; Porter, A. E.; Jones, J. R. Spherical bioactive glass particles and their interaction with human mesenchymal stem cells in vitro. *Biomaterials* **32**, 1010–1018 (2011).
95. Green, D. L.; Lin, J. S.; Lam, Y. F.; Hu, M. Z. C.; Schaefer, D. W.; Harris, M. T. Size, volume fraction, and nucleation of Stober silica nanoparticles. *Journal of Colloid and Interface Science* **266**, 346–358 (2003).
96. Harris, L. G.; Richards, R. G. Staphylococci and implant surfaces: a review. *Injury-International Journal of the Care of the Injured* **37**, 3–14 (2006).
97. Kawashita, M.; Tsuneyama, S.; Miyaji, F.; Kokubo, T.; Kozuka, H.; Yamamoto, K. Antibacterial silver-containing silica glass prepared by sol-gel method. *Biomaterials* **21**, 393–398 (2000).
98. Balamurugan, A.; Balossier, G.; Laurent-Maquin, D.; Pina, S.; Rebelo, A. H. S.;

Faure, J.; Ferreira, J. M. F. An in vitro biological and anti-bacterial study on a sol-gel derived silver-incorporated bioglass system. *Dental Materials* **24**, 1343–1351 (2008).

99. Ahmed, I.; Ready, D.; Wilson, M.; Knowles, J. C. Antimicrobial effect of silver-doped phosphate-based glasses. *Journal of Biomedical Materials Research Part A* **79A**, 618–626 (2006).
100. Percival, S. L.; Bowler, P. G.; Russell, D. Bacterial resistance to silver in wound care. *Journal of Hospital Infection* **60**, 1–7 (2005).
101. Cho, Y.-H.; Lee, S.-J.; Lee, J. Y.; Kim, S. W.; Lee, C. B.; Lee, W. Y.; Yoon, M. S. Antibacterial effect of intraprostatic zinc injection in a rat model of chronic bacterial prostatitis. *International Journal of Antimicrobial Agents* **19**, 576–582 (2002).
102. Varmette, E. A.; Nowalk, J. R.; Flick, L. M.; Hall, M. M. Abrogation of the inflammatory response in LPS-stimulated RAW 264.7 murine macrophages by Zn- and Cu-doped bioactive sol–gel glasses. *Journal of Biomedical Materials Research Part A* **90A**, 317–325 (2009).
103. Beherei, H. H.; Mohamed, K. R.; Mahmoud, A. I. Lim, C. T.; Goh, J. C. H. (eds.) *Preparation, Bioactivity and Antibacterial Effect of Bioactive Glass/Chitosan Biocomposites 13th International Conference on Biomedical Engineering* (Springer Berlin Heidelberg, 2009).
104. Boyd, D.; Li, H.; Tanner, D.; Towler, M.; Wall, J. The antibacterial effects of zinc ion migration from zinc-based glass polyalkenoate cements. *Journal of Materials Science: Materials in Medicine* **17**, 489–494 (2006).
105. Zhou, G.; Li, Y. B.; Xiao, W.; Zhang, L.; Zuo, Y.; Xue, J.; Jansen, J. A. Synthesis, characterization, and novel nanohydroxyapatite/zinc antibacterial activities of a oxide complex. *Journal of Biomedical Materials Research Part A* **85A**, 929–937 (2008).
106. Balamurugan, A.; Balossier, G.; Kannan, S.; Michel, J.; Rebelo, A. H. S.; Ferreira, J. M. F. Development and in vitro characterization of sol–gel derived CaO–P_2O_5–SiO_2–ZnO bioglass. *Acta Biomaterialia* **3**, 255–262 (2007).
107. Lusvardi, G.; Malavasi, G.; Menabue, L.; Menziani, M. C.; Pedone, A.; Segre, U.; Aina, V.; Perardi, A.; Morterra, C.; Boccafoschi, F.; Gatti, S.; Bosetti, M.; Cannas, M. Properties of zinc releasing surfaces for clinical applications. *Journal of Biomaterials Applications* **22**, 505–526 (2008).
108. Haimi, S.; Gorianc, G.; Moimas, L.; Lindroos, B.; Huhtala, H.; Räty, S.; Kuokkanen, H.; Sándor, G. K.; Schmid, C.; Miettinen, S.; Suuronen, R. Characterization of zinc-releasing three-dimensional bioactive glass scaffolds and their effect on human adipose stem cell proliferation and osteogenic differentiation. *Acta Biomaterialia* **5**, 3122–3131 (2009).
109. Aina, V.; Perardi, A.; Bergandi, L.; Malavasi, G.; Menabue, L.; Morterra, C.; Ghigo, D. Cytotoxicity of zinc-containing bioactive glasses in contact with human osteoblasts. *Chemico-Biological Interactions* **167**, 207–218 (2007).
110. Guida, A.; Towler, M. R.; Wall, J. G.; Hill, R. G.; Eramo, S. Preliminary work on the antibacterial effect of strontium in glass ionomer cements. *Journal of Materials Science Letters* **22**, 1401–1403 (2003).
111. Gentleman, E.; Fredholm, Y. C.; Jell, G.; Lotfibakhshaiesh, N.; O'Donnell, M. D.; Hill, R. G.; Stevens, M. M. The effects of strontium-substituted bioactive glasses on osteoblasts and osteoclasts in vitro. *Biomaterials* **31**, 3949–3956

(2010).

112. Lao, J.; Jallot, E.; Nedelec, J. M. Strontium-delivering glasses with enhanced bioactivity: A new biomaterial for antiosteoporotic applications? *Chemistry of Materials* **20**, 4969–4973 (2008).

113. Hesaraki, S.; Alizadeh, M.; Nazarian, H.; Sharifi, D. Physico-chemical and in vitro biological evaluation of strontium/calcium silicophosphate glass. *Journal of Materials Science: Materials in Medicine* **21**, 695–705 (2010).

114. Lin, Y. G.; Yang, Z. R.; Cheng, J.; Wang, L. S. Synthesis, characterization and antibacterial property of strontium half and totally substituted hydroxyapatite nanoparticles. *Journal of Wuhan University of Technology-Materials Science Edition* **23**, 475–479 (2008).

115. Abou Neel, E. A.; Ahmed, I.; Pratten, J.; Nazhat, S. N.; Knowles, J. C. Characterisation of antibacterial copper releasing degradable phosphate glass fibres. *Biomaterials* **26**, 2247–2254 (2005).

116. Leonelli, C.; Lusvardi, G.; Malavasi, G.; Menabue, L.; Tonelli, M. Synthesis and characterization of cerium-doped glasses and in vitro evaluation of bioactivity. *Journal of Non-Crystalline Solids* **316**, 198–216 (2003).

117. Stoor, P.; Söderling, E.; Salonen, J. I. Antibacterial effects of a bioactive glass paste on oral microorganisms. *Acta Odontologica Scandinavica* **56**, 161–165 (1998).

118. Zhang, D.; Munukka, E.; Lepparanta, O.; Hupa, L.; Ylanen, H.; Salonen, J.; Eerola, E.; Vijanen, M. K.; Hupa, M. Comparison of antibacterial effect of three bioactive glasses. *Bioceramics 18, Pts 1 and 2* **309–311**, 345–348 (2006).

119. Allan, I.; Newman, H.; Wilson, M. Particulate Bioglass (R) reduces the viability of bacterial biofilms formed on its surface in an in vitro model. *Clinical Oral Implants Research* **13**, 53–58 (2002).

120. Lepparanta, O.; Vaahtio, M.; Peltola, T.; Zhang, D.; Hupa, L.; Hupa, M.; Ylanen, H.; Jukka, I. S.; Matti, K. V.; Eerola, E. Antibacterial effect of bioactive glasses on clinically important anaerobic bacteria in vitro. *Journal of Materials Science-Materials in Medicine* **19**, 547–551 (2008).

121. Munukka, E.; Lepparanta, O.; Korkeamaki, M.; Vaahtio, M.; Peltola, T.; Zhang, D.; Hupa, L.; Ylanen, H.; Salonen, J. I.; Viljanen, M. K.; Eerola, E. Bactericidal effects of bioactive glasses on clinically important aerobic bacteria. *Journal of Materials Science-Materials in Medicine* **19**, 27–32 (2008).

122. Vaahtio, M.; Munukka, E.; Lepparanta, O.; Zhang, D.; Eerola, E.; Ylanen, H.; Peltola, T. Effect of ion release on antibacterial activity of melt-derived and sol-gel-derived reactive ceramics. *Bioceramics 18, Pts 1 and 2* **309–311**, 349–352 (2006).

123. Sawai, J. Quantitative evaluation of antibacterial activities of metallic oxide powders (ZnO, MgO and CaO) by conductimetric assay. *Journal of Microbiological Methods* **54**, 177–183 (2003).

124. Kokubo, T.; Takadama, H. How useful is SBF in predicting in vivo bone bioactivity? *Biomaterials* **27**, 2907–2915 (2006).

125. Underwood, E. *Quantitative Stereology* (New York, Addison-Wesley., 1970).

126. Velten, D.; Biehl, V.; Aubertin, F.; Valeske, B.; Possart, W.; Breme, J. Preparation of TiO_2 layers on cp-Ti and Ti6Al4V by thermal and anodic oxidation and by sol-gel coating techniques and their characterization. *Journal of Biomedical Materials Research* **59**, 18–28 (2002).

127. Horvat, B.; Rečnik, A.; Dražić, G. The growth of anatase bipyramidal crystals during hydrothermal synthesis. *Journal of Crystal Growth* **347**, 19–24 (2012).

128. Xie, Y.; Heo, S. H.; Yoo, S. H.; Ali, G.; Cho, S. O. Synthesis and Photocatalytic Activity of Anatase TiO(2) Nanoparticles-coated Carbon Nanotubes. *Nanoscale Research Letters* **5**, 603–607 (2010).

129. Briand, L- E.; Cornaglia, L., Guida, J., Thomas, H.J., Stadelmann, P. A. Formation of a solid-solution of vanadium in TiO_2 (anatase) on V-Ti solids with high vanadium content. *Journal of Materials Chemistry* **5**, 1433–145 (1995).

130. Dodd, N. J. F.; Jha, A. N. Titanium dioxide induced cell damage: A proposed role of the carboxyl radical. *Mutation Research-Fundamental and Molecular Mechanisms of Mutagenesis* **660**, 79–82 (2009).

131. Bream. A.; Neirinck. B.; Schrooten, B.; Van der Biest, O.; Vleugels, J.; Biofunctionalization of porous titanium coatings through sol-gel impregnation with a bioactive glass-ceramic. *Materials Science and Engineering C* **32**, 2292–2298 (2012).

132. Federman, S. R.; Costa, V. C.; Vasconcelos, D. C. L.; Vasconcelos, W. L. Sol-Gel SiO_2-CaO-P_2O_5 biofilm with surface engineered for medical application. *Materials Research* **10**, 177–181 (2007).

133. Hench, L. L.; Splinter, R. J.; Allen, W. C.; Greenlee, T. K. Bonding mechanisms at the interface of ceramic prosthetic materials. *Journal of Biomedical Materials Research* **5**, 117–141 (1971).

134. Mami, M.; Lucas-Girot, A.; Oudadesse, H.; Dorbez-Sridi, R.; Mezahi, F.; Dietrich, E. Investigation of the surface reactivity of a sol–gel derived glass in the ternary system SiO_2–CaO–P_2O_5. *Applied Surface Science* **254**, 7386–7393 (2008).

135. Almeida, R. M.; Gama, A.; Vueva, Y. Bioactive sol-gel scaffolds with dual porosity for tissue engineering. *Journal of Sol-Gel Science and Technology* **57**, 336–342 (2011).

136. Goel, A.; Kapoor, S.; Rajagopal, R. R.; Pascual, M. J.; Kim, H.-W.; Ferreira, J. M. F. Alkali-free bioactive glasses for bone tissue engineering: A preliminary investigation. *Acta Biomaterialia* **8**, 361–372 (2012).

137. Chang, M. C.; Tanaka, J. FT-IR study for hydroxyapatite/collagen nanocomposite cross-linked by glutaraldehyde. *Biomaterials* **23**, 4811–4818 (2002).

138. Clupper, D. C.; Mecholsky Jr, J. J.; LaTorre, G. P.; Greenspan, D. C. Bioactivity of tape cast and sintered bioactive glass-ceramic in simulated body fluid. *Biomaterials* **23**, 2599–2606 (2002).

139. Rani, V. V. D.; Manzoor, K.; Menon, D.; Selvamurugan, N.; Nair, S. V. The design of novel nanostructures on titanium by solution chemistry for an improved osteoblast response. *Nanotechnology* **20** (2009).

140. Wong, M. H.; Cheng, F. T.; Man, H. C. In situ hydrothermal synthesis of oxide film on NiTi for improving corrosion resistance in Hanks' solution. *Scripta Materialia* **56**, 205–208 (2007).

141. Barnard, A. S.; Curtiss, L. A. Prediction of TiO2 nanoparticle phase and shape transitions controlled by surface chemistry. *Nano Letters* **5**, 1261–1266 (2005).

142. Dong, X.; Tao, J.; Li, Y. Y.; Zhu, H. Oriented single crystalline TiO_2 nano-pillar arrays directly grown on titanium substrate in tetramethylammonium

hydroxide solution. *Applied Surface Science* **256**, 2532–2538 (2010).

143. Chen, Y. X.; He, X.; Zhao, X. J.; Yuan, Q. H.; Gu, X. Y. Preparation, characterization, and growth mechanism of a novel aligned nanosquare anatase in large quantities in the presence of TMAOH. *Journal of Colloid and Interface Science* **310**, 171–177 (2007).
144. Nicholas, N. J.; Franks, G. V.; Ducker, W. A. Selective Adsorption to Particular Crystal Faces of ZnO. *Langmuir* **28**, 7189–7196 (2012).
145. Rupp, F.; Haupt, M.; Klostermann, H.; Kim, H. S.; Eichler, M.; Peetsch, A.; Scheideler, L.; Doering, C.; Oehr, C.; Wendel, H. P.; Sinn, S.; Decker, E.; von Ohle, C.; Geis-Gerstorfer, J. Multifunctional nature of UV-irradiated nanocrystalline anatase thin films for biomedical applications. *Acta Biomaterialia* **6**, 4566–4577 (2010).
146. Grigal, I. P.; Markeev, A. M.; Gudkova, S. A.; Chernikova, A. G.; Mityaev, A. S.; Alekhin, A. P. Correlation between bioactivity and structural properties of titanium dioxide coatings grown by atomic layer deposition. *Applied Surface Science* **258**, 3415–3419 (2012).
147. Wu, J. M.; Hayakawa, S.; Tsuru, K.; Osaka, A. Low-temperature preparation of anatase and rutile layers on titanium substrates and their ability to induce in vitro apatite deposition. *Journal of the American Ceramic Society* **87**, 1635–1642 (2004).
148. Wang, X. X.; Hayakawa, S.; Tsuru, K.; Osaka, A. Bioactive titania gel layers formed by chemical treatment of Ti substrate with a H_2O_2/HCl solution. *Biomaterials* **23**, 1353–1357 (2002).
149. Gong, X. Q.; Selloni, A. Reactivity of anatase TiO_2 nanoparticles: The role of the minority (001) surface. *Journal of Physical Chemistry B* **109**, 19560–19562 (2005).
150. Takadama, H.; Kim, H.-M.; Kokubo, T.; Nakamura, T. TEM-EDX study of mechanism of bonelike apatite formation on bioactive titanium metal in simulated body fluid. *Journal of Biomedical Materials Research* **57**, 441–448 (2001).
151. Yamaguchi, S.; Takadama, H.; Matsushita, T.; Nakamura, T.; Kokubo, T. Preparation of bioactive Ti-15Zr-4Nb-4Ta alloy from HCl and heat treatments after an NaOH treatment. *Journal of Biomedical Materials Research Part A* **97A**, 135–144 (2011).
152. Han, Y.; Chen, D.; Sun, J.; Zhang, Y.; Xu, K. UV-enhanced bioactivity and cell response of micro-arc oxidized titania coatings. *Acta Biomaterialia* **4**, 1518–1529 (2008).
153. Liu, S.; Yu, J.; Jaroniec, M. Anatase TiO_2 with Dominant High-Energy {001} Facets: Synthesis, Properties, and Applications. *Chemistry of Materials* **23**, 4085–4093 (2011).
154. Feng, B.; Chen, J. Y.; Qi, S. K.; He, L.; Zhao, J. Z.; Zhang, X. D. Characterization of surface oxide films on titanium and bioactivity. *Journal of Materials Science-Materials in Medicine* **13**, 457–464 (2002).
155. Pattanayak, D. K.; Yamaguchi, S.; Matsushita, T.; Kokubo, T. Nanostructured positively charged bioactive TiO_2 layer formed on Ti metal by NaOH, acid and heat treatments. *Journal of Materials Science-Materials in Medicine* **22**, 1803–1812 (2011).
156. Yang, X. F.; Chen, Y.; Yang, F.; He, F. M.; Zhao, S. F. Enhanced initial adhesion of

osteoblast-like cells on an anatase-structured titania surface formed by H2O2/HCl solution and heat treatment. *Dental Materials* **25**, 473–480 (2009).

157. Shi, G.-S.; Ren, L.-F.; Wang, L.-Z.; Lin, H.-S.; Wang, S.-B.; Tong, Y.-Q. H_2O_2/HCl and heat-treated Ti-6Al-4V stimulates pre-osteoblast proliferation and differentiation. *Oral Surgery, Oral Medicine, Oral Pathology, Oral Radiology, and Endodontology* **108**, 368–375 (2009).

158. Feng, B.; Weng, J.; Yang, B. C.; Qu, S. X.; Zhang, X. D. Characterization of surface oxide films on titanium and adhesion of osteoblast. *Biomaterials* **24**, 4663–4670 (2003).

159. Chen, H.-T.; Chung, C.-J.; Yang, T.-C.; Chiang, I. P.; Tang, C.-H.; Chen, K.-C.; He, J.-L. Osteoblast growth behavior on micro-arc oxidized [beta]-titanium alloy. *Surface and Coatings Technology* **205**, 1624–1629 (2010).

160. Anselme, K. Osteoblast adhesion on biomaterials. *Biomaterials* **21**, 667–681 (2000).

161. Itala, A. I.; Ylanen, H. O.; Ekholm, C.; Karlsson, K. H.; Aro, H. T. Pore diameter of more than 100 microm is not requisite for bone ingrowth in rabbits. *Journal of Biomedical Materials Research* **58**, 679–83 (2001).

162. Bobyn, J. D.; Pilliar, R. M.; Cameron, H. U.; Weatherly, G. C. THE OPTIMUM PORE-SIZE FOR THE FIXATION OF POROUS-SURFACED METAL IMPLANTS BY THE INGROWTH OF BONE. *Clinical Orthopaedics and Related Research*, 263–270 (1980).

163. Chang, B.-S.; Lee, C.-K.; Hong, K.-S.; Youn, H.-J.; Ryu, H.-S.; Chung, S.-S.; Park, K.-W. Osteoconduction at porous hydroxyapatite with various pore configurations. *Biomaterials* **21**, 1291–1298 (2000).

164. van Tienen, T. G.; Heijkants, R. G. J. C.; Buma, P.; de Groot, J. H.; Pennings, A. J.; Veth, R. P. H. Tissue ingrowth and degradation of two biodegradable porous polymers with different porosities and pore sizes. *Biomaterials* **23**, 1731–1738 (2002).

165. Stangl, R.; Pries, A.; Loos, B.; Muller, M.; Erben, R. G. Influence of pores created by laser superfinishing on osseointegration of titanium alloy implants. *Journal of Biomedical Materials Research Part A* **69A**, 444–453 (2004).

166. Gasik, M.; Van Mellaert, L.; Pierron, D.; Braem, A.; Hofmans, D.; De Waelheyns, E.; Anné, J.; Harmand, M.-F.; Vleugels, J. Reduction of Biofilm Infection Risks and Promotion of Osteointegration for Optimized Surfaces of Titanium Implants. *Advanced Healthcare Materials* **1**, 117–127 (2012).

167. Lucas-Girot, A.; Mezahi, F. Z.; Mami, M.; Oudadesse, H.; Harabi, A.; Le Floch, M. Sol–gel synthesis of a new composition of bioactive glass in the quaternary system SiO_2–CaO–Na_2O–P_2O_5: Comparison with melting method. *Journal of Non-Crystalline Solids* **357**, 3322–3327 (2011).

168. Chen, Q.-Z.; Li, Y.; Jin, L.-Y.; Quinn, J. M. W.; Komesaroff, P. A. A new sol–gel process for producing Na_2O-containing bioactive glass ceramics. *Acta Biomaterialia* **6**, 4143–4153 (2010).

169. Jokinen, M.; Rahiala, H.; Rosenholm, J. B.; Peltola, T.; Kangasniemi, I. Relation Between Aggregation and Heterogeneity of Obtained Structure in Sol-Gel Derived CaO-P_2O_5-SiO_2. *Journal of Sol-Gel Science and Technology* **12**, 159–167 (1998).

170. Edén, M. The split network analysis for exploring composition–structure correlations in multi-component glasses: I. Rationalizing bioactivity-

composition trends of bioglasses. *Journal of Non-Crystalline Solids* **357**, 1595–1602 (2011).

171. Cho, S. B.; Miyaji, F.; Kokubo, T.; Nakanishi, K.; Soga, N.; Nakamura, T. Apatite formation on silica gel in simulated body fluid: effects of structural modification with solvent-exchange. *Journal of Materials Science-Materials in Medicine* **9**, 279–284 (1998).

172. Nychka, J.; Mazur, S.; Kashyap, S.; Li, D.; Yang, F. Dissolution of bioactive glasses: The effects of crystallinity coupled with stress. *JOM Journal of the Minerals, Metals and Materials Society* **61**, 45–51 (2009).

173. Peitl, O.; LaTorre, G. P.; Hench, L. L. Effect of crystallization on apatite-layer formation of bioactive glass 45S5. *Journal of Biomedical Materials Research* **30**, 509–514 (1996).

174. Rao, K. J. *Structural chemistry of glasses* (Elsevier, Amsterdam ; New York, 2002).

175. Bini, M.; Grandi, S.; Capsoni, D.; Mustarelli, P.; Saino, E.; Visai, L. SiO_2–P_2O_5–CaO Glasses and Glass-Ceramics with and without ZnO: Relationships among Composition, Microstructure, and Bioactivity. *The Journal of Physical Chemistry C* **113**, 8821–8828 (2009).

176. Courtheoux, L.; Lao, J.; Nedelec, J. M.; Jallot, E. Controlled bioactivity in zinc-doped sol-gel-derived binary bioactive glasses. *Journal of Physical Chemistry C* **112**, 13663–13667 (2008).

177. Aina, V.; Malavasi, G.; Fiorio Pla, A.; Munaron, L.; Morterra, C. Zinc-containing bioactive glasses: Surface reactivity and behaviour towards endothelial cells. *Acta Biomaterialia* **5**, 1211–1222 (2009).

178. El-Kady, A. M.; Ali, A. F. Fabrication and characterization of ZnO modified bioactive glass nanoparticles. *Ceramics International* **38**, 1195–1204 (2012).

179. Lao, J.; Jallot, E.; Nedelec, J.-M. Strontium-Delivering Glasses with Enhanced Bioactivity: A New Biomaterial for Antiosteoporotic Applications? *Chemistry of Materials* **20**, 4969–4973 (2008).

180. Hesaraki, S.; Gholami, M.; Vazehrad, S.; Shahrabi, S. The effect of Sr concentration on bioactivity and biocompatibility of sol-gel derived glasses based on CaO-SrO-SiO_2-P_2O_5 quaternary system. *Materials Science & Engineering C-Materials for Biological Applications* **30**, 383–390 (2010).

181. Fredholm, Y. C.; Karpukhina, N.; Law, R. V.; Hill, R. G. Strontium containing bioactive glasses: Glass structure and physical properties. *Journal of Non-Crystalline Solids* **356**, 2546–2551 (2010).

182. Stoor, P.; Soderling, E.; Salonen, J. I. Antibacterial effects of a bioactive glass paste on oral microorganisms. *Acta Odontologica Scandinavica* **56**, 161–165 (1998).

183. Bellantone, M.; Coleman, N. J.; Hench, L. L. A novel sol-gel derived bioactive glass featuring antibacterial properties. *Bioceramics* **192–1**, 597–600 (2000).

184. El-Kady, A. M.; Ali, A. F.; Rizk, R. A.; Ahmed, M. M. Synthesis, characterization and microbiological response of silver doped bioactive glass nanoparticles. *Ceramics International* **38**, 177–188 (2012).

185. Shahnazari, M.; Sharkey, N. A.; Fosmire, G. J.; Leach, R. M. Effects of strontium on bone strength, density, volume, and microarchitecture in laying hens. *Journal of Bone and Mineral Research* **21**, 1696–1703 (2006).

186. Lang, C.; Murgia, C.; Leong, M.; Tan, L. W.; Perozzi, G.; Knight, D.; Ruffin, R.;

Zalewski, P. Anti-inflammatory effects of zinc and alterations in zinc transporter mRNA in mouse models of allergic inflammation. *American Journal of Physiology - Lung Cellular and Molecular Physiology* **292**, L577–L584 (2007).

187. Hu, H.; Zhang, W.; Qiao, Y.; Jiang, X.; Liu, X.; Ding, C. Antibacterial activity and increased bone marrow stem cell functions of Zn-incorporated TiO_2 coatings on titanium. *Acta Biomaterialia* **8**, 904–915 (2012).
188. Storrie, H.; Stupp, S. I. Cellular response to zinc-containing organoapatite: An in vitro study of proliferation, alkaline phosphatase activity and biomineralization. *Biomaterials* **26**, 5492–5499 (2005).
189. Ito, A.; Kawamura, H.; Otsuka, M.; Ikeuchi, M.; Ohgushi, H.; Ishikawa, K.; Onuma, K.; Kanzaki, N.; Sogo, Y.; Ichinose, N. Zinc-releasing calcium phosphate for stimulating bone formation. *Materials Science and Engineering: C* **22**, 21–25 (2002).
190. Hu, S.; Chang, J.; Liu, M. Q.; Ning, C. Q. Study on antibacterial effect of 45S5 Bioglass(A (R)). *Journal of Materials Science-Materials in Medicine* **20**, 281–286 (2009).
191. Lee, S.; Zimmer, J.; Fechner, J.; Uzunian, G. E.; Song, L. Bioactive Glasses as a Potential New Class of Anti-Oxidative Ingredients for Personal Care Products. *SöFW Journal* **129**, 2–7 (2003).
192. Saiz, E.; Lopez-Esteban, S.; Fujino, S.; Oku, T.; Suganuma, K.; Tomsia, A. P. Meyers, M. A.; Ritchie, R. O.; Sarikaya, M. (eds.). *Characterization of Metal/Glass Interfaces in Bioactive Glass Coatings on Ti-6Al-4V and Co-Cr Alloys* (Elsevier Science Ltd, Oxford, 2003).
193. Oku, T.; Suganuma, K.; Wallenberg, L. R.; Tomsia, A. P.; Gomez-Vega, J. M.; Saiz, E. Structural characterization of the metal/glass interface in bioactive glass coatings on Ti-6Al-4V. *Journal of Materials Science: Materials in Medicine* **12**, 413–417 (2001).

Index of Figures

Index of Tables

Appendix

Original scientific article

Drnovšek, N.; Rade K.; Milačič, R.; Štrancar, J.; Novak, S. The properties of bioactive TiO_2 coatings on Ti-based implants. *Surface and Coatings Technolology.* **209,** 177–183, (2012).

Drnovšek, N.; Novak, S.; Dragin, U.; Čeh, M.; Gorenšek, M.; Gradišar, M. Bioactive glass enhances bone ingrowth into the porous titanium coating on orthopaedic implants. *International Orthopaedics* **36**, 1739–1745 (2012).

Drnovšek, N.; Daneu, N.; Rečnik, A.; Mazaj, M.; Kovač, J.; Novak, S. Hydrothermal synthesis of a nanocrystalline anatase layer on Ti6Al4V implants. *Surface and Coatings Technolology* **203** 1462–1468 (2009).

Petković, J.; Žegura, B.; Stefanović, M.; Drnovšek, N.; Uskoković, D.; Novak, S.; Filipič, M. DNA damage and alterations in expression of DNA damage responsive genes induced by TiO_2 nanoparticles in human hepatoma HepG2 cells. *Nanotoxicology* **5**, 341–353 (2011).

Patents

Novak, S.; Drnovšek, N.; Murn, G. *Kostni vsadki v večslojno prevleko in postopek njihove priprave: patent SI 23420 A*. Ljubljana: Urad RS za intelektualno lastnino, 31. jan. 2012.

Novak, S.; Drnovšek, N. *Bioaktivna in fotokatalitska prevleka na kovinskih ortopedskih in dentalnih vsadkih in postopek priprave: patent SI 23312 A*. Ljubljana: Urad RS za intelektualno lastnino, 30. sept. 2011.

Novak, S.; Drnovšek, N.; *Implant having a multilayered coating and a process for preparing thereof:* patent application PCT/SI2011/000020. 13th April 2011.

Published scientific conference contribution abstract

Drnovšek, N.; Murn, G.; Rade, K.; Čeh, M.; Hofmans, D.; Mellaert, L. van.; Dragin, U.; Romih, R.; Gradišar, M.; Novak, S. Enhancement of osseointegration by BAG coating on Ti-based impalnts with porous surface. V: *Innovative biomaterials and crossing frontiers in biomaterials and regenerative medicine*. CD (Sichuan University, Chengdu, China, 2012).

Novak, S.; Drnovšek, N.; Rade, K.; Čeh, M.; Pierron D.; Harmand, M-F., Gradišar, M.;, Dragin, U.; Romih, R. Firmly bonded anatase TiO_2 coating on Ti-alloy implants. V: *Innovative biomaterials and crossing frontiers in biomaterials and regenerative medicine*. CD (Sichuan University, Chengdu, China, 2012).

Drnovšek, N.; Novak, S., Bioactive coatings in porous Ti-layer on Ti6Al4V alloy for bone implants with improved osseointegration. V: *2nd Joint Meeting of the COST action MP1005 NAMABIO Programme & book of abstracts.* 27 (Vienna University of Technology,Vienna, Austria, 2012).

Drnovšek, N.; Novak, S., Dragin, U.; Čeh, M.; Gorenc, M.; Gradišar, M. *In vivo* test of nanoparticulate bioactive glass coatings in porous Ti-implants. *J. tissue eng. regen. med.* **6-1**, 234 (2012).

Gantar, A.; Drnovšek, N.; Podlipec, R.; Štrancar, J.; Novak, S. Bioactive-glass/collagen composite scaffollds for bone regeneration. V: *2nd Joint Meeting of the COST action MP1005 NAMABIO Programme & book of abstracts.* 23 (Vienna University of Technology,Vienna, Austria, 2012).

Drnovšek, N.; Murn, G.; Dragin, U.; Hofmans, D.; Mellaert, L. van.; Romih, R.; Čeh, M.; Novak, S. Particulate sol-gel bioactive glass coating on Ti-based implants. V: *6th Young Researcher's Day 2012 Program and abstract book.* 31 (Jožef Stefan Institute, Ljubljana, Slovenia, 2012).

Drnovšek, N.; Murn, G.; Dragin, U.; Hofmans, D.; Van Mellaert, L.; Romih, R.; Čeh, M.; Novak, S. Particulate sol-gel bioactive glass coating on Ti-based implants. V: *The cycle of biomaterials - back to our roots*. 24th European Conference on Biomaterials. 381 (Dublin, Ireland, 2011).

Drnovšek, N.; Novak, S.; Rade, K.; Murn, G.; Milačič, R.; Harmand, M-F. Bioactive TiO_2 coatings on Ti6Al4V implants. V: *12th Conference of the European Ceramic Society ECerS XII*. CD (ECERS, Stockholm, Sweden, 2011).

Drnovšek, N.; Novak, S.; Rade, K.; Murn, G.; Milačič, R.; Harmand, M-F. Kostni vsadki na osnovi Ti6Al4V z izboljšano osteointegracijo. V: *5. dan mladih raziskovalcev. Program in povzetki.* 54 (Institut "Jožef Stefan", Ljubljana, Slovenia, 2011).

Drnovšek, N.; Van Mellaert, L.; Hofmans, D.; Novak, S. Bioactive glass prepared by particulate sol-gel method : antibacterial properties. V: *11th International Conference and Exhibition of the European Ceramic Society Conference Programme* *and book of abstracts*. 113 (ECERS, Krakow, Poland, 2009).

Rade, K.; Novak, S.; Drnovšek, N.; Kobe, S. Kompoziti iz hidroksiapatita in biostekla - priprava in karakterizacija bioaktivnosti. V: *Dan mladih raziskovalcev 2009*. CD (Institut "Jožef Stefan", Ljubljana, Slovenia, 2009).

Horvat, B.; Silva, A. M. T.; Dražić, G.; Drnovšek, N.; Novak, S. Meritve fotokatalitične aktivnosti TiO_2. V: *Dan mladih raziskovalcev 2009*. CD (Institut "Jožef Stefan", Ljubljana, Slovenia, 2009).

Drnovšek, N.; Van Mellaert, L.; Novak, S. Vpliv sestave bioaktivnih stekel pripravljenih po sol-gel postopku na rast bakterij S. epidermidis in S. aureus. V: *Dan mladih raziskovalcev 2009*. CD (Institut "Jožef Stefan", Ljubljana, Slovenia, 2009).

Drnovšek, N. Bioaktivne prevleke na kostnih vsadkih. V: *1. študentska konferenca Mednarodne podiplomske šole Jožefa Stefana. Zbornik prispevkov*. 18–19 (Mednarodna podiplomska šola Jožefa Stefana, Ljubljana, Slovenia, 2009).

Drnovšek, N.; Daneu, N.; Novak, S.; Kovač, J. Synthesis of nanocrystalline TiO_2 on Ti-alloy implants. V: *Hot nano topics 2008: incorporating SLONANO 2008, 3 overlapping workshops on current hot subjects in nanoscience: abstract book*. 239 (Ljubljana, Slovenia, 2008).

Rade, K.; Novak, S.; Drnovšek, N.; Kobe, S. Hydroxyapatite/bioglass composites - preparation and bioactivity characterization. V: *Hot nano topics 2008: incorporating SLONANO 2008, 3 overlapping workshops on current hot subjects in nanoscience: abstract book*. 256 (Ljubljana, Slovenia, 2008).

Horvat, B.; Drnovšek, N.; Rade, K.; Novak, S.; Dražić, G. Preparation of nano-anatase TiO_2. V: *1st International Conference on Materials and Technology sponsored by FEMS and IUVSTA*. *Program in knjiga povzetkov*. (Inštitut za kovinske materiale in tehnologije, Ljubljana, Slovenija, 2009).

Drnovšek, N.; Daneu, N.; Novak, S.; Kovač, J. Hydrothermal formation of TiO_2 later on the surface of Ti6Al4V alloy used for bone implants. V: *WomenInNano winter school abstract book.* 58. (Kranjska Gora, Slovenia, 2008).

Drnovšek, N.; Daneu, N.; Novak, S.; Rade, K.; Kovač, J. A double-layer coating on a Ti6A14V alloy for biomedical applications. V: *Mater. tehnol.*, **41-6**, 311–312 (2006).

Drnovšek, N.; Daneu, N.; Rade, K.; Kovač, J.; Novak, S. A double-layer coating on an Ti6Al4V alloy for biomedical applications. V: *15 Conference on Materials and Technology. Program in knjiga povzetkov*. 35 (Ljubljana, Inštitut za kovinske materiale in tehnologije, Portorož, Slovenia, 2007).

Drnovšek, N.; Daneu, N.; Novak, S. The formation of Ti-oxides on hydrothermally treated surface of Ti6Al4V alloy used for biomedical applications. V: *10th International Conference and Exhibition of the European Ceramic Society Programme*. (ECERS, Berlin, Germany, 2007).

Novak, S.; Dražić, G.; Drnovšek, N.; Toplišek, T.; Koenig, K.; Žagar, T. Razvoj keramičnega kompozita za osnovi SiC za uporabo v fuzijskem reaktorju. V: *14th Conference on Materials and Technology. Program in knjiga povzetkov.* 73 (Inštitut za kovinske materiale in tehnologije, Portorož, Slovenia, 2006).

Drnovšek, N.; Novak, S.; Daneu, N.; Pejovnik, S.; Low-temperature densification study of SiC-based ceramics. V: *14th Conference on Materials and Technology. Program in knjiga povzetkov.* 141 (Inštitut za kovinske materiale in tehnologije, Portorož, Slovenia, 2006).